Cross-shore suspended sediment transport and morphological response on a beach plain

during
fair weather
conditions
and

during a
storm event
at
The Slufter, Texel

Marjolijn Witteveen
0346683

MSc Thesis

Universiteit Utrecht

Cross-shore suspended sediment transport and morphological response on a beach plain during fair weather conditions and a storm event at

The Slufter, Texel

M.Witteveen
11/20/2011

Supervisors: Dr. B.G. Ruessink & Dr. M. van der Vegt
Faculty of Geosciences, Department of Physical Geography
Utrecht University, The Netherlands

Cross-shore suspended sediment transports were studied at a transect over a beach plain in a small tidal inlet system The Slufter located on the barrier island Texel, The Netherlands. Field measurements of the near-bed velocity and sediment concentrations were obtained using electromagnetic current meters and optical backscatter sensors. Spectral analyses of velocity and sediment concentration was performed on two time frames of low wave conditions and two time frames of high wave conditions to reveal the contributions of waves of different frequencies to the net transport. Sediment flux measurements showed that the main contributors to the gross suspended sediment transport were made by incident waves and undertow, causing onshore and offshore transport, respectively. Co-spectral density diagrams of high wave conditions have shown a high-frequency contribution to the onshore transport, but of minor importance to the gross suspended sediment transport. Morphological change over the cross-section was mapped with a DGPS system and by using depth-of-activity rods. Swash bars were formed and slowly migrated onshore during low wave conditions and the cross-shore profile flattened during high wave events.

Acknowledgements

Contents

List of photographs

List of Tables

List of Figures

1 Introduction

1.1 Background and problem definition

Research on suspended sediment transport in the nearshore region has significantly increased in the past decades, especially since the advent of new instruments like optical and acoustic backscatter sensors which detect suspended sediment with high temporal and spatial resolution. Previous studies provide evidence that contributions to nearshore sediment transport can come from local wind forced waves (sea), regional wind forced waves (swell), low-frequency waves (0.004 - 0.04 Hz) and offshore-directed mean currents (undertow) (Conley & Beach, 2003; Osborne & Greenwood, 1992a). These studies have shown that the relative contributions of these components can vary greatly in time and in the vertical as well as on the location in the surf zone. In general, the net transport signal represents a balance between an offshore-directed mean transport and an onshore-directed wave coherent transport (Conley & Beach, 2003; Osborne & Greenwood, 1992a). Conley and Beach (2003) have also shown that the relative contribution of these two components is a function of elevation above the bed. The effects of seabed ripples for example can cause turbulent mixing, as a result it takes time for sediment to move vertically upward in the water column and it takes time for the sediment to settle. Thus the sediment concentration is not in phase with the shear stress but generally lags it. Furthermore, the average flow profile is complex, e.g. onshore flow near the bottom (viscous streaming during low energy conditions), offshore flow slightly higher in the water column (undertow) and onshore flow near water surface (stokes flux). Overall it is difficult to predict the direction and magnitude of sediment transport in the surf zone and the ensuing morphological response, because of the various mechanisms contributing to the cross-shore suspended sediment transport, including mean currents and oscillatory waves at incident and infragravity frequencies. Therefore, more field measurements of suspended sediment transport rates are needed to resolve the relative contributions of the various mechanisms responsible for sediment transport. This is particularly true for storm conditions, because data measured during storms is generally incomplete owing to failure of the measuring devices. In the present study the instruments are less likely to fail during storm conditions because they are partly protected by a longshore bar and partly by a middle ground bar formed seaward of the main channel.

In this thesis a closer look is taken on the various sediment transport mechanisms occurring on a beach plain of a small tidal inlet system The Slufter, The Netherlands. This location is of interest because it not only possesses hydrodynamic processes seaward of the beach plain e.g. swash and undertow, but also other processes might occur like overwash due to the fact that the beach plain is backed by a lower lying dune valley and therefore viable to inundation during high wave conditions. These processes are of interest because the acquired process based knowledge from this research can be possibly used for understanding hydrodynamic processes at related areas in the Wadden Sea. Furthermore, the beach plain at The Slufter can be easily accessed for research on a daily basses. A

distinction is made between processes taking place during fair weather conditions (henceforth low wave conditions) and processes taking place during storm conditions (henceforth high wave conditions). The reason for this distinction is that sediment transport processes during low wave conditions are in a sense comparable to processes occurring at a gentle sloping beach backed by a dune. However, during high wave conditions water can flow over the beach plain to the backbarrier basin. The dynamics occurring during such a flooding event might be comparable to overwash processes. Overwash is the flow of water and sediment over the crest of the beach that does not directly return to the water body (ocean, sea, bay or lake) where it originated (Donnelly, Kraus, & Larson, 2006). Overwash processes occurs if either wave runup level or storm surge level (water level in excess of predicted tide) exceeds beach crest height. This will usually lead to erosion on the most seaward side of the barrier and deposition of sediment on the landward side. A previous study on the morphology of the beach and beach plain of The Slufter has shown a landward retreat of the beach and accretion of the beach flat due to storm conditions (Puijvelde, 2009). However, no morphological measurements were carried out in the back-barrier area. Therefore, it is not possible to say if overwash processes actually occurred. Until now only the morphological change of overwash processes has been recognized, but measurements of overwash processes are still lacking.

Complementary to the obtained process based knowledge this area is of interest because of its high nature value, where terrain conservationists like to maintain the dynamic nature of the tidal inlet system, but at the same time try to protect the hinterland from flooding. The priority for protecting the coastal hinterland of The Slufter against flooding started in the 70's by fixing the channel mouth and dune opening (Durieux, 2003). The influence of these and recent interventions (e.g. offshore sediment nourishment) on the development of The Slufter is difficult to foresee, especially because of limited research that has been conducted towards the hydrodynamic and morphodynamic processes in The Slufter. Since 1630 a dike protects the hinterland against flooding. However, mechanical measures in The Slufter still need to be taken ones every five years to prevent the dike and both dune feet at The Slufter's entrance from eroding. On the other hand, in the past decades the Dutch Ministry of Water Management (Rijkswaterstaat, RWS) focused their management strategy on natural processes occurring at the coastal zone (Durieux, 2003). Without human interferences the dune valleys and slufters along the Dutch coast regain their chance for natural development. Slufters are extreme valuable ecological areas with a wide diversity of flora and fauna due to the gradual transition of salt and fresh water. The present study will lead to a better understanding of the local hydro- and morphodynamics at the beach plain of The Slufter which is of interest for the RWS for their decision making for coastal management and can contribute to a safe and ecologically valuable tidal inlet system. Moreover, it will increase our knowledge on sediment transport as a function of height in the water column, various wave conditions (shoaling, surf or overwash) and wave forcing. This research is conducted as part of my MSc programme Physical Geography –

Track 'Coastal Dynamics and Fluvial Systems' under supervision of Dr. B.G. Ruessink and Dr. M. van der Vegt.

1.2 Research objectives

The aims of this report are: (1) to identify the cross-shore suspended sediment transport mechanisms over a beach plain during a storm; (2) to define the relative contribution of these mechanisms to the total suspended sediment flux; (3) to relate the net flux to the observed morphological change; (4) to confront storm conditions on the beach plain to more 'normal' conditions on the beach. In order to fulfil these aims the following research questions are formulated.

Main research question:

Which hydrodynamic processes dominate the cross-shore suspended sediment transport leading to the observed morphological change of the beach plain of the Slufter during storm conditions?

Sub-questions:

- How does the magnitude and direction of mean currents, oscillatory flows and infragravity motion vary as a function of cross-shore position and as a function of offshore forcing?
- What is the relative contribution of these flow mechanisms to the net suspended sediment transport and how does the relative contribution depend on cross-shore position and offshore forcing?
- What are the qualitative and quantitative differences between normal beach conditions and overwash processes during a flooding event?
- How does the morphology of the beach plain change during low- and high- energy conditions?

Previous study on suspended sediment transport during storm conditions demonstrate that in very dissipative environments (gentle slopes and/or more energetic conditions) where incident wave variance is small shoreward's of the breakpoint, infragravity waves and mean currents might dominate exclusively ((R. A. Beach & Sternberg, 1991; R. A. Beach & Sternberg, 1988) and (Russell, 1993)). Furthermore, data of (R. A. Beach & Sternberg, 1988) show that suspended sediment concentrations primarily develop and decay on time scales of the infragravity motions rather than those of the incident waves and therefore infragravity waves may play a dominant role in transporting sediment. Also the amount of infragravity energy increases significantly across the surf zone in the onshore direction which is largely assigned to shoaling of the infragravity waves entering shallower water (Masselink & Hughes, 2003). However, the incident wave energy level decreases in the onshore direction due to wave breaking. During high wave conditions the surf zone will become wider, because large incident storm waves break further offshore dissipating their energy

trough the wider surf zone. In contrast, infragravity energy is not dissipated in the surf zone and may therefore dominate the water motion in the inner surf zone during high wave conditions. Knowing this it is hypothesized that infragravity waves are the dominant cross-shore sediment transport mechanism that results in morphological change over the beach plain of The Slufter during high wave conditions.

1.3 Thesis Outline

This MSc Thesis starts with a short description of the study area (Chapter 2). The following chapter (Chapter 3) describes the methods used during and after the fieldwork including instrumentation and measurements, data calibration, suspended sediment transport calculations and analytical procedures. The results of the procedures explained in Chapter 3 are presented in Chapter 4 which is divided into four sections. First of all the environmental conditions, e.g. wind, offshore waves and tide will be discussed (section 4.1). Secondly, section 4.2 will describe the morphological change that occurred during the fieldwork period. Thirdly, the local hydrodynamics including the wave conditions and mean currents will be discussed (Section 4.3). The fourth section will cover the results of the cross-shore suspended sediment transport (Section 4.4). Topics that will be dealt with in this section are cross-shore velocity and concentrations, cross-shore suspended sediment fluxes and results of the spectral analysis. The findings of this study are discussed in Chapter 5. The final chapter (Chapter 6) summarizes the main conclusions of this study.

2 Study area

The data analysed in this thesis were collected at a beach plain located on the southern side of the mouth of The Slufter (blue dashed circle, Figure 2.1). The Slufter is a brackish/salty dune valley in connection with the North Sea via a tidal channel and is located on the north-western part of the barrier island Texel, The Netherlands. The Slufter valley has a total area of approximately 400 ha. This area contains around 50 ha dunes and dune valleys with a surface level of 2 m above NAP (Dutch Ordnance Datum, about Mean Sea Level, MSL). The majority of the flood basin, 270 to 300 ha, consists of scarcely vegetated sandy plates with a surface level ranging from 0.8 m to 1.5 m above NAP. Furthermore, there is an area of ± 80 ha that is flooded twice a day. The fieldwork campaign was conducted from mid-September till the end of October 2009.

Figure 2.1: Location of The Slufter (top) and study area (dashed blue circle) on the island Texel (bottom left) in The Netherlands (bottom right). Source: Google Earth image, 2008.

The coast is characterized as a dissipative beach and is exposed to wind-generated waves from predominantly western directions. The tide is semi-diurnal with a mean tidal range of 1.5 m and neap and spring tidal ranges of about 0.9 and 2.1 m, respectively. Furthermore, the tide is characterized by shorter flood duration of around 5 hours and longer ebb duration of about 7 hours. Besides the tide the water levels can also be momentarily increased by wind set-up, which increases/decreases the area of inundation if the wind is coming from the west/east. The entire Slufter basin is inundated when water levels reach 1.8 m + NAP. However, the beach plain, located at the entrance of The Slufter, is already inundated at water heights of around 1.5 m above NAP.

3 Methods

3.1 Instrumentation and measurements

The suspended sediment transport was measured in a cross-shore array from the low-tide level to the landward side of the beach plain. The instruments used during the fieldwork are three instrumented tripods (P1-P3). When the beach plain is not inundated, the instrumented cross-shore transect is limited to the intertidal beach face seaward of the beach plain (Photo 3-1). However, when high wave conditions are forecasted tripod P1 was repositioned to the highest point of the beach plain (P4), to enable measurements when the beach plain is inundated. The cross-shore profile at the onset of the campaign and the positions of the tripods are shown in Figure 3.1. The transect has a surface level ranging from -1.5 m to 1.5 m above NAP and shows a clear intertidal swash bar with an intertidal slope of $\beta = 0.02$. In addition a runnel is visible at 53 m landward of tripod P2 (Photo 3-1; Figure 3.1). The runnel was connected to the Slufter´s outflow channel to the north of the transect (see also Figure 2.1).
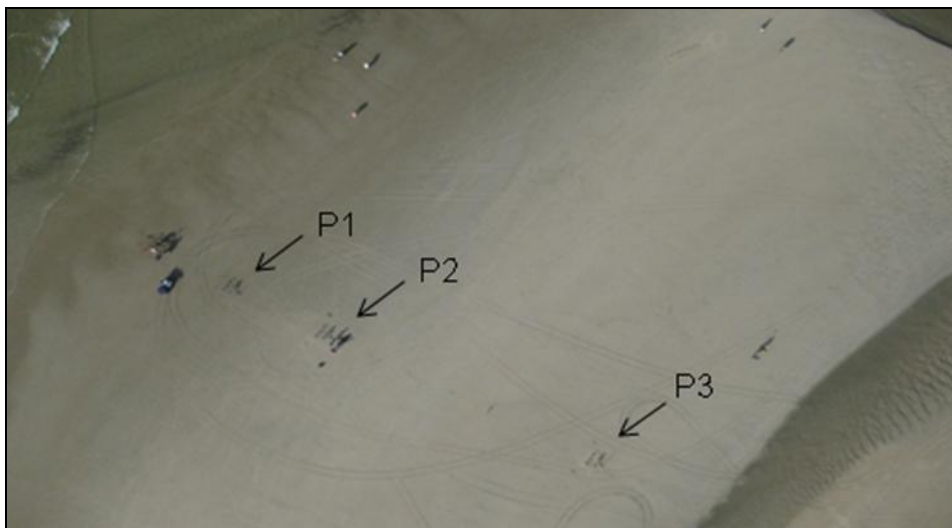
Photo 3-1: Instrument deployment in a cross-section over the beach plain (Source: airborne photo H. Markies).
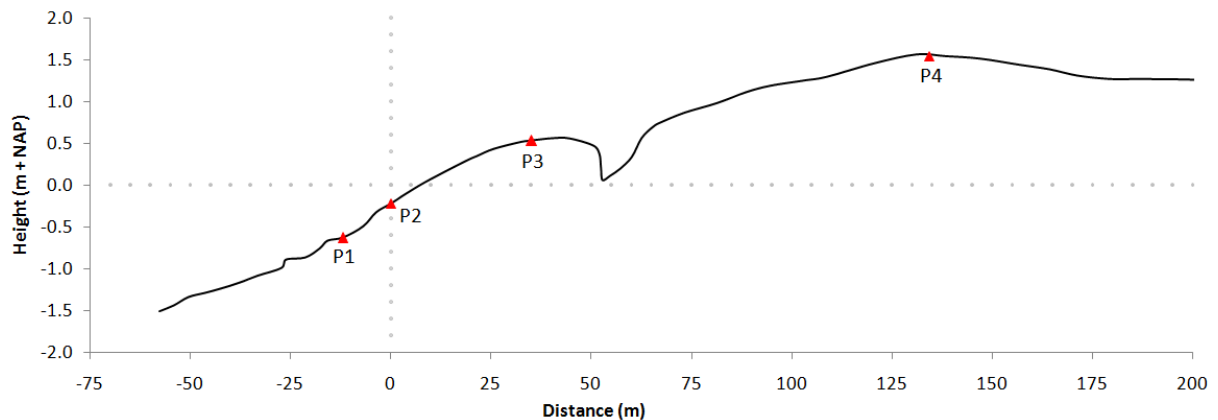

Figure 3.1: Cross-shore profile at the onset of the campaign, instrument positions (P1 = seaward position low energetic conditions, P2 = seaward position high energetic conditions and reference position at distance 0 m, P3 = landward position low energetic conditions, P4 = landward position high energetic conditions).

Table 3-1: Initial location of tripods, their initial bed level and local grain size diameter *d50.*

Tripod	Distance to shoreline[1] (m)	Initial bed level (m)	Grain size[2] (µm)
P1	-23	-0.63	356
P2	-11	-0.22	362
P3	27	0.54	290
P4	134	1.54	267

Sediment was collected at each tripod location to determine the grain size. According to the grain size scale of the American Geophysical Union the sediment at these four locations is composed of medium sand (Table 3-1; medium sand: 500-250 µm). Grain size can be used as an indicator of energy conditions (Van Rijn, 1993). Fine grains usually are dominant in low-energy conditions and coarse grains are found in high-energy conditions. The sediment on the beach plain shows a landward fining of sediment indicating higher energetic conditions at locations P1 and P2 compared to P4. This is due to the fact that tripods P1 and P2 are submerged each tide. Tripod P4, however, is located at the top of the beach plain which only rarely inundates and for that reason the sediment is mainly composed of windblown sand which is generally finer material.

Each tripod (Photo 3-2) is equipped with one Keller pressure sensor (20 cm above the bed), one Electromagnetic Current Meter (hereafter EMCM; 15 cm above the bed) and three Optical Backscatter Sensors, also known as Seapoint Turbidity Meter (hereafter OBS; 5, 10 and 20 cm above the bed). Their location with respect to the initial shoreline and initial bed level of deployment are given in Table 3-1. The pressure sensor is used for air pressure corrections and to determine the local water levels, the EMCM measures the flow velocity in two horizontal directions (x = cross-shore positive shoreward and y = longshore positive northward) and the OBS measures the sediment density in the water column. The OBS measures suspended sediment concentration only at discrete heights above the bed and is capable of measuring suspended sand concentrations in the range of 0.1 to 200 g l^{-1} or ppt (Hanes & Huntley, 1986).

Photo 3-2: a: Tripod with EMF, OBS, pressure sensor and data logger, **b:** COM-port connection with laptop.

---

[1] Shoreline is isoline of 0 m NAP. Note that this is the initial location of the shoreline and that it varies throughout the fieldwork.
[2] The median grain size diameter (d50) is calculated by use of the (Van Rijn, 1993) formula. The settling velocity is determined by using a sediment settling tube.

All instruments measured continuously with a frequency of 4 Hz. The data was saved on a data logger and was daily downloaded to a laptop during daylight at low tide. The instruments needed to calculate the suspended sediment transport rates are the EMCM and the OBS's. There are great limitations on the EMCM with respect to the proximity of the bed (Osborne & Greenwood, 1992a). The electromagnetic field can get distorted when the current meter is placed too close to the sea bed. EMCM's are typically deployed at a minimal height of 10 cm above the bed (Foote et al., 1998; Osborne & Greenwood, 1992a). OBS´s do not have this disadvantage and can be placed as close as 2.5 cm to the sea bed without significant degradation of signal-to-noise ratio ((Downing, Sternberg, & Lister, 1981)). The only limitation of placing OBS´s close to the sea bed is the risk of getting burrowed in the sand during which a concentration of 0 g/l is measured. Another problem that arises when the tripods slowly get burrowed is that the exact heights of the sensors above the bed are unknown. This burrowing usually slowed down when the lead weights sank 6 cm beneath the surface and therefore the OBS and EMCM instruments were repositioned 6 cm higher on the 26th of September to prevent them from digging in. The sensor height above the bed was measured once daily and was interpolated between these moments in time. Furthermore, OBS´s might be subject to interference of air bubbles entrained by breaking waves overestimating the suspended sediment concentration. Each OBS sensor needs to be calibrated for sand size particles, which will be carried out in a sediment recirculation tank using sand from its deployment site after the fieldwork.

The morphological response to cross-shore sediment transport is measured with several methods. One method is to use depth of disturbance rods (Figure 3.2; (Greenwood & Hale, 1980; Osborne & Greenwood, 1992a). A depth of disturbance rod is a round steel rod that is driven vertically into the sand until ± 0.50 m is left exposed above the surface; a loose-fitted ring is placed over the rod that provides the control for determining bed surface scour or aggradation. Rod measurements allow the determination of: (1) net bed elevation change; (2) maximum depth of activity relative to the pre-storm surface; and (3) degradation-aggradation cycles (Greenwood & Hale, 1980). The only sequence of events that cannot be deciphered by the rod is an episode of aggradation followed by a smaller degree of degradation; the net result would appear as aggradation. Although continuous monitoring of absolute values of sediment flux is not possible with this technique, its simplicity permits deployment of considerable numbers of rods for the detection of spatial variability of net flux (degradation-aggradation cycles) through time. The rods are placed in a transect from tripod P1 crossing tripods P2 and P3 and ends at the landward side of the runnel covering only the most dynamic part of the cross-shore profile (Photo 3-3; Figure 3.1).
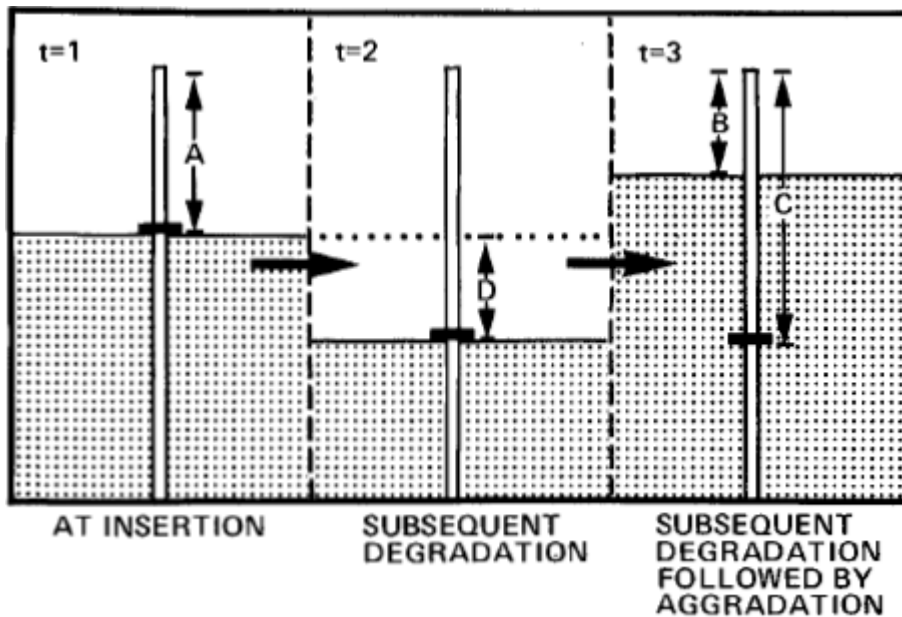
Figure 3.2: Interpretation of depth of disturbance rod: t = 1, 2, 3 represent time intervals, dotted area the sand bed and A, B, C, D measurements made relative to the top of the rod. The determinations to be made are: (**a**) net bed elevation change (A-B), this value may be positive or negative indicating aggradation or degradation; (**b**) maximum scour depth or depth of activity relative to the pre-storm surface (C-A); (**c**) total aggradation subsequent to maximum degradation (C-B) (Greenwood & Hale, 1980).
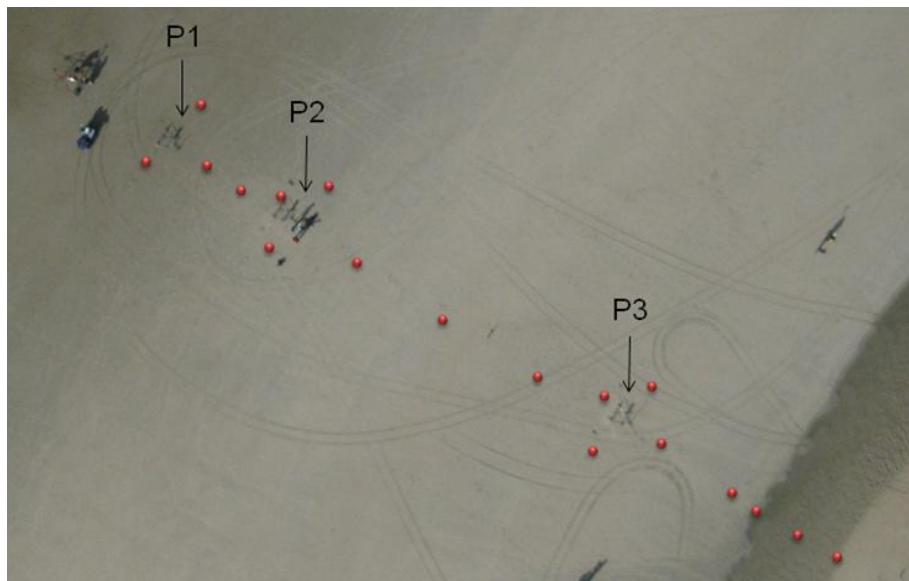
Photo 3-3: Transect of the rods displayed as red dots (Source: airborne photo H. Markies).

A second method that is used is a Differential Global Positioning System (DGPS) which measures bed level elevation with vertical resolution of 1 cm. DGPS uses a network of fixed, ground-based reference stations to broadcast the difference between the positions indicated by the satellite systems and the known fixed positions. The base station is located on top of the southern dune row (Photo 3-4a). DGPS measurements were taken daily with a human-operated DGPS device shown in Photo 3-4b to determine the morphological change during storm conditions.

Photo 3-4: a: DGPS base station with radio on the left and receiver on the right, **b:** Mobile DGPS device.

3.2 Data calibration

The data that was retrieved from the data logger consists of measurements expressed in millivolt. Before further calculation these measurements need to be converted to physically meaningful parameters. The relation between these measurements and the measured physical parameters has been determined with calibration data from individual instruments as well as from the individual tripods. The calibration values for the pressure sensors and EMCM's can be directly obtained from the instrumentation manual whereas the OBS's are calibrated in a laboratory. The conversion formulas of the measurements to physical parameters for the pressure sensor, EMCM and OBS are linear regression curves and are described below.

Pressure Sensor

$$p_w = \frac{x}{\alpha} \cdot w + c - p_a \tag{3.1}$$

where p_w is the water pressure above the sensor in mbar, w is the measurements data logger in mV, α is an electronical transformation factor, c is the regression constant, x is the regression coefficient and p_a is the atmospheric pressure in mbar. Furthermore, the water pressure is converted into water height by using formula 3.2 below.

$$h_w = h_{sen} + \frac{g}{\rho_w} \cdot p_w \tag{3.2}$$

where h_w is the local water height, p_w is the water pressure above the sensor in mbar, g is the gravitational acceleration (9.81 m/s^2), ρ_w is the density of sea water (1,027 kg/m^3 at a water temperature of 20°C) and h_{sen} is the height of the pressure sensor above bed level (0.1 m).

EMCM

$$u = \frac{w - o}{x \cdot \alpha} \tag{3.3}$$

where u is the cross-shore velocity in m/s, w is the measurements data logger in mV, α is an electronical transformation factor, o is the dynamic offset and x is the regression coefficient.

OBS

$$ssc = \frac{w-b}{\alpha}$$ (3.4)

where *ssc* is the suspended sediment concentration in g/L or kg/m^3, *w* is the measurements data logger in mV, α is the transformation factor and *b* is the intercept. Noise in the ssc-dataset like large spikes and negative ssc-values were deleted from the ssc-dataset. Furthermore, other noise like the ssc-values that lie below the trend of the ssc-profile was corrected by calculating the 5th percentile for each block of 5 minutes and subtracting this from the ssc-dataset.

3.3 Suspended sediment transport calculations

Measurements of cross-shore sediment transport on sandy beaches have shown that the direction of net transport is determined by the relative importance of the mean and oscillatory components of the incident wave motions (Osborne & Greenwood, 1992a). The net cross-shore suspended sediment transport <*uc*>$_{net}$ at a particular level at the near bed region can be calculated by the time-average of the product of the instantaneous suspended sediment concentration and velocity, as follows:

$$<uc>_{net} = \frac{1}{n}\sum uc$$ (3.5)

where n is the sample size and the brackets are indicative for the time-average (Aagaard & Greenwood, 1995; Osborne & Greenwood, 1992a). The local net sediment transport rate can be decomposed into two components, the mean flux due to mean velocity and mean sediment concentration $\overline{uc}$ and the oscillatory flux due to coupled fluctuations in velocity and sediment concentration $<\tilde{u}\tilde{c}>$. Hence, equation 3.5 can be written as:

$$<uc>_{net} = \overline{uc} + <\tilde{u}\tilde{c}>$$ (3.6)

The sediment concentration *c* of $\overline{uc}$ contains contributions of currents and infragravity and swell waves. The oscillatory term is non-zero when fluctuations in cross-shore velocity and concentration are correlated (Ruessink, Houwman, & Hoekstra, 1998). The oscillatory component can be subdivided into a high- (0.04 < *f* < 1 Hz) and low-frequency (0.004 < *f* < 0.04 Hz) sediment flux, indicated by the subscripts H and L respectively (see Equation 3.7):

$$<\tilde{u}\tilde{c}> = <(u_H + u_L)(c_H + c_L)> = <u_H c_H> + <u_L c_L>$$ (3.7)

The terms that consist of the product of a low- and high-frequency component are negligibly small in comparison with the other components, because high- (low-) frequency fluctuations in *u* are, in general, uncorrelated to low- (high-) frequency oscillations in *c* (Ruessink et al., 1998) and are therefore not included in the oscillatory component. Thus, equations 3.6 and 3.7 can be combined into:

$$<uc>_{net} = \overline{uc} + <u_H c_H> + <u_L c_L>$$ (3.8)

Positive (negative) values indicate onshore (offshore) fluxes, because the velocity is defined positive shoreward. A fundamental limitation of this approach is the existence of only point measurements of the current velocity and suspended sand concentration (Foote et al., 1998). This problem can be addressed in two ways:

1. assuming a logarithmic velocity profile (not expected, as velocity increases rapidly with height, but might be plausible for the bottom boundary layer) and a concentration profile derived from the balance between turbulent mixing and gravity forces acting on particles (Cayocca, 2001),
2. assuming an exponential sediment concentration profile, assuming the wave velocity is independent of depth and that the flux profile will be the product of a constant and the concentration profile (Nielsen, 1979),

While it is common practice to use a single velocity sensor to provide the current speed for concentration sensors at multiple elevations (Masselink & Pattiaratchi, 2000; Ruessink et al., 1998), Ogston and Sternberg (1995) have suggested that this can lead to errors in the magnitude and in the direction of transport with the result that the direction of depth-integrated transport can be onshore even in the presence of offshore transport further above the bed. Further results from Ogston and Sternberg (1995) suggest that the majority of the difference between single source transport and paired source transport estimates come from a reduction in velocity magnitude as the bed is approached. These observations suggest great caution must be exercised when interpreting sediment transport direction/magnitude measurements. Furthermore, the difference was greatest for the mean and infragravity transport components (Conley & Beach, 2003), a further explanation why this is the case was not given, but it is likely due to a larger bottom boundary layer for infragravity waves compared to the bottom boundary layer of regular waves (a few cm's). A simple engineering rule (equation 3.9; (Van Rijn, 1991) is used for the calculation of the mean current-related flux at all OBS-sensor heights to depth-correct the mean flow measured by the EMCM. The reason for using this equation is that it is simply not opportune to use a more complex formula given the uncertainty in instrument heights.

$$\bar{u}_1 = \bar{u}_2 \left(\frac{z_1}{z_2} \right)^{0.25} \tag{3.9}$$

Where z_1 and z_2 represent the height above the bed for the lower and upper OBS sensor respectively and $\bar{u}_1$ and $\bar{u}_2$ represent the corresponding mean velocity. The mean flow at OBS height 5, 10 and 20 cm above bed was estimated at 76, 90 and 100 % respectively of that measured by the EMCM at 20 cm above bed. Note that the instrument heights above bed level are not constant in time due to local accretion or erosion.

The importance of a flux to the cross-shore suspended sediment transport can be expressed as its relative contribution to the gross sediment transport. The relative contribution of the mean suspended sediment flux to the gross suspended sediment flux is given as an example (Equation 3.10), where | | indicate absolute values.

$$\frac{\left| \overline{uc} \right|}{\left| \overline{uc} \right| + \left| \langle \tilde{u}_H \tilde{c}_H \rangle \right| + \left| \langle \tilde{u}_L \tilde{c}_L \rangle \right|} \tag{3.10}$$

The mean suspended sediment flux in the numerator can be replaced by the high- and low-frequency flux to calculate their relative contribution to the gross sediment transport.

3.4 Analytical procedures

The following parameters were extracted from the dataset: water depth (h), wave height ($H_{1/3}$), wave period ($T_{1/3}$), mean sediment transport rates ($\overline{uc}$) and sediment transport rates at low- and high-frequency bands (<$u_L c_L$> and <$u_H c_H$> respectively). First of all a time domain analyses is performed on the wave record to determine individual wave properties (height, period, direction). The individual waves are sorted and significant wave height and root-mean-square wave height (H_s or $H_{1/3}$ and H_{rms}) are calculated over a period of 20 minutes. $H_{1/3}$ represents the average wave height of one-third of the highest waves in the wave record. The significant wave height approximately corresponds to visual estimates of wave heights and has been found to be particularly useful for practical design purposes by coastal engineers (Masselink & Hughes, 2003). The root-mean-square wave height is obtained by taking the square root of the mean squared wave height, using all the waves in the wave record. As a rule of thumb, $H_s=1.41H_{rms}$. The significant wave period ($T_{1/3}$) and the root-mean-square wave period (T_{rms}) can be calculated with a standard zero-down-crossing technique in the time domain (Ruessink et al., 1998).

Secondly, spectral analysis is used which is an alternative method that describes the properties of irregular waves (Masselink & Hughes, 2003). Spectral analysis can be based on the Fast Fourier Transform (FFT) of the record, which generally gives more resolution in frequency space than can be readily used. This method can be used to identify the dominant wave frequencies (or periods) present in the wave record. Spectral analysis produces a wave spectrum which is a plot of wave energy versus wave frequency. Before applying FFT to the wave record the pressure (p) and velocity (u) data need to be demeaned and detrended to determine the total oscillatory component $\tilde{u}$. Furthermore, a Hamming-window and 50 % overlapping data segments with a length of 600 s were applied to the demeaned and detrended dataset before obtaining the power spectral densities and co-spectra estimates. The number of degrees of freedom was 20. The co-spectrum (real part of cross-spectrum) between the suspended sediment concentration and cross-shore velocity time-series gives the net (suspended load) cross-shore transport spectrum (Huntley & Hanes, 1987) and allows the magnitude and direction of net sediment transport associated with the incident and low frequency waves to be determined. These can then be compared with the mean (steady) transport component. The wave spectrum is also useful for partitioning wave energy over distinct frequency bands. To separate low-frequency (u_L, c_L) and high-frequency (u_H, c_H) components, a low-pass filter with a cut-off period has to be applied (in Matlab script terms see Equations 3.11 and 3.12).

$$sseHF = fft\_filter(sse, 1/Fs, 0.04, 1); \tag{3.11}$$
$$sseLF = fft\_filter(sse, 1/Fs, 0.004, 0.04); \tag{3.12}$$

where *sse* is the detrended sea surface elevation for high- and low-frequency (HF and LF respectively), *fft_filter* is the Fast Fourier Transform filtered to the HF-component (0.04 – 1 *Hz*) and the LF-component (0.004 – 0.04 *Hz*) of the frequency spectrum and *Fs* is the sampling frequency in *Hz* thus *1/Fs* gives the sample time in *s*. Furthermore, the integral of the co-spectrum over the short-wave frequency and infragravity frequency region are equal

to the time-averaged oscillating fluxes (2nd and 3rd term on right hand side of Eq. 3.8). The local net oscillatory sediment transport rate can be obtained by integration of the co-spectrum over all frequencies.

In addition the coherence squared diagrams and the phase diagram are determined. The coherence squared estimate is calculated to give an indication of how well u corresponds linearly to c at each frequency. The coherence squared is a function of the power spectral density of u and c and the cross power spectral density of u and c (Equation 3.13).

$$coh^2 = \frac{P_{uc}\,conj\left(P_{uc}\right)}{P_{uu}P_{cc}}$$

(3.13)

where P_{uc} is the co-spectrum, $conj$ is the complex conjugate of the co-spectrum and P_{uu} and P_{cc} are the power spectral densities of u and c, respectively. The magnitude of the coherence lies between 0 and 1 (no and complete correlation respectively). The phase diagram (calculated with Equation 3.14) provides information on phase lags, in other words whether sediment is transported in the on- or offshore phase of the oscillatory wave motion.

$$pha = 360\left(\frac{atan\,2(Cuc, Quc)}{2\pi}\right)$$

(3.14)

where C_{uc} and Q_{uc} are the real and imaginary parts of the co-spectrum, $atan2$ is the four quadrant arctangent and multiplied by $360/2\pi$ to convert radians to degrees. The phase diagrams range from -180 to +180 degrees. A phase > |90˚| indicates that suspended sediment is present in the offshore phase of the wave motion and when the phase lies between -90˚ and +90˚ sediment is present in the onshore phase.

4 Results

Suspended sediment can be stirred and transported by a variety of processes. The sediment moves horizontally due to wave-dominated or current-dominated flow and vertically due to resuspension mechanisms e.g. vortex development, turbulence and breaking waves. To be able to identify the dominant cross-shore suspended sediment transport mechanisms over the beach plain of The Slufter it is of primary importance to identify the local hydrodynamics (section 4.3). In addition, spectral analysis is performed to obtain information on the magnitude and direction of cross-shore suspended sediment transport (section 4.4). But before going into depth on the aforementioned topics it is of great value to consider the environmental conditions, e.g. wind, offshore waves and tide (section 4.1), and to discuss the morphological change that occurred during the fieldwork period (section 4.2).

4.1 Wind, offshore waves and tide

An overview of several environmental conditions including the wind, offshore waves and tide during the fieldwork period is presented in Figure 4.1a-h. The prevailing wind direction during the fieldwork is from northwest to west with an average wind speed of 7 m/s (Figure 4.1a, b). A wide range of offshore wave conditions were observed at the offshore station Wadden Eierlandse Gat located slightly northwest of Texel where the water depth is 20 m. The offshore wave angle, significant wave height and significant wave period are shown in Figure 4.1c, d and e respectively. Note that offshore wave data from the 24th of September is absent from Figure 4.1c, d and e due to the fact that only wave data from the 25th of September till the 10th of November was acquired from the Dutch Ministry of Water Management. The wave angle indicates the directions from which waves approach the shoreline which is generally in accordance with the prevailing wind direction (Figure 4.1b, c). The fieldwork period is dominated by low to intermediate wave conditions (Figure 4.1d). Four periods are marked in Figure 4.1a, d and f, e.g. LWC1+2 and HWC1+2 (LWC/HWC = low/high wave conditions), because these periods represent characteristic change in the morphology (see chapter 4.2). Offshore significant wave heights (Hs) varied between 0.3 and 5.8 m with a mean significant wave height of 1.5 m and the significant offshore wave period (Ts) ranged from 3 to 8.6 s with a mean significant period of 4.7 s (Figure 4.1d, e). The measured tide and the astronomical tide are given in Figure 4.1f and g, respectively, and show a semi-diurnal pattern. There are clear deviations between the measured tide and the astronomical tide, especially on the 3rd and 4th of October (Figure 4.1f). This is because the measured tide includes weather effects contrary to the astronomical tide. The measured tide includes wave set-up/set-down and storm surge levels. Set-up/set-down is calculated by subtracting the astronomical water height from the measured water height (Figure 4.1). When the wind changes in north-westerly direction the fetch increases and when merged with a storm, offshore significant wave heights exceed 4 m, with wave periods of 7 s. Storm surge levels of about 1 m are reached during severe storms (Figure 4.1h).
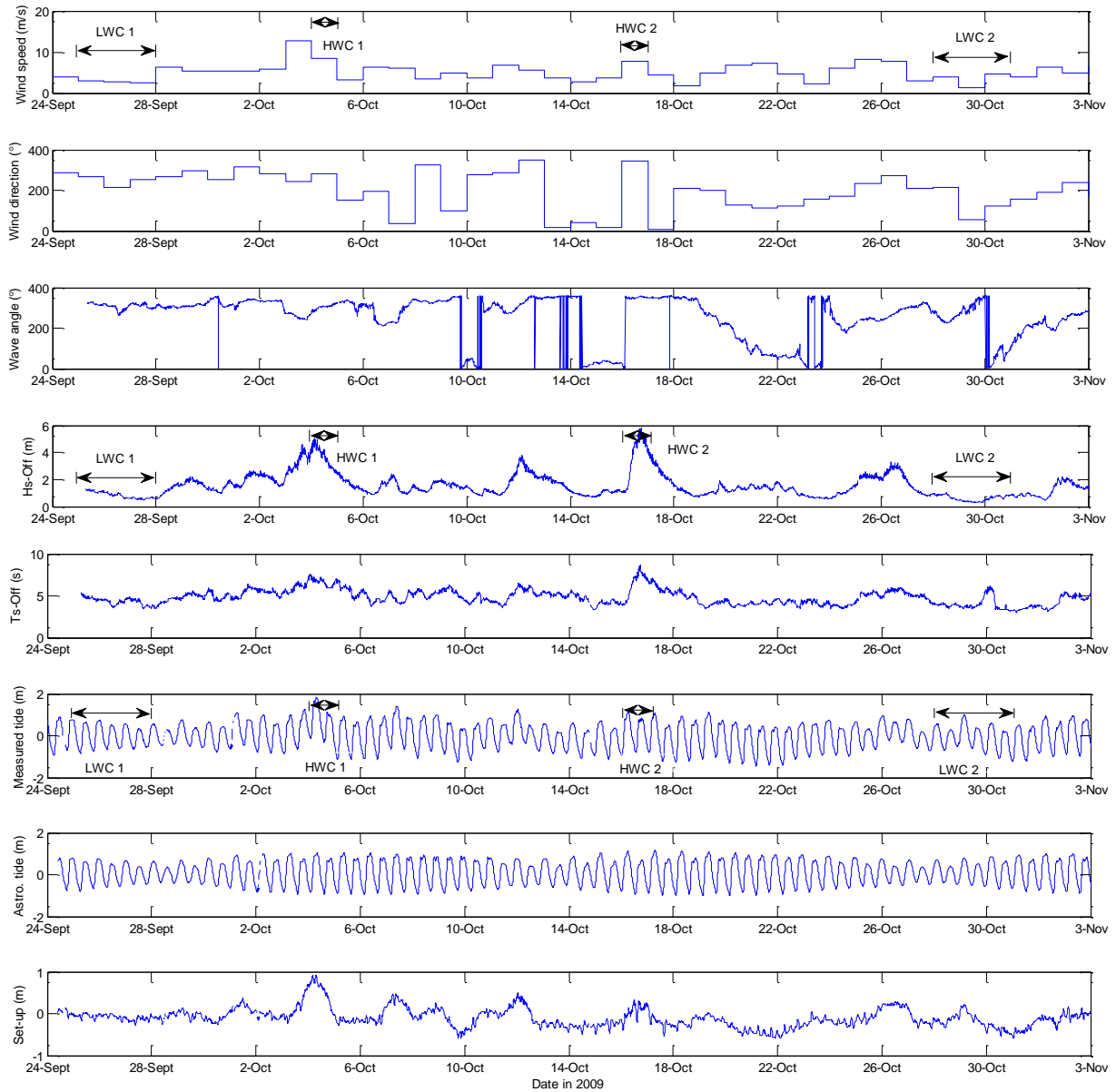
Figure 4.1: Environmental conditions during the fieldwork period, **a:** daily mean wind speed, **b:** vector mean wind direction (360˚=north, 90˚=east, 180˚=south, 270˚=west, 0˚=calm/variable; source: Royal Netherlands Meteorological Institute, *KNMI*), **c:** wave angle relative to the North (orientation of coastline is 33˚N), **d:** offshore significant wave height **e:** offshore significant wave period (offshore measuring station 'Wadden Eierlandse Gat'), **f:** measured tide, **g:** astronomical tide (Source: Dutch Ministry of Water Management, *RWS*) and **h:** set-up or set-down. Note that the subfigures a, d and f containing the forcing factors wind, wave and tide, respectively, include the four periods that were analysed in more detail (LWC's 1+2 and HWC's 1+2; see section 4.2).

4.2 Morphological change

This section gives a qualitative assessment of the morphological change that occurred during the course of the fieldwork. The observed morphological change, recorded with DGPS along a transect of the beach plain (Photo 3-3), can be divided into four distinctive periods of morphological development, namely: (a) onshore swash bar migration prior to storm inundation (19th of September till the 3rd of October), (b) inundation during first storm causing overwash processes (3rd till 5th of October), (c) erosion of high-water areas (≈ + 1.0 m NAP) during second storm (16th and 17th of October) and (d) no significant morphological change during remainder of fieldwork period (18th of October till the 1st of November). DGPS data was also collected for areas surrounding this transect, however this thesis focuses on suspended sediment transport across the transect of the beach plain and therefore only DGPS data of the transect is used for analysing the morphological change.

4.2.1 Onshore swash bar migration prior to storm inundation

The morphology of the initial profile (red line in Figure 4.2; mapped on the 19th of September) shows a distinct intertidal swash bar and runnel system. Field observations during the first two weeks of the fieldwork period, last two weeks of September, have shown that the runnel slowly migrated landward and started to fill up with sediment. This is also visible in Figure 4.2 and Figure 4.3 where the DGPS profiles show an initial onshore migration of the swash bar from the 22nd till the 25th of September. Furthermore, the landward slope of the runnel became less steep. A new swash bar and runnel was created on the 22nd of September near tripod P2 which also migrated onshore in the following days up to the 28th of September (Figure 4.2 and Figure 4.3). Overall the decrease in swash bar crest and the development of a wider and less deep trough flattened the intertidal profile. The remaining landward part of the profile showed little bed level change. The morphological changes discussed above occurred during low wave conditions (Figure 4.1d) and to investigate which sediment transport processes are responsible for these morphological changes a period from 25th till the 28th of September, henceforth LWC1, is chosen for suspended sediment transport analysis (see section 4.4).
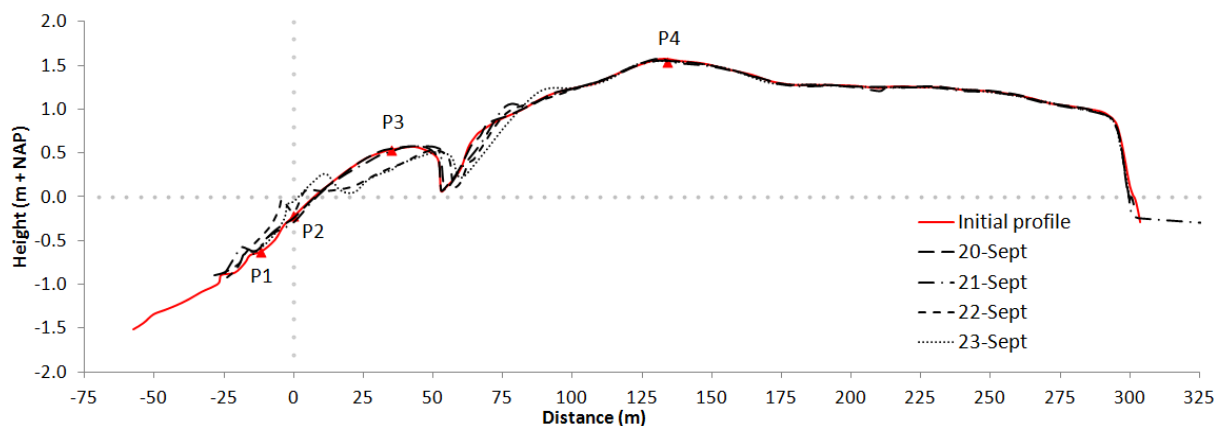

Figure 4.2: Changes in beach plain profile showing a flattening of the intertidal swash bar and runnel profile. Note that the initial profile (red line) was measured on the 19th of September. The figure also includes the positions of the four tripods P1-P4.
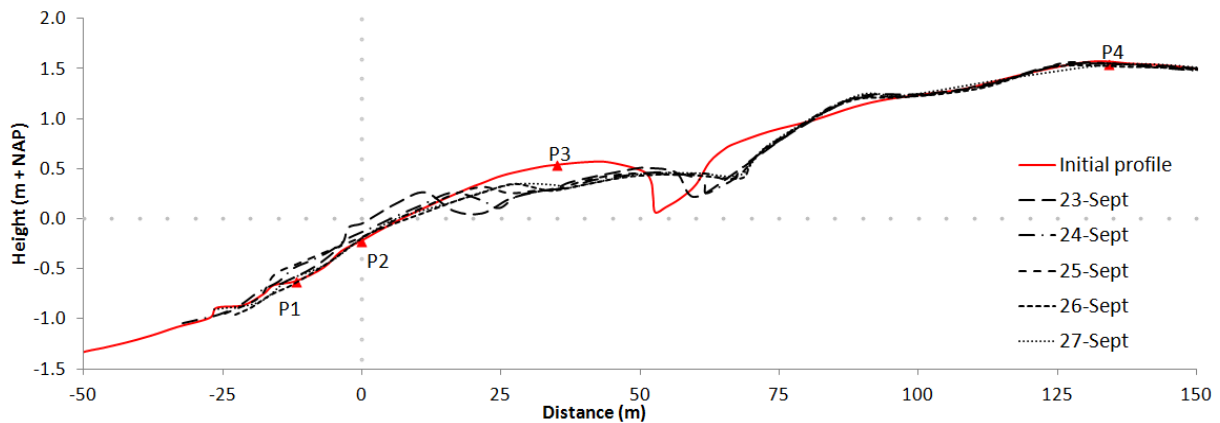
Figure 4.3: Changes in beach plain profile, focussing on the seaward facing side of the beach plain, showing a more detailed image of the onshore migration of the swash bar.

4.2.2 Inundation during first storm causing overwash processes

The last profiles of the beach plain, prior to the first storm, were recorded on the 28th and 29th of September showing no marked morphological changes (Figure 4.4). On the 3rd of October wind speed increased significantly (Figure 4.1a) resulting in the first storm that was recorded during the fieldwork period. High wave conditions prevailed during this storm that took place from the 3rd to the 5th of October (Figure 4.1d). Throughout the storm spring tide was accompanied by high storm surge levels causing the entire beach plain to inundate in the morning of the 4th of October reworking the entire cross-shore profile. The post-storm profile, mapped on the 7th of October, shows that the old swash bar and runnel had disappeared and a new swash bar was generated landward of tripod P2. Furthermore, due to overwash processes a lot of sediment was eroded on the seaward side of the beach plain crest (seaward of tripod P4), and deposited on the landward side pointing to large scale onshore sediment transport. The period that is chosen for the investigation of the suspended sediment transport mechanisms during high wave conditions is from the 4th till the 5th of October, henceforth HWC1.
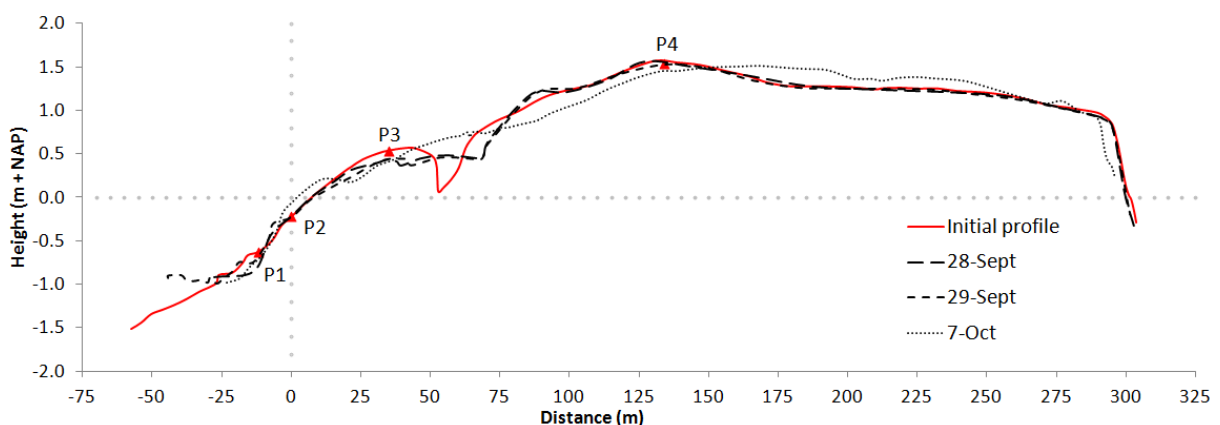
Figure 4.4: Vast morphological changes were recorded on the beach plain profile due to inundation during the first storm. Note that beach profiles were not mapped from the 30th of September till the 6th of October.

25

4.2.3 Erosion of high-water areas during second storm

The second storm occurred at 16th and 17th of October. The first profile that can be displayed prior to the storm was mapped on the 13th of October (Figure 4.5). DGPS data was recorded on the 14th and 15th of October, however this data cannot be used because it did not contain coordinates of tripod P2 which was used as a reference position for all the other profiles shown in this paragraph. On the 16th of October wind speeds were high generating high offshore waves (Figure 4.1a, d). Because these conditions coincided with a spring tide it was suspected that the beach plain would inundate. Due to little to no set-up in water surface level this did not happen. However, the profile mapped on the 17th shows that the swash bar disappeared flattening the profile. Therefore, it can be concluded that the waves reached high enough to rework the seaward part of the beach plain, though this time the sediment was not deposited on the landward side because the beach plain did not inundate. To elucidate the morphological change after this storm suspended sediment transport is analysed in the period of the 16th and 17th of October, hereafter HWC2.
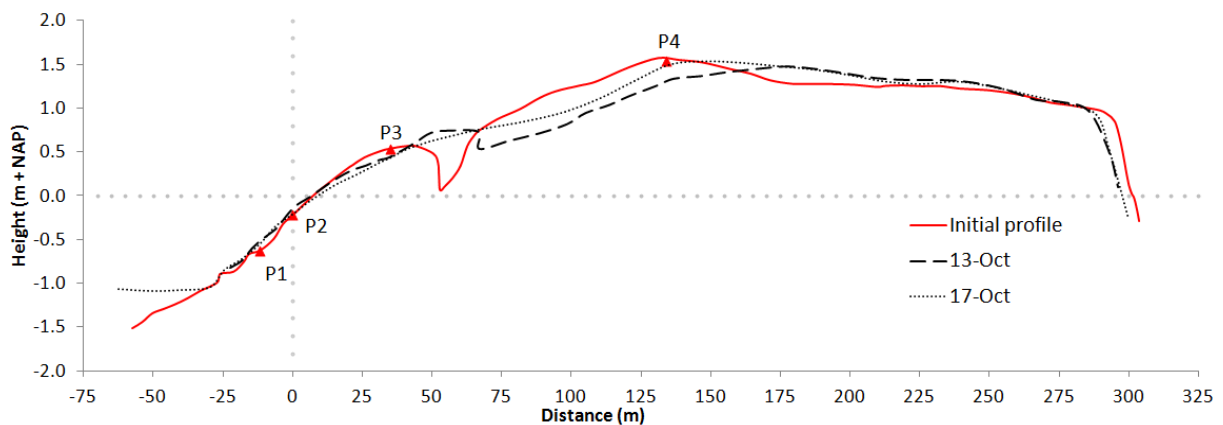
Figure 4.5: The second storm only shows a change in profile at the high water area on the seaward side of the beach plain.

4.2.4 Little morphological change during remainder of fieldwork period

The weather on the remainder days of October was tranquil and little to no change in bed level was observed in the field. However, subtle morphological changes along the intertidal beach plain profile were recognized when plotting the DGPS profiles (Figure 4.6 and Figure 4.7). In the second to last week of the fieldwork period, 19th to 25th of October, sediment was eroding seaward of tripod P1 and between tripods P1 and P2 (Figure 4.6). Sediment deposition was taking place further along the beach plain, namely 15 meters landward from tripod P2 up to 60 meters from P2, pointing to onshore sediment transport. This process of erosion and deposition continued throughout the last week of October (Figure 4.7). However, the location of sediment erosion shifted landward and concentrated around tripod P2. From the 29th to the 31st of October a new swash bar with a little runnel had developed. The erosional and depositional processes discussed above resulted in a steepening of the intertidal profile. The period that is chosen to investigate which sediment transport mechanisms are responsible for these subtle morphological changes is from the 28th till the 31st of October, henceforth LWC2.
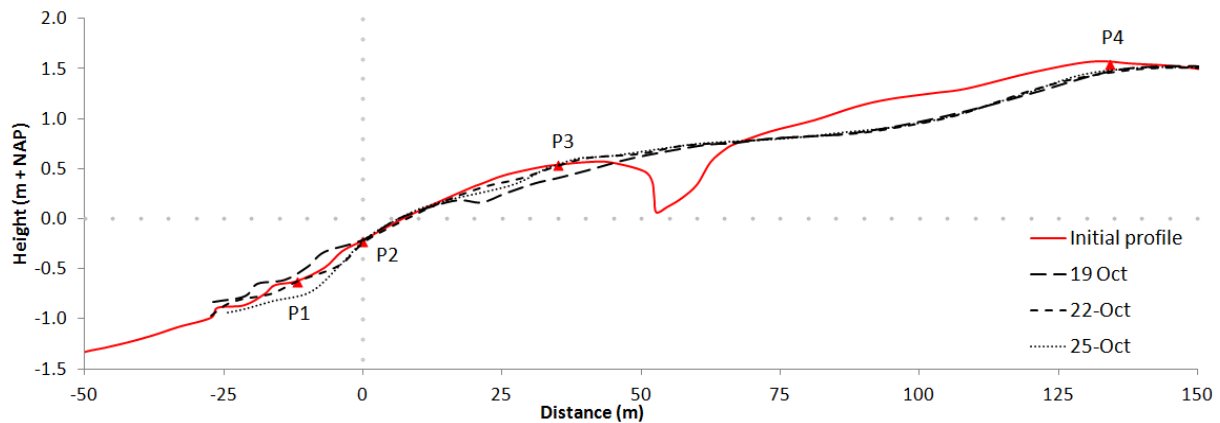
Figure 4.6: Little to no morphological change occurred during the second to last week of the fieldwork period (19th till 25th of October).
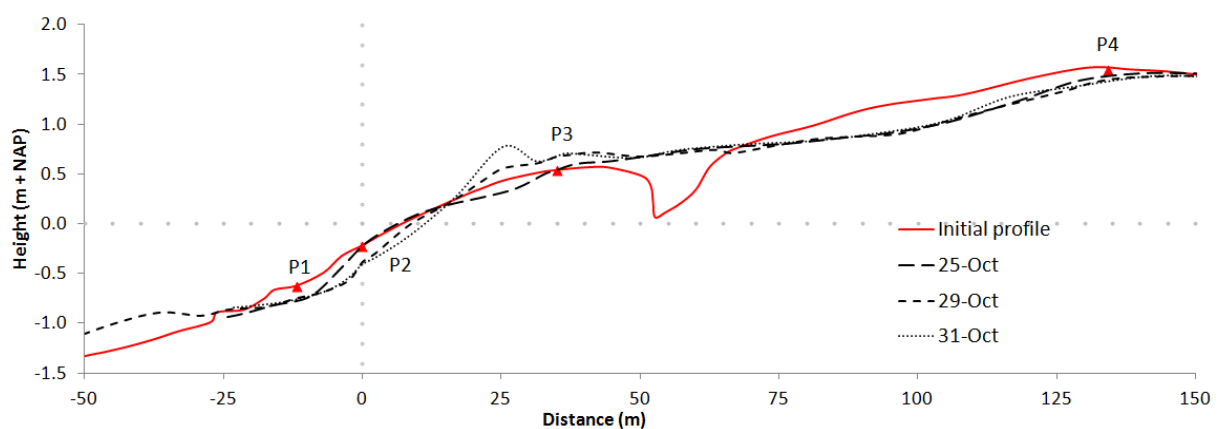

Figure 4.7: Little to no morphological change occurred during the last week of the fieldwork period (25th till 31st of October).

4.2.5 *Depth of activity rods*

Another way to detect changes in bed level is by use of depth of activity rods. The intertidal part of the cross-shore profile was monitored on a daily bases (Photo 3-3). The daily bed level change of the whole intertidal profile (having a length of ± 65 m from tripod position P1 landwards) was calculated via linear interpolation of bed level change between rods (21 in total) and multiplying by the distance between rods. Several erosion and accretion events were observed during the measurement period, but the daily bed level change was generally small (Figure 4.8). The main erosion events occurred at the 4th of October and at the 17th and 18th of October. These data exactly correspond to the two most extreme high wave events that took place during the fieldwork (HWC's 1+2). As mentioned earlier both cases show a flattening of the beach plain profile during these events. The daily bed level change measured with depth-of-activity rods on the 17th of October was more than twice as much as the bed level change on the 4th of October (Figure 4.8). The reason for this is that water levels on the 17th of October were lower compared to the 4th of October and therefore the beach plain is affected more by breaking waves generating undertow, hence a higher bed level change on the 17th of October. The major accretion event occurred at the 13th and 26th of October (Figure 4.8), which is consistent to the observed bed level change. On the 13th of October 10-20 cm of sediment was deposited at the intertidal zone of the cross-shore profile

27

and the newly formed swash bar had migrated landwards and was now located at the former runnel (Figure 4.5). On the 26th of October a new swash bar had formed with its crest approximately located at tripod P3. High winds from the north and high offshore waves on the 24th and the 25th of October resulted in a relatively high set-up causing this change in morphology (Figure 4.1a, d and h). The weather on the remainder days of October was tranquil and little change in bed level was observed. A final profile was mapped on the 31st of October (Figure 4.7). A cumulative bed level change of - 8 m³/m was measured over the intertidal profile at the end of the fieldwork, which means more sediment was eroded than accreted during the course of the fieldwork. When inspecting the changes in beach plain profile caused by the two high wave events (Figure 4.4 and Figure 4.5), it can be concluded that this sediment was deposited on the landward side of the beach plain.
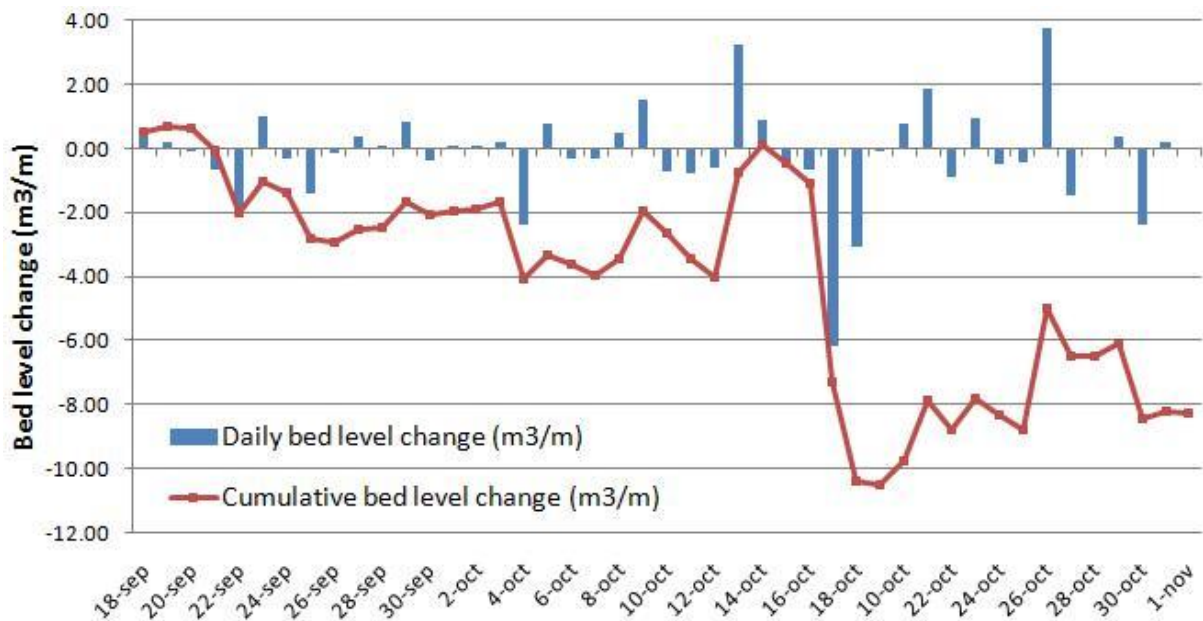
Figure 4.8: The daily- and cumulative bed level change measured with depth-of-activity rods from 18 September to 1 November 2009. Note that the rods were not surveyed at the 28th of October and 1st of November.

28

4.3 Local hydrodynamics

The fieldwork period is characterized by four distinctive periods of morphological development, as previously mentioned in section 4.2, and therefore further data analysis is focussed on these four periods, namely LWC's 1+2 and HWC's 1+2. The local wave condition and mean currents will be discussed in the following sections.

4.3.1 Wave conditions

The wave conditions during the field campaign are shown in Figure 4.9. The significant wave heights at an offshore location 'Wadden Eierlandse Gat' (Hs_Offshore; black line) and at the four measuring positions P1-P4 (Hs_P1 - Hs_P4; red, green, blue and yellow line respectively) are plotted in one graph to differentiate between various wave conditions that occurred during the fieldwork period. The offshore wave heights are 10-min averaged out of a 30-100 MHz spectrum and wave heights P1-P4 are 10-min averaged out of a high-frequency (0.04 < f < 1 Hz) spectrum. The significant wave heights of the four measuring positions (P1-P4) evidently follow the pattern of the offshore significant wave height. The offshore significant wave height shows two peaks that stand out in Figure 4.9, i.e. HWC1 on the 4th of October with maximum Hs_Off of 5.0 m and HWC2 on the 16th of October with maximum Hs_Off of 5.8 m (Table 4-1). The significant wave height at tripod P4 was only measured during the first high wave event (HWC1) because only then did the entire beach plain inundate. From the 12th to the 15th of October measurements at tripod positions P2 and P3 lack because water levels did not reach these tripods due to a set-down which leaded to low water levels (Figure 4.1h).
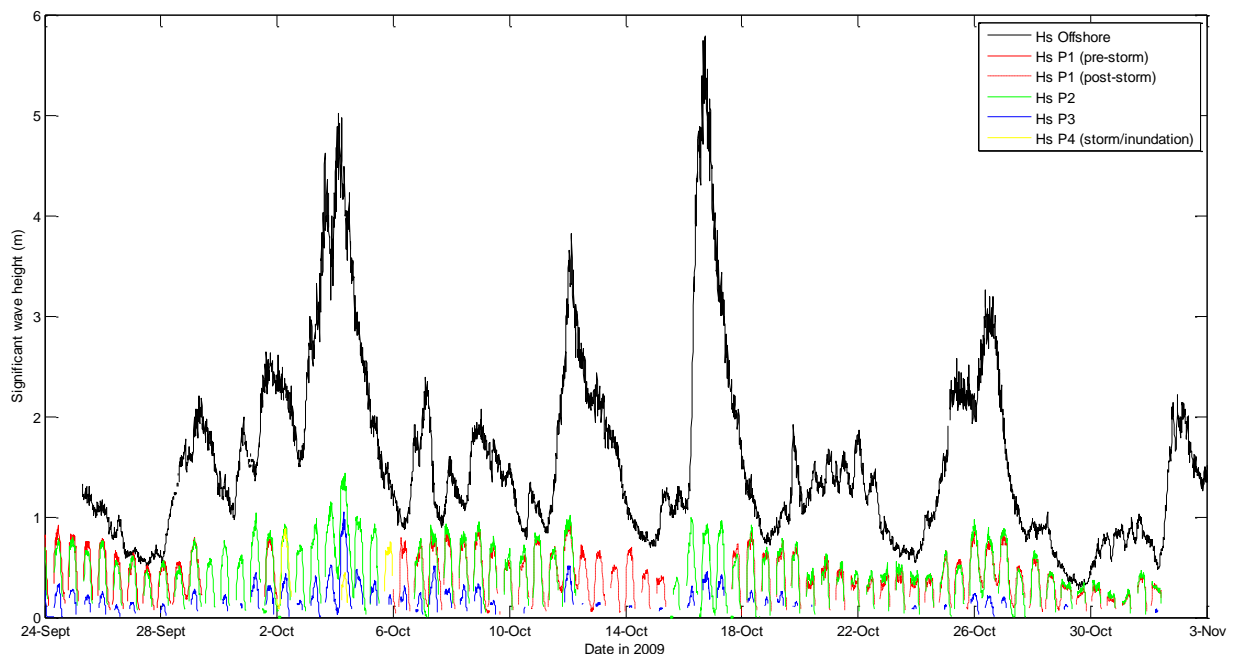
Figure 4.9: Significant wave height during the fieldwork campaign (24 September – 1 November) at five positions: offshore measuring station 'Wadden Eierlandse Gat' and the measuring positions P1-P4. Note that data acquired in the first week of the fieldwork period (17 – 23 September) contained errors and is not included in Figure 4.9.

Table 4-1: Minimum, mean and maximum offshore wave height and wave period calculated for the entire fieldwork period (18 Sept − 1 Nov) and calculated for the four periods that were researched in detail (LWC's 1+2 and HWC's 1+2).

	Date in 2009	Hs_Offshore (m)			Ts_Offshore (s)		
		min	mean	max	min	mean	max
	18 Sept − 1 Nov	0.3	1.5	5.8	3	4.7	8.6
LWC1	25 − 28 Sept	0.5	0.8	1.3	3.5	4.4	5.3
LWC2	28 − 31 Oct	0.3	0.6	1.1	3.1	4.0	6.2
HWC1	4 − 5 Oct	2.4	3.7	5.0	5.8	6.6	7.6
HWC2	16 − 17 Oct	1.0	3.6	5.8	3.8	6.3	8.6

The offshore water height (h) and the offshore astronomical water height (h Ast) are given in Figure 4.10. The figure clearly illustrates high storm surge levels during HWC1 and that storm surge levels were not reached during HWC2. This is in line with the field observations, that is, the beach plain did not inundate.
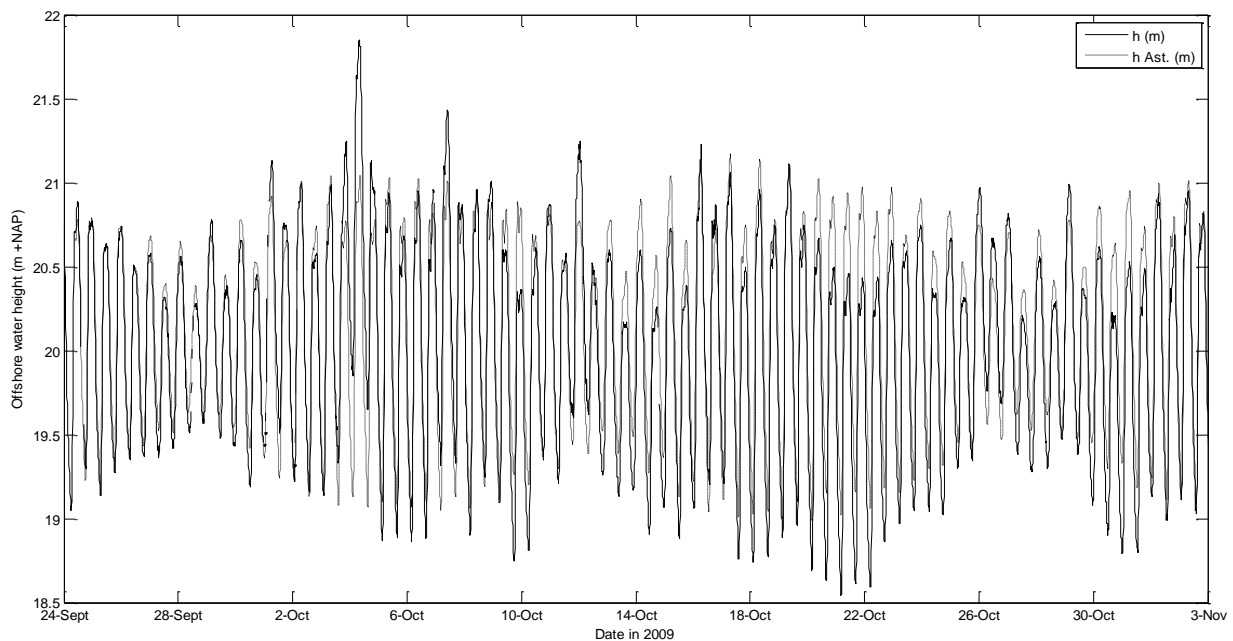
Figure 4.10: Offshore water height and offshore astronomical water height at measuring station 'Wadden Eierlandse Gat'.

The water depth (*h*), significant wave height (*Hs*) and the relative wave height (*Hs/h*) for low and high wave conditions are illustrated in Figure 4.11 and Figure 4.14, respectively. Significant wave heights range from 0.2-0.8 m during LWC1 and from 0.2-0.6 m during LWC2 (Figure 4.12a, b). During LWC1 *Hs* decreases shoreward signifying that waves are breaking between P1, P2 and P3. During LWC2 *Hs* does not decrease between P1 and P2 which means waves are not breaking between P1 and P2, but *Hs* does decrease from P2 to P3 indicating waves are breaking between P2 and P3. The pattern of the significant wave height fluctuates coherently with the tide which is another indication that waves are breaking. This tidal modulation of *Hs* can be seen during LWC1 and the first part of LWC2 (Figure 4.11a, b). During the second part of LWC2 (29th to 31st of October), *Hs* is constant indicating that waves are no longer breaking. The relative wave height is of interest because of its usability as a breaker criterion (Osborne & Greenwood, 1992b). Initiation of short-wave breaking occurred

at a value of *Hs/h* ≈ 0.4 and fully saturated breaking conditions occurred at a value of *Hs/h* = 0.55. During LWC1, *Hs/h*-values are larger than 0.55 (see Figure 4.13a) also indicates that waves were fully broken at positions P1 and P2. Waves are also breaking at position P3, but show lower *Hs/h*-values (*Hs/h*≈0.4; see Figure 4.13a), because most waves have already broken resulting in a lower *Hs* hence a lower *Hs/h*. During LWC2 there is a shift from saturated breaking conditions on the 28th of October to non-breaking conditions (*Hs/h* < 0.4) from the 29th till the 31st of October. This might be caused by a decrease of wave input from deeper water. Note the low offshore wave height measured during the 29th of October Figure 4.1d. Furthermore, a water height of 1.7 m was measured during the 29th of October which is 0.5 m higher compared to the water height measured on the 28th of October, resulting in fewer to no wave breaking from the 29th onwards. The relative significant wave height increases shoreward as can be expected (Figure 4.13b). Note that measurements become unreliable when water levels drop below 0.2 mab (mab = meters above bed).
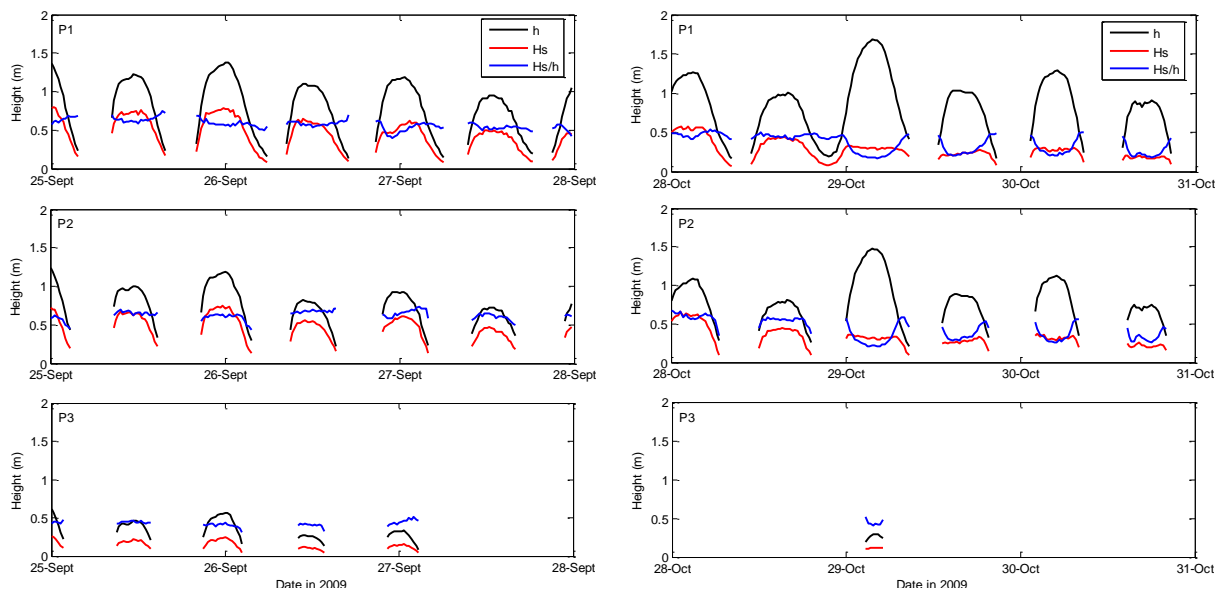
Figure 4.11: Water depth, significant wave height and relative significant wave height for **a:** LWC1 and **b:** LWC2 at positions P1 to P3.
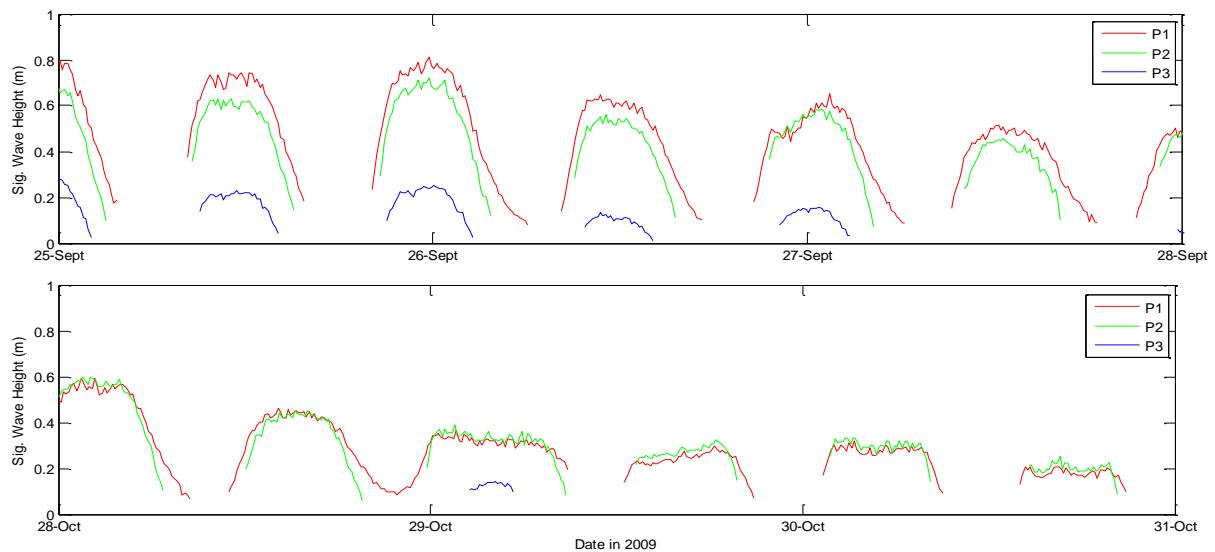
Figure 4.12: Significant wave height at positions P1 to P3 for **a:** LWC1 and **b:** LWC2.
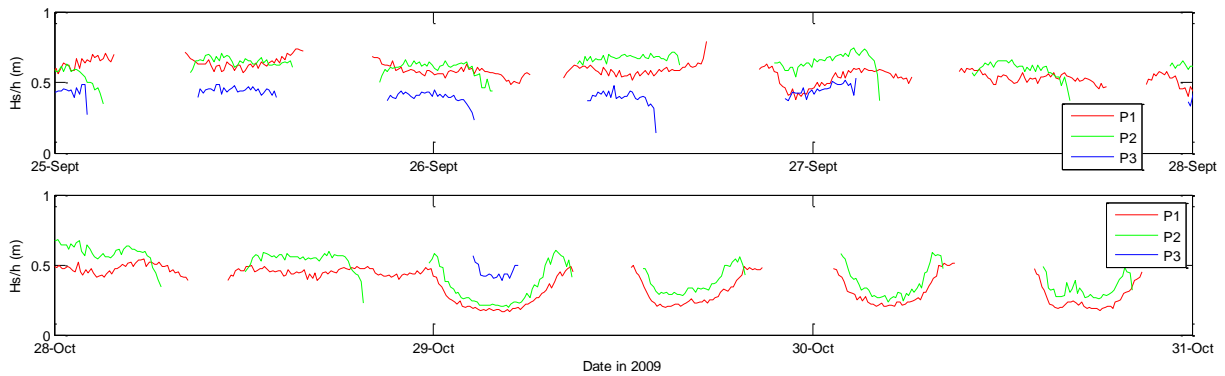
Figure 4.13: Relative significant wave height at positions P1 to P3 for **a:** LWC1 and **b:** LWC2.

Significant wave heights during high wave conditions show strong cross-shore variability. There is a clear landward decrease in wave height (Figure 4.14), again through the process of wave breaking. During HWC1 *Hs* at position P2 ranges from 0.2-1.4 m, at P3 from 0.2-0.9 m and at position P4 from 0.2-0.45 m. Wave heights during HWC2 are visibly lower and range from 0.1-0.9 at position P2 and from 0.1-0.45 at position P3 (Figure 4.14a, b). Notice that P4 is not inundated during HWC2. This can be ascribed to a set-down of 40 cm during HWC2 compared to a high set-up of 90 cm during HWC1 (see section 4.1). The relative wave heights in both high wave periods mainly have a value of *Hs/h* > 0.55 which means the waves are in fully saturated conditions. In addition, the magnitude of the significant wave height is affected by the occurrence of neap or spring tide. Both low wave conditions occurred near a period of neap tide and both high wave conditions occurred during spring tide.
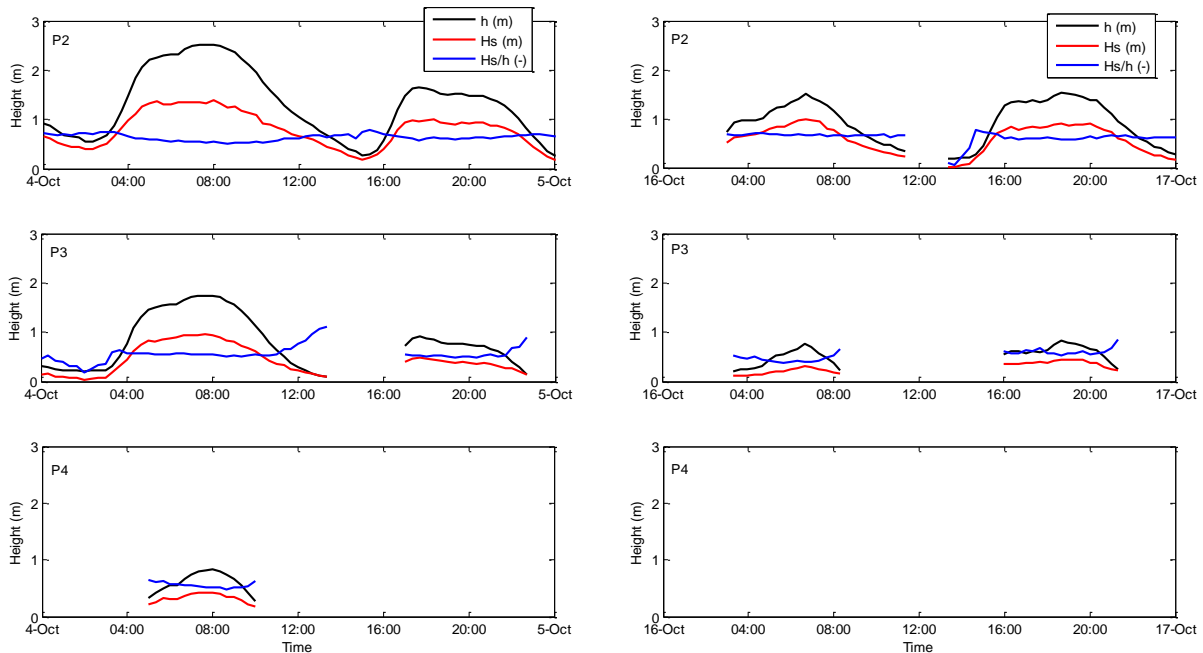
Figure 4.14: Water depth, significant wave height and relative significant wave height for **a:** HWC1 and **b:** HWC2 at positions P2 to P4.

4.3.2 Mean currents

The mean cross-shore velocity (*u*) and longshore velocity (*v*) for low and high wave conditions are presented in Figure 4.15 and Figure 4.16, respectively. Positive/negative

32

cross-shore velocities are onshore/offshore directed and positive/negative longshore velocities are northward/southward directed. The mean cross-shore velocities during LWC1, Figure 4.15a, are offshore directed at position P1 and P2 and therefore undertow dominated with an average velocity of 0.15 m/s and onshore directed at position P3 with an average velocity of 0.1 m/s. The mean longshore velocity during LWC1 show a larger variation in flow velocity and flow direction and has a higher maximum flow velocity ($v \approx 0.4$ m/s) than the maximum cross-shore velocity. An alteration in wave angle approach is likely the basis for a change in direction of the longshore current. On the 25th of September waves approached the shoreline[3] at an angle of 320˚ (Figure 4.1c) as a result generating a southward directed longshore current at P1 and P2. On the 26th of September the wave angle changes to 260˚ causing a shift in direction of the longshore current at P2. Furthermore, the change in direction of the mean currents u and v at position P3 can be indicative for horizontal cell circulation which occurs when water overtops the berm crest (Figure 3.1) and flows though the runnel, located slightly landward of P3 (Photo 3-1), to be discharged to the sea via the main channel of The Slufter.
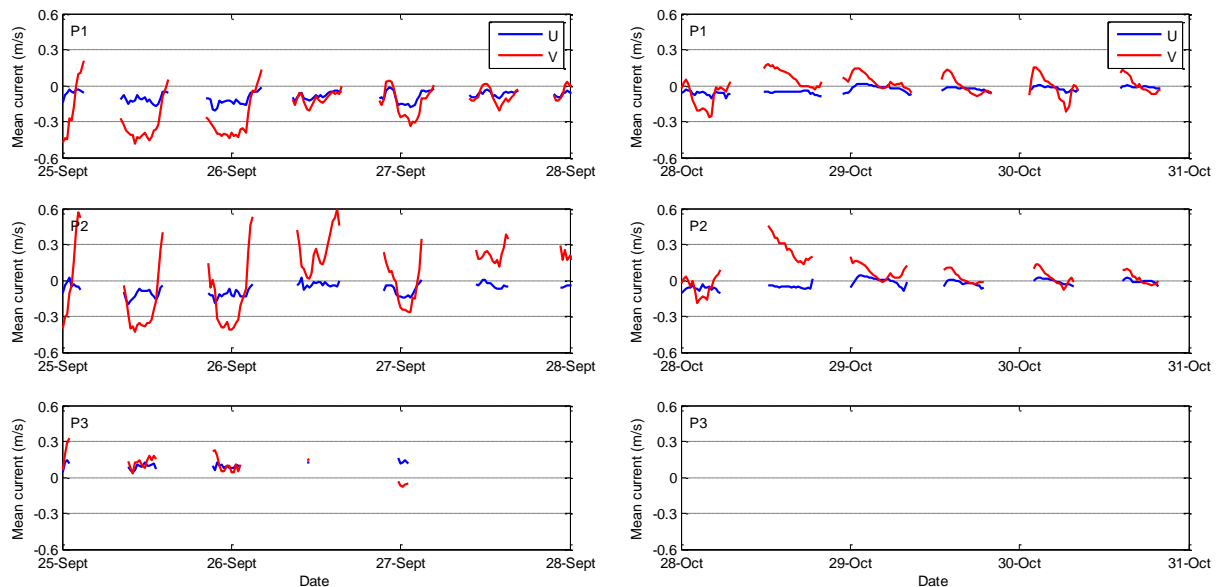
Figure 4.15: Mean cross-shore and longshore current during **a:** LWC1 and **b:** LWC2 at positions P1 to P3.

The mean cross-shore velocities during LWC2, Figure 4.15b, are offshore directed at 28 October, but change to onshore direction from the 29th of October. This change can be explained by an increase of water depth on the 29th causing waves to stop breaking, which is in accordance with low relative wave heights, and diminishing the undertow. The mean longshore current from the 29th onward shows a northward directed current during the flood cycle of the tide, southward directed current during the ebb cycle and in between reaching slack tide just after high tide. This is a typical pattern caused by the in- and outflow of The Slufter's channel. Overall, both u and v velocities during LWC2 are weaker compared to LWC1.

---

[3] The shoreline at The Slufter is oriented NE-SW by 30 degrees.

Mean cross-shore currents during HWC1 fluctuate in on- and offshore direction at positions P2 and P3, however undertow became more dominant during the second half of the tidal cycle (Figure 4.16a). During HWC1 the crest of the beach plain became inundated for the first and only time, hereby inundating tripod P4 (Figure 3.1). A clear onshore directed mean current is visible at P4 indicating the presence of overwash processes. Cross-shore flow velocity nearly reached 1 m/s, which is 10 times larger than during low wave conditions. The mean longshore velocities fluctuate in north- and southern directions at positions P2 and P3 with velocities of 0.5 m/s and is northward directed at position P4 with velocities of 0.5 m/s. The pattern of the mean current at tripods P2 and P3 corresponds to the pattern seen at LWC2, indicating that the in- and outflow of The Slufter's channel also influences the direction of the cross- and longshore currents during HWC1. Mean cross-shore currents are offshore directed at positions P2 and P3 during HWC2, Figure 4.16b, with values of 0.2 and 0.4 m/s, respectively, indicating the presence of undertow. During HWC2 the waves approach the shoreline with an angle of 30˚ (Figure 4.1c), resulting in a dominantly southward directed mean longshore currents. Maximum values of longshore current of 0.75 m/s at position P2 and 0.3 m/s at positions P3 were reached.
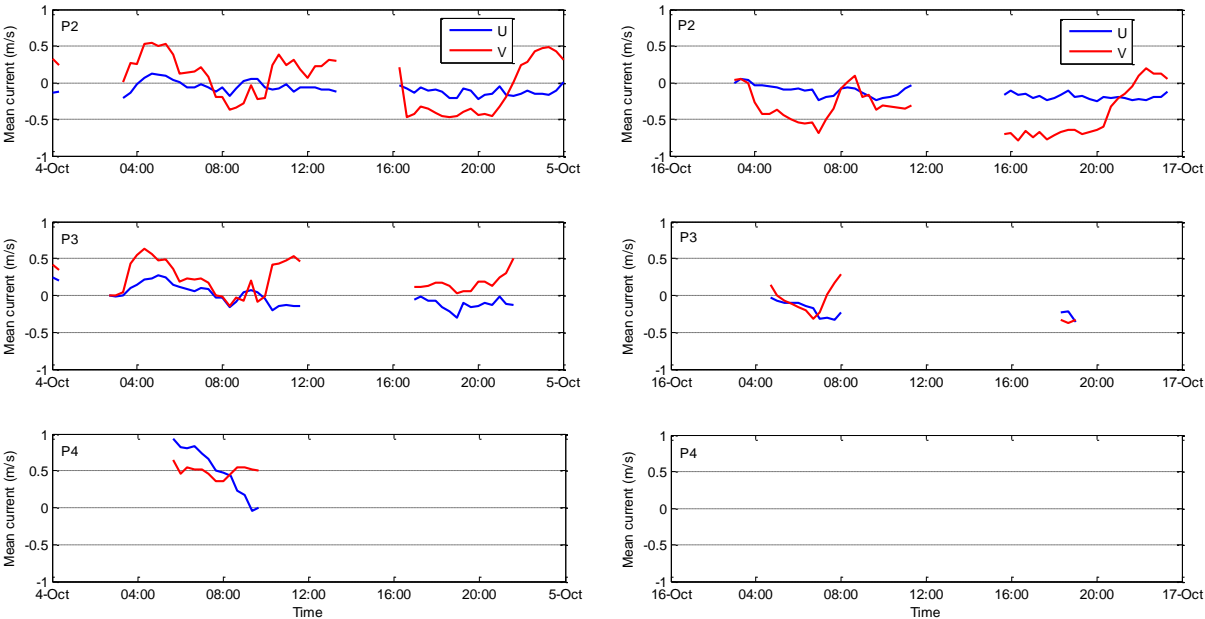
Figure 4.16: Mean cross-shore and longshore current during **a:** HWC1 and **b:** HWC2 at positions P2 to P4.

4.4 Cross-shore suspended sediment transport

The following sections will discuss the correlation between cross-shore velocity and concentration, the cross-shore sediment fluxes (high- and low frequency flux, mean flux and net flux) and their relative contribution and the results of the spectral analysis.

4.4.1 Cross-shore velocity and concentration

Three time series of detrended low- and high frequency cross-shore velocity and suspended sediment concentrations at all three OBS sensors heights (c_1 = lower, c_2 = middle and c_3 = upper sensor) are selected to investigate the occurrence of a coupling between long low-frequency (infragravity) waves and sediment concentration bursts in the water column. The suspended sediment concentration data has been inspected before selecting the time series described below. The ssc-data show abnormal large values during the initial stage of rising tide and the final period of falling tide. Because the water depth is small during these periods the wave rollers, containing air bubbles, can reach the OBS-sensors and due to these bubbles the OBS-sensors will mistakenly record high sediment concentration. Therefore, it was chosen to select the time series during high tide, minimizing false values of suspended sediment concentration. In addition, the ssc-data series that are selected were retrieved from the data that was recorded after the tripods were correctly repositioned on the surface which was done after daily data collection. It is often observed that the three OBS instruments did not get burrowed in the sand during the first tidal cycle recorded after repositioning the tripods.

The first time series that will be discussed was documented during LWC1 on the 27th of September from 00:34h to 00:40h at position P1 (Figure 4.17). These six minutes were randomly chosen. The thick line in Figure 4.17a represents the low-frequency part of u. There are no clear characteristics of a bound long wave visible. If this was the case you would expect troughs under all high waves and crests under all low waves. However, a trough is visible during low waves at one thirds of t = 00:35. Furthermore, the lack of bound long waves can be suspected because surf zone conditions occurred at that time ($Hs/h \approx$ 0.55), where bound long waves disintegrate in the surf zone due to wave breaking. The concentration bursts coincide with the passage of high waves e.g. slightly before t = 00:35, t = 00:36, one fourth of t = 00:36, one thirds and two thirds of t = 00:38 and three fourths of t = 00:39. The suspended sediment concentration bursts predominantly reach the bottom two OBS sensors and hardly reach the upper sensor. Three concentration bursts were simultaneously observed at all three sensor heights e.g. slightly before t = 00:35 with values of 18, 14 and 3 kg/m^3 for c_1, c_2 and c_3 respectively, at two thirds of t = 00:38 with values of 14, 6 and 3 kg/m^3 for c_1, c_2 and c_3 respectively and at three fourths of t = 00:39 with values of 22, 10, 4 kg/m^3 for c_1, c_2 and c_3 respectively. The concentration bursts all coincide with the passage of large gravity waves indicating that these waves are responsible for sediment suspension.
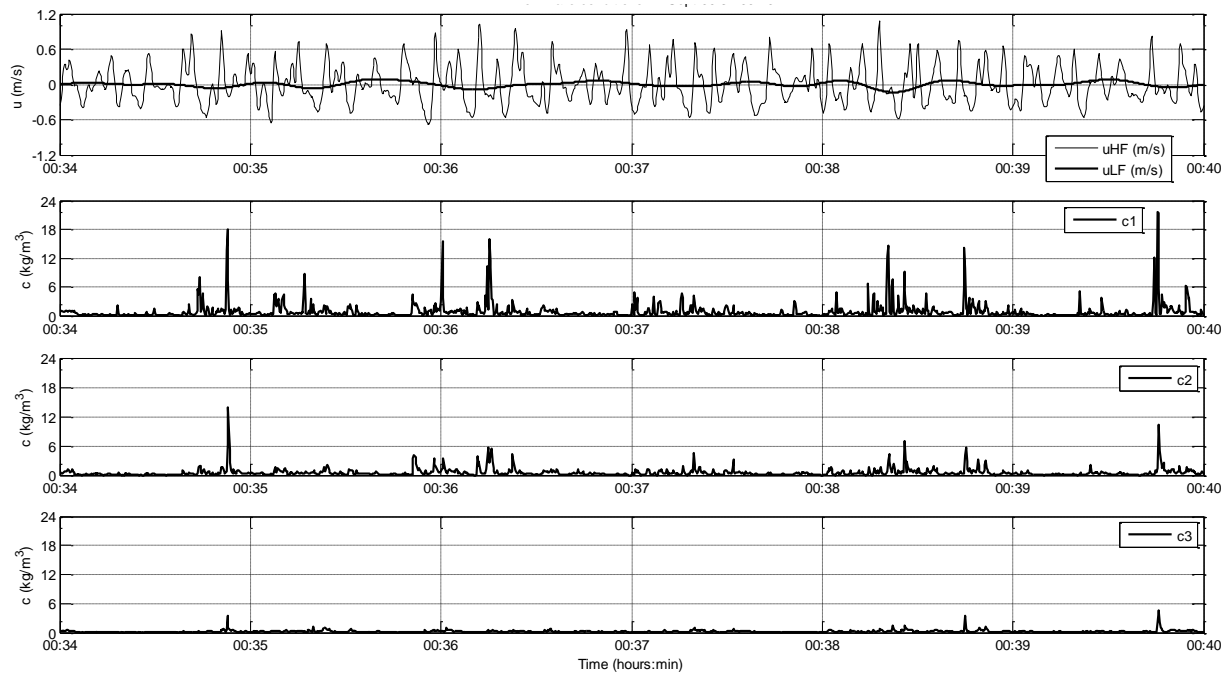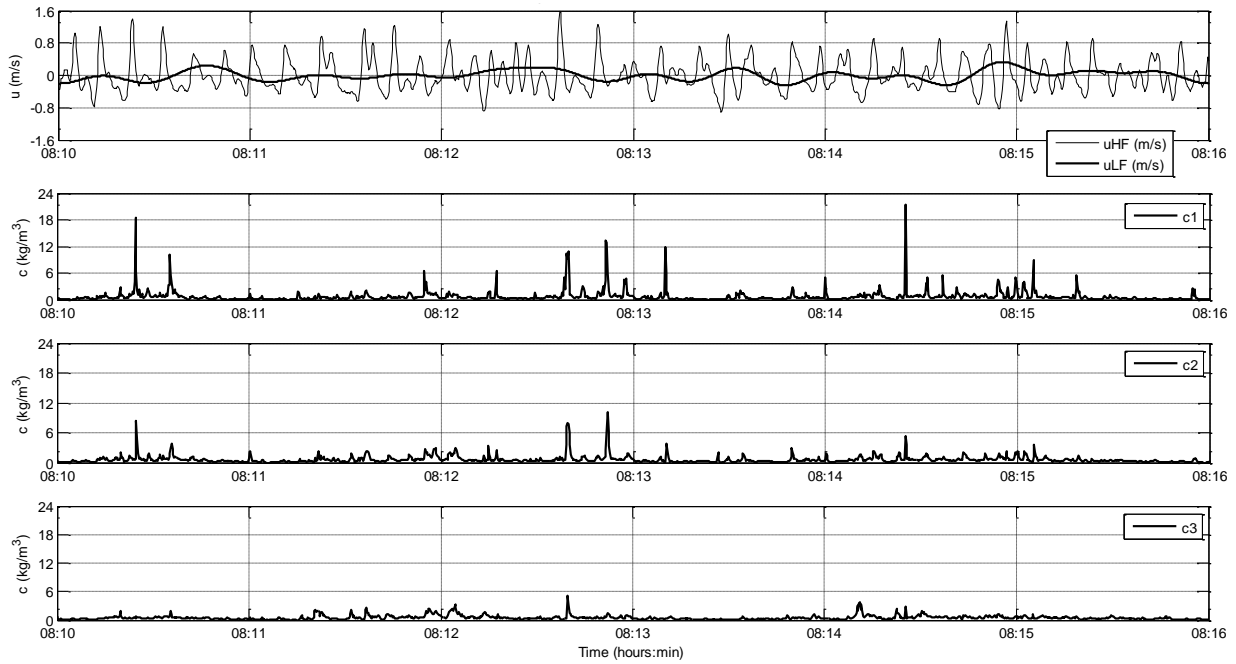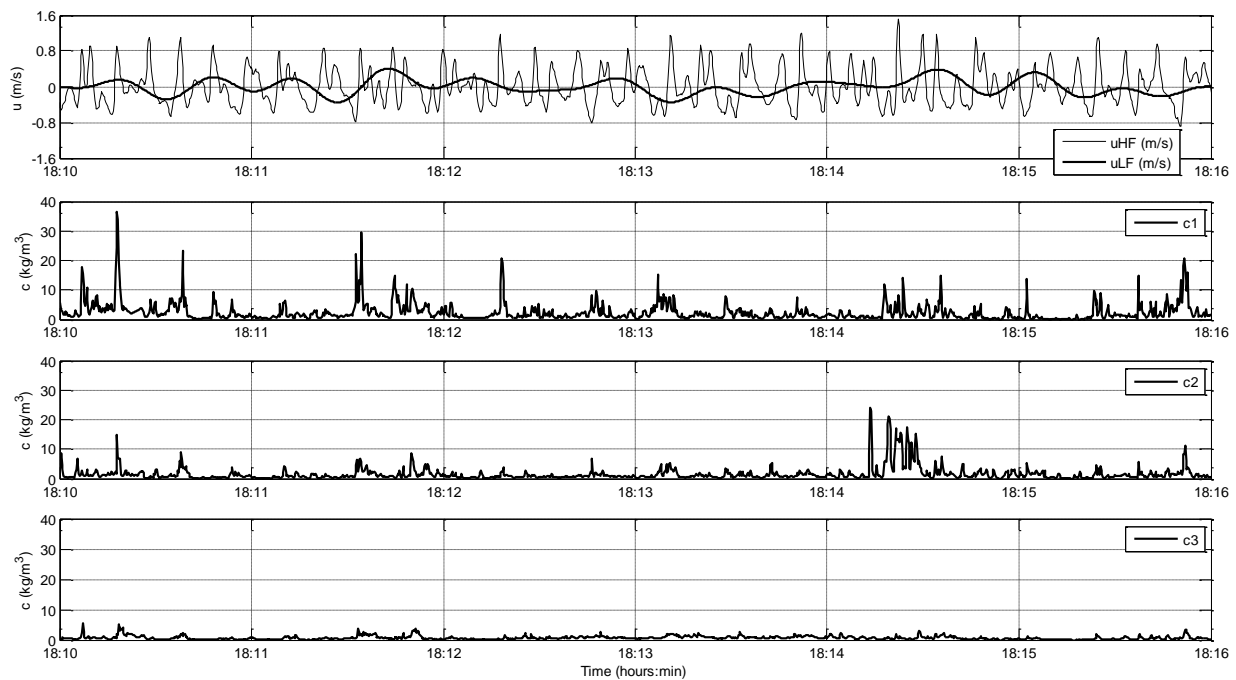
Figure 4.17: a: Low- and high frequency cross-shore velocity and **b-d:** concentration (c1-c3) during LWC1 on the 27th of September from 00:34h to 00:40h at position P1.

The second and third time series that will be discussed were documented during HWC1 on the 4th of October from 08:10h to 08:16h and from 18:10h to 18:16h both at position P2 (Figure 4.18 and Figure 4.19). There are several reasons why this tripod was selected. First of all, during HWC1 the OBS sensor nearest to the bottom at tripod P3 was often burrowed in the sand giving a value of 0 g/L and therefore not useful for analyses. And secondly, OBS measurements at tripods P3 and P4 were often distorted by air bubbles during HWC1 giving unrealistically large ssc-values. The second time series from 08:10h to 08:16h also illustrates a randomly selected time series. A bound long wave is visible showing wave troughs under high waves e.g. halfway of t = 08:10, three fourth of t = 08:12 and wave crests above low waves e.g. three fourth of t = 08:10 and one third of t = 08:12 (Figure 4.18). Once again the suspension events coincide with the passage of high waves (e.g. two bursts halfway t = 08:10, two bursts at three fourth of t = 08:12 and one bursts halfway t = 08:14). The values of suspended sediment concentration in this time series (Figure 4.18) are in the same order of magnitude as the ssc-values recorded at LWC1 (Figure 4.17). This is contradictory to what you might expect. HWC1 is characterized by higher significant wave height (Hs_{mean_Off} = 3.7m during HWC1 compared to Hs_{mean_Off} = 0.8m during LWC1; Table 4-1). Higher waves penetrate deeper into the water column, suspecting more sediment to be stirred and suspended during HWC1. The reason why this is not the case is because the water depth of the time series recorded during HWC1 (08:10h to 08:16h) is twice as deep (h = 2.5m; Figure 4.14) as the water depth during LWC1 (h = 1.2m; Figure 4.11). However, when plotting the low- and high-frequency cross-shore velocity and suspended sediment concentrations one tidal cycle further (on the 4th of October from 18:10h to 18:16h), a similar water depth is found (h = 1.5m; Figure 4.14) as for the time series selected during LWC1, and larger ssc-values are recorded (Figure 4.19). The ssc-value at the bottom sensor even recorded values

twice as large as recorded during LWC1, namely 36 kg/m^3 at one third of t = 18:10. Once more this time series demonstrates that suspended sediment bursts coincide with the passage of high waves e.g. one third and two third of t = 18:10, halfway of t = 18:11, one third of t = 18:12, one third of t = 18:14 and three fourth of t = 18:15. Furthermore, the bound long wave is even more prominent in Figure 4.19 showing wave troughs under high waves and crests under low waves. All three time series show that the suspended sediment concentration decreases with elevation above the bed.

Figure 4.18: a: Low- and high frequency cross-shore velocity and **b-d:** concentration (c1-c3) during HWC1 on the 4th of October from 08:10h to 08:16h at position P2.

Figure 4.19: a: Low- and high frequency cross-shore velocity and **b-d:** concentration (c1-c3) during HWC1 on the 4th of October from 18:10h to 18:16h at position P2.

4.4.2 Cross-shore suspended sediment fluxes and spectral analysis

The correlation between the velocity and the sediment concentration was investigated within a six minutes time span (section 4.4.1), because in this way you get a view on which waves are responsible for the sediment suspension events. This section will discuss the cross-shore suspended sediment fluxes, now zooming out to analyse the four morphologically distinctive periods, LWC's 1+2 and HWC's 1+2, to be able to correlate the sediment fluxes to the observed morphological change. The low- and high-frequency, mean and net fluxes are plotted against the relative significant wave height (Hs/h). In this way the effect of non-breaking and breaking waves on the fluxes are analysed. Furthermore, the magnitude and direction of the fluxes during low- and high wave conditions are determined. All sediment fluxes have been calculated over a period of 20 minutes. Note that the use of Hs/h presumes a 2D beach state (uniform beach without cell circulation), but because we are dealing with a 3D beach state (overwash processes and ridge/runnel systems caused by cell circulation) there is some degree of scatter in the cross-shore sediment fluxes.

The values of the suspended sediment fluxes at P1 during LWC1 are plotted in Figure 4.20. The oscillatory and mean flux measurements have Hs/h values ranging between 0.4 and 0.7, indicating that P1 experienced surf zone conditions. The high-frequency flux at all sensor heights is directed onshore with some outliers directed offshore at the lower and middle sensor. The mean flux for the lower, middle and upper sensor is offshore directed, which is consistent with the direction of the measured mean flow velocity (Figure 4.15a). Furthermore, the values of the mean flux exceeds the values of the high-frequency flux and result in a offshore directed net flux with values of 1.4, 1.0 and 0.1 kg/m^{2}s for the lower, middle and upper sensor respectively. The low-frequency flux is directed offshore at all sensor heights, but has significant lower values than the high-frequency and mean flux and is therefore of less importance to the net flux. The mean suspended sediment flux is the main contributor to the net sediment flux for all three sensors during LWC1 (Figure 4.21). The co-spectral density calculated for two tidal cycles on the 27th of September on hourly bases also illustrates an onshore directed transport at high-frequency wavelength and offshore directed transport at low-frequency wavelength (Appendix C1) which is in line with the direction of the fluxes described above. Furthermore, the accompanying variance density spectra show that the difference between the estimates of the concentration at the bottom sensor c1 and the upper sensor c3 increases when water levels rise towards high tide and decrease again when water levels drop. In other words during high tide values at c1 can be several factors higher than at c3 and during low water levels values at c1 equal c3 indicating an uniform distribution of sediment up to the upper sensor. The oscillatory and mean flux measurements at position P2 have Hs/h values ranging between 0.55 and 0.73, indicating that P2 also experienced surf zone conditions (Appendix A.1). At this position similar direction for the oscillatory and mean fluxes of all three sensor heights are found. However, the high-frequency fluxes show values twice as high compared to the high-frequency flux at P1, however the net sediment flux is still directed offshore with values of 0.9, 1.0 and 0.25 kg/m^{2}s for the lower, middle and upper sensor respectively. The contribution of the high-

frequency flux increased at position P2 (Appendix B.1) compared to position P1. The co-spectral density calculated for the first tidal cycle on the 27th of September again illustrates an onshore directed transport at high-frequency wavelength and offshore directed transport at low-frequency wavelength (Appendix C2) which is in line with the flux directions described above. This time the accompanying variance density spectra show that during the tidal cycle there is little difference between the estimates of the concentration at the lower and upper sensor. The oscillatory and mean flux measurements at position P3 have *Hs/h* values ranging between 0.38 and 0.47, indicating that waves at P3 are broken (Appendix A.2). The oscillatory and mean fluxes are onshore directed at all three sensor heights resulting in an onshore directed net flux. The net flux has values ranging from 0.08 kg/m^{2}s for the lower sensor and 0.06 kg/m^{2}s for the middle and upper sensors showing little vertical variation. The high-frequency and mean flux equally contribute to the net flux at the lower sensor (Appendix B.2). At the middle and upper sensor, however, the mean flux shows the largest contribution to the net flux. The direction of the mean flux is in line with the onshore directed mean cross-shore current at position P3 (Figure 4.15a). Furthermore, this notion together with the onshore fluxes at all three sensor heights strongly indicates cell circulation taking place at position P3. The co-spectral density calculated for the first tidal cycle on the 27th of September illustrates an onshore directed transport at high-frequency wavelength and also an onshore directed transport at low-frequency wavelength (Appendix C3) which is in line with the flux directions described above. Again there is little difference between the estimates of the concentration at the lower and upper sensor. Note that there are only few data points in Appendix A.2, because several sections of the ssc-date series did not exceed the OBS-threshold[4] during LWC1.
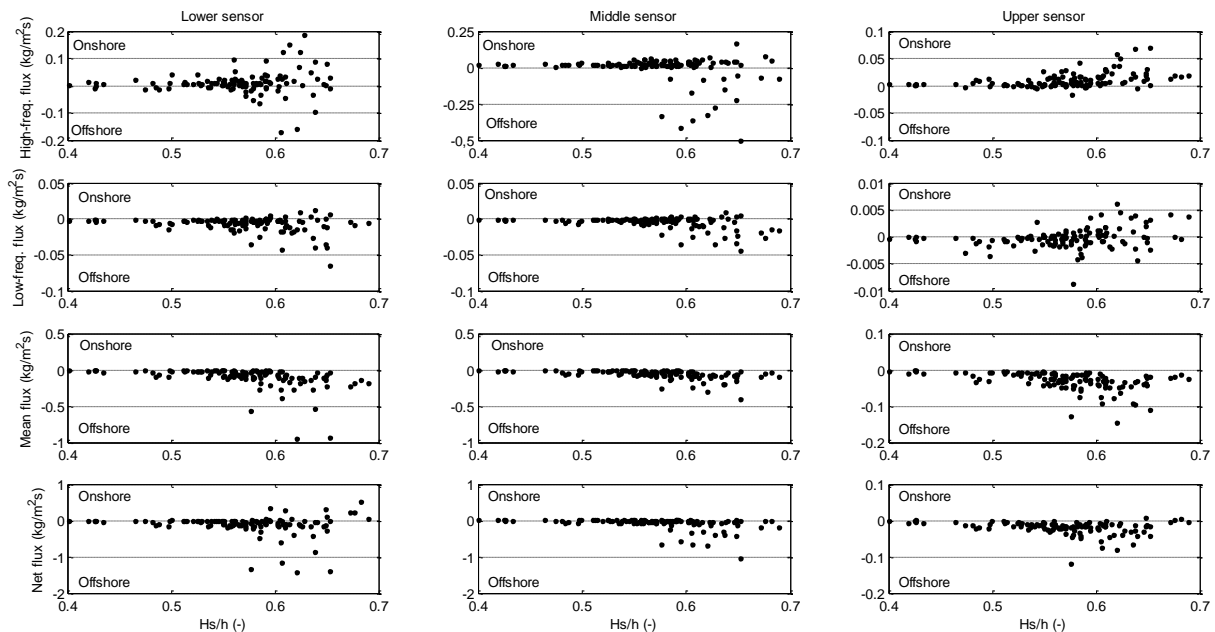
Figure 4.20: Cross-shore suspended sediment fluxes during LWC1 at **a:** lower OBS sensor (5 cmab) and **b:** middle OBS sensor (10 cmab) and **c:** upper OBS sensor (20 cmab) at position P1.

---

[4] The OBS-threshold will discard ssc-data when water levels drop below a threshold of 25cm measured above the pressure sensor.
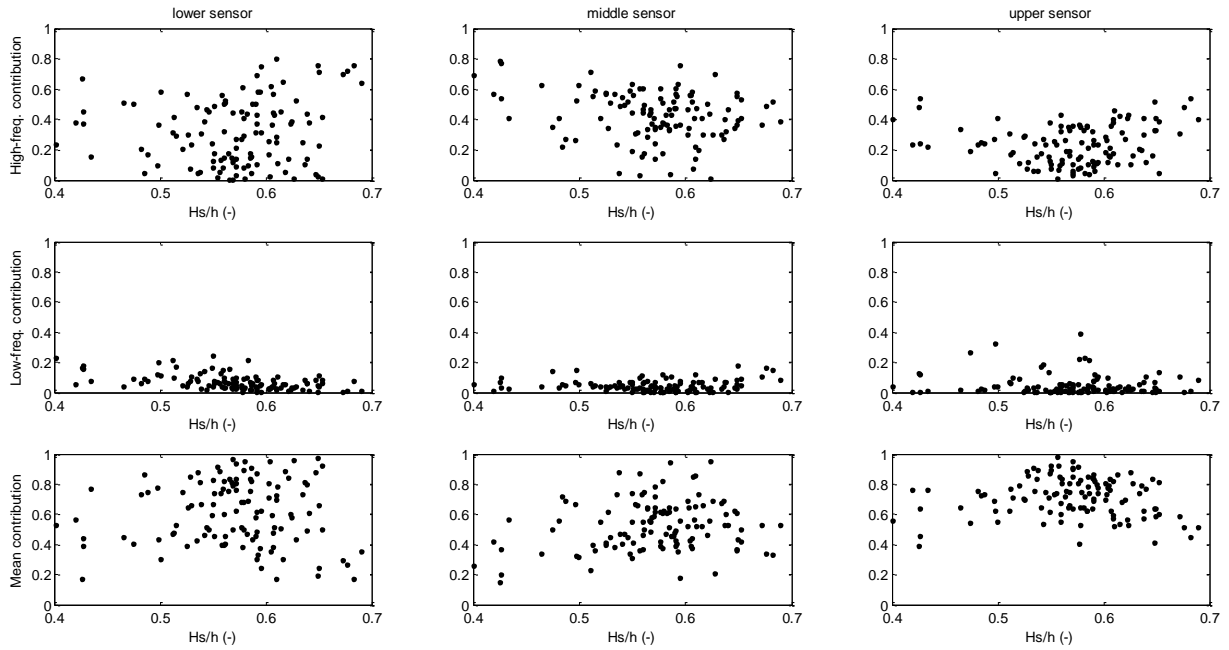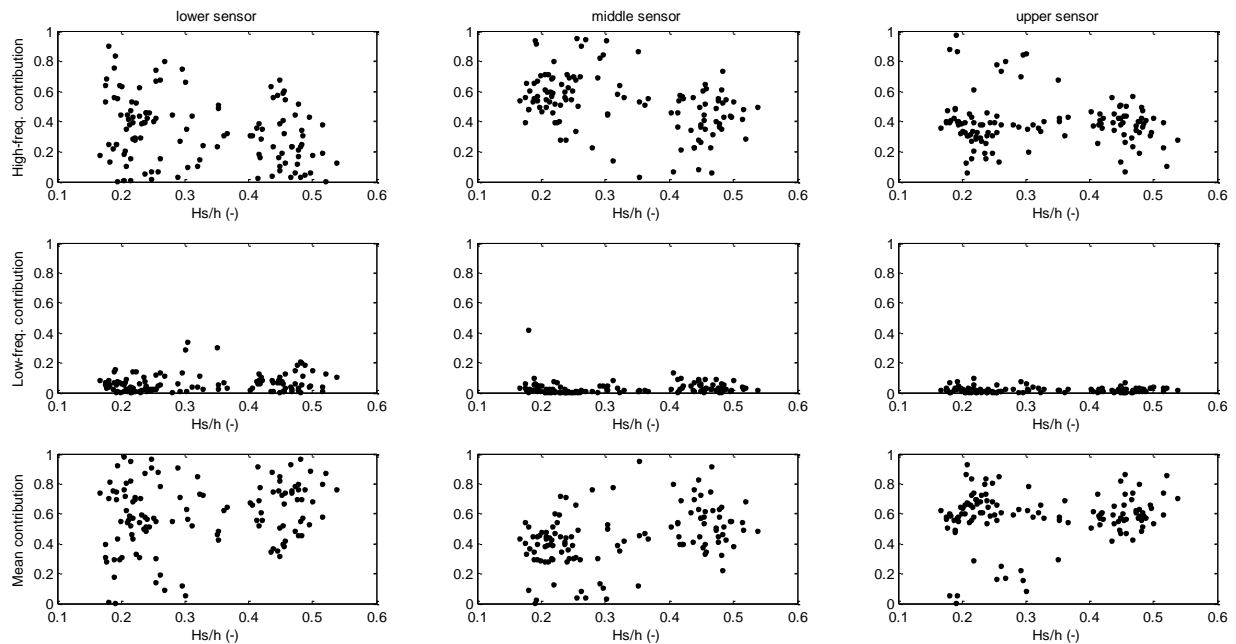
Figure 4.21: Relative contribution of high freq., low freq. and mean sediment fluxes to net flux during LWC1 at position P1.

The values of the suspended sediment fluxes at P1 during LWC2 are plotted in Figure 4.22. At first glance you can already see two differences compared to LWC1. First of all, the oscillatory and mean flux measurements were only non-zero for situations with *Hs/h* > 0.3 at the lower sensor and *Hs/h* > 0.4 at the middle and upper sensor, in other words, during situations when P1 experienced surf zone conditions. Secondly, the high-frequency flux at the lower sensor is directed offshore. This might be due to phase lags that during the onshore phase of the wave ($\tilde{u}_{crest}$) a sediment suspension cloud is created, which is transported in the offshore direction during the offshore phase of the wave ($\tilde{u}_{trough}$). Spectral analysis is applied to the velocity and concentration data to illustrate this phase lag. A 20 minute time frame on the 28th of October clearly shows that at wind wave frequencies the bottom OBS sensor (c1) has phases larger than |90˚| indicating that suspended sediment is present in the offshore phase of the wave motion (Figure 4.23d). At infragravity frequencies, the phases at all three sensor heights were larger than |90˚|. This indicates that the sediment that is stirred by the large high-frequency waves coincides with the trough (negative velocity) of the low-frequency waves which is in line with the offshore directed low-frequency flux. Furthermore, Figure 4.23b shows offshore directed co-spectra for the bottom OBS sensor at wind wave frequencies which is in line with the direction of high-frequency flux described above. The mean flux is directed offshore which is consistent with the direction of the measured mean flow velocity (Figure 4.15b). Figure 4.24 illustrates that both high-frequency and mean flux contribute to a net flux, having a value of 4.7, 3.5 and 0.7 kg/m²s for the lower, middle and upper sensor, respectively (Figure 4.22). The *Hs/h* values of the oscillatory and mean flux measurements at position P2 during LWC2 range between 0.2 and 0.7 (Appendix A.3). Low values of oscillatory and mean flux were measured at 0.2 < *Hs/h* < 0.35 indicating that sediment is also being transported under non-breaking waves.
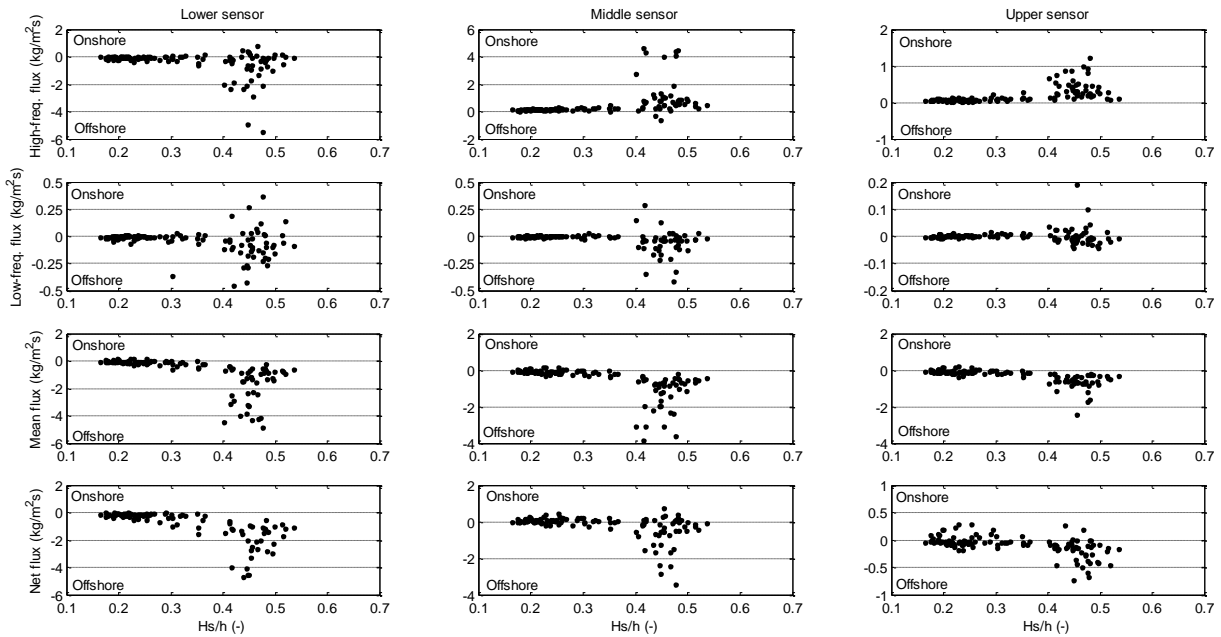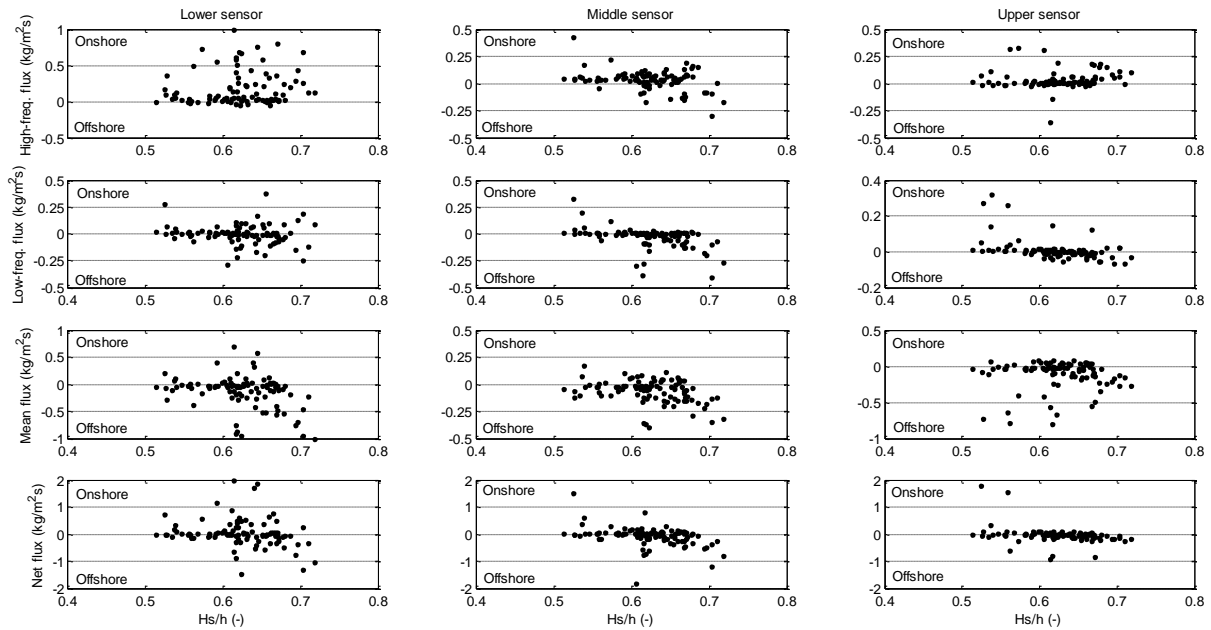
Figure 4.22: Cross-shore suspended sediment fluxes during LWC2 at **a:** lower OBS sensor (5 cmab) and **b:** middle OBS sensor (10 cmab) and **c:** upper OBS sensor (20 cmab) at position P1.
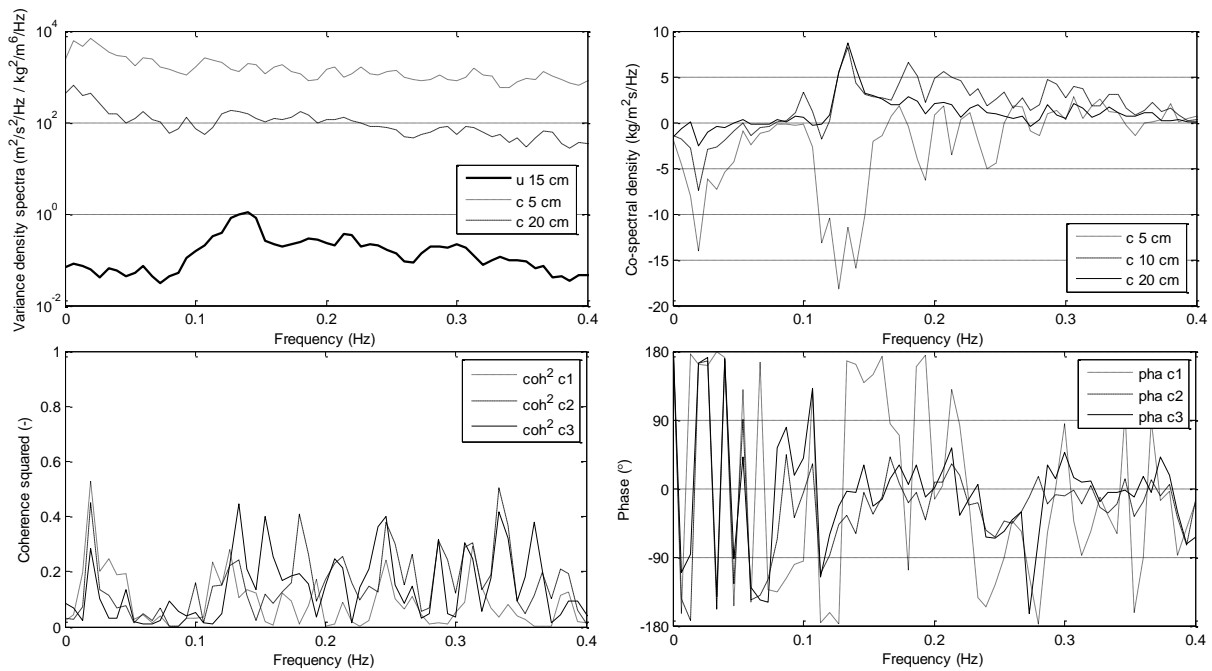

Figure 4.23: a: Variance density spectra, **b:** Co-spectral density, **c:** coherence squared diagram and **d:** phase diagram during LWC2 on 28 October from 04:00h to 04:20h at position P1.

Flux values increased from $Hs/h > 0.35$, again during situations when P2 experienced surf zone conditions. The high-frequency flux at the lower and upper sensor is onshore directed, but the middle sensor shows offshore directed flux again due to phase lag effects. This indicates that phase lag effects can be observed at different heights above the bed, i.e. at the lower OBS sensor at position P1 and at the middle OBS sensor at P2. The mean flux at all sensor heights is offshore directed which is consistent with the measured mean flow velocity (Figure 4.15b). The oscillatory and mean fluxes result in a net offshore directed sediment transport at all sensor heights, with values of 4.6, 4.4 and 2.5 kg/m²s for the lower, middle and upper sensor, respectively. The high-frequency and mean flux are the main contributors

41

to the gross transport (Appendix B.3). Data from tripod P3 lacked, because it was not submerged during the tranquil weather conditions during LWC2.

Figure 4.24: Relative contribution of high freq., low freq. and mean sediment fluxes to net flux during LWC2 at position P1.

The values of the suspended sediment fluxes at P2 during HWC1 are plotted in Figure 4.25. The oscillatory and mean flux measurements have *Hs/h* values ranging between 0.5 and 0.74, indicating that P2 experienced surf zone conditions. The high-frequency fluxes at all three sensor heights are onshore directed and the low-frequency fluxes are small and directed offshore. The mean flux at all sensor heights are offshore directed, which is consistent with the direction of mean velocity (Figure 4.16a). The net sediment flux is directed offshore and results from a slightly higher mean flux contribution than the high-frequency flux contribution (Figure 4.26). The net suspended sediment flux has values of 1.5, 1.8 and 0.9 kg/m^{2}s for the lower, middle and upper sensor, respectively. The co-spectral density calculated for two tidal cycles on the 4th of October on hourly bases shows a different view on the sediment transport directions (Appendix C4). Especially the first tidal cycle predominantly show onshore directed transport at low-frequency which contradicts the low-frequency flux direction described above. The second tidal cycle, however, does show offshore directed transport at low-frequency. Onshore directed transport is observed at high-frequency wavelength during both tidal cycles. Once more, the accompanying variance density spectra show that during high tide values at c1 are several factors higher than at c3 and during low water levels values at c1 nearly equal c3 indicating an uniform distribution of sediment up to the upper sensor. The *Hs/h* values of the oscillatory and mean flux measurements at position P3 range between 0.44 and 0.63 (Appendix A.4), which indicate that P3 experienced surf zone conditions. The oscillatory and mean fluxes at all sensor heights are onshore directed resulting in a onshore directed net flux with values of 4.6, 4.0 and 1.2 kg/m^{2}s for the lower, middle and upper sensor, respectively. The mean flux and high-frequency flux contribute most to a net onshore directed flux (Appendix B.4). This

time there is no clear relation between the direction of the mean velocity and the direction of the mean flux with respect to Hs/h, i.e. on- and offshore directed velocity were measured (Figure 4.16a). The reason for this is because research has shown that there is another parameter which is more indicative for identifying the hydrodynamic zone, namely the wave length ((Raubenheimer, Guza, & Elgar, 1996) and (Price & Ruessink, 2008)). However, in this report the ratio of Hs/h is used to be able to compare results to prior research ((Osborne & Greenwood, 1992a) and (Ruessink et al., 1998)). The main process that causes onshore directed mean transport at all sensor heights at position P3 is overwash, namely water is flowing over the beach crest during inundation. Furthermore, oscillatory and mean flux magnitudes at position P3 are twice as high as at position P2, indicating a large spatial variability. The co-spectral density calculated for two tidal cycles on the 4th of October on hourly bases also illustrates an onshore directed transport at high-frequency wavelength and onshore directed transport at low-frequency wavelength (Appendix C5) which is in line with the direction of the fluxes described above. Yet again, the accompanying variance density spectra show that during high tide values at c_1 are higher than at c_3 and during low water levels values at c_1 nearly equal c_3 indicating an uniform distribution of sediment up to the upper sensor. The small number of oscillatory, mean and net flux measurements at position P4 were attained during the few hours of beach flat inundation (Figure 4.14a). The Hs/h values range between 0.47 and 0.56 (Appendix A.5), indicating that P4 also experienced surf zone conditions. The magnitude of the oscillatory fluxes at all three sensor heights is negligibly small. The mean fluxes are onshore directed, which is consistent with the direction of the measured mean flow velocity (Figure 4.16a). This onshore directed mean flux can be related to overwash. The mean flux at P4 is several factors smaller than at positions P2 and P3, but is still the main contributor to the net flux (Appendix B.5). The oscillatory and mean fluxes result in a net onshore directed sediment transport at all sensor heights, with values of 0.6, 0.7 and 0.6 kg/m^{2}s for the lower, middle and upper sensor, respectively, showing little vertical variation. The co-spectral density calculated for the first tidal cycle on the 4th of October illustrates an onshore directed transport at high-frequency wavelength and also an onshore directed transport at low-frequency wavelength (Appendix C6) which is in line with the flux directions described above. Again during high tide there is little difference between the estimates of the concentration at the lower and upper sensor, but during falling tide this difference increases.

The values of the suspended sediment fluxes at P2 during HWC2 are plotted in Figure 4.27. The oscillatory and mean flux measurements have Hs/h values ranging between 0.52 and 0.72, indicating that P2 experienced fully broken wave conditions. There is little difference between the oscillatory, mean and net fluxes of position P2 during HWC1 and HWC2. Only the low-frequency and mean flux have higher magnitudes. The mean flux contribution to the net flux is slightly higher than the high-frequency flux contribution in both lower and upper sensor (Figure 4.28). The oscillatory and mean fluxes result in a net offshore directed sediment transport at all sensor heights, with values of 5.0, 3.5 and 0.7 kg/m^{2}s for the lower, middle and upper sensor, respectively.

Figure 4.25: Cross-shore suspended sediment fluxes during HWC1 at **a:** lower OBS sensor (5 cmab) and **b:** middle OBS sensor (10 cmab) and **c:** upper OBS sensor (20 cmab) at position P2.
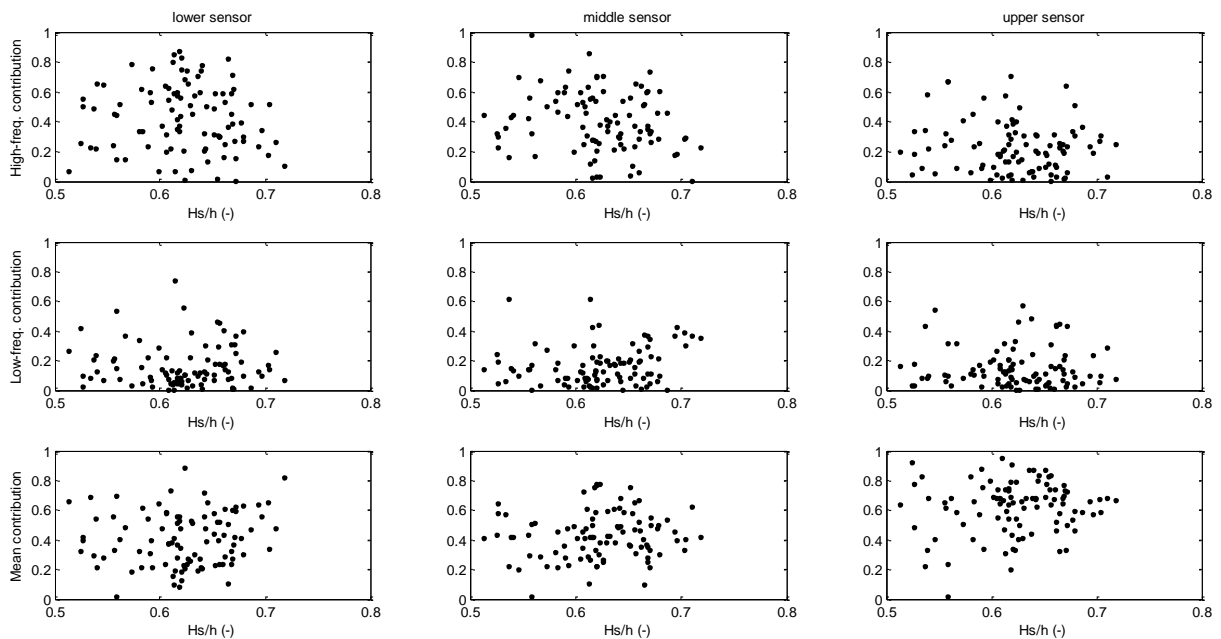
Figure 4.26: Relative contribution of high freq., low freq. and mean sediment fluxes to net flux during HWC1 at position P2.

The *Hs/h* values of the oscillatory and mean flux measurements at position P3 range between 0.38 and 0.62 (Appendix A.6), which indicate that P3 experienced surf zone conditions. The suspended sediment fluxes at P3 during HWC2 differ greatly from the fluxes at P3 during HWC1. The high-frequency flux at the middle and upper sensor is onshore directed, but the lower sensor shows offshore directed flux again due to phase lag effects. The offshore directed mean flux is consistent with the direction of the mean velocity (Figure 4.16b) and is the main contributor to the net flux (Appendix B.6). The oscillatory and mean fluxes result in a net offshore directed flux at all sensor heights, with values of 1.2, 0.25 and

0.25 kg/m²s for the lower, middle and upper sensor, respectively. There are no flux data for tripod P4, because the beach plain did not inundate during HWC2.
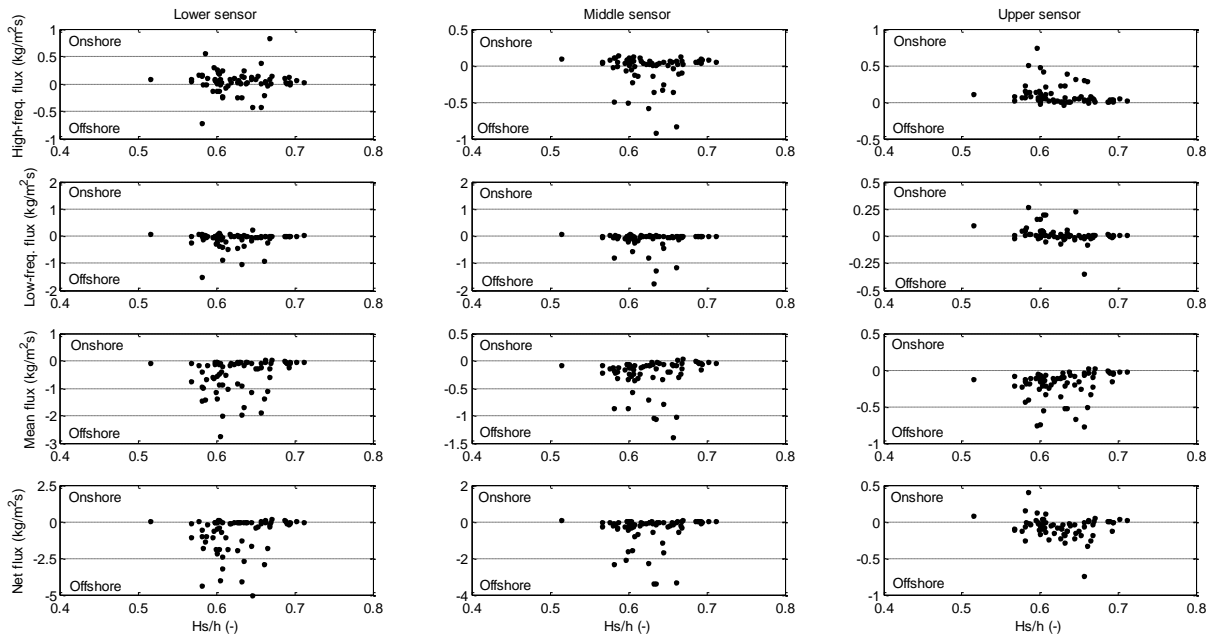
Figure 4.27: Cross-shore suspended sediment fluxes during HWC2 at **a:** lower OBS sensor (5 cmab) and **b:** middle OBS sensor (10 cmab) and **c:** upper OBS sensor (20 cmab) at position P2.
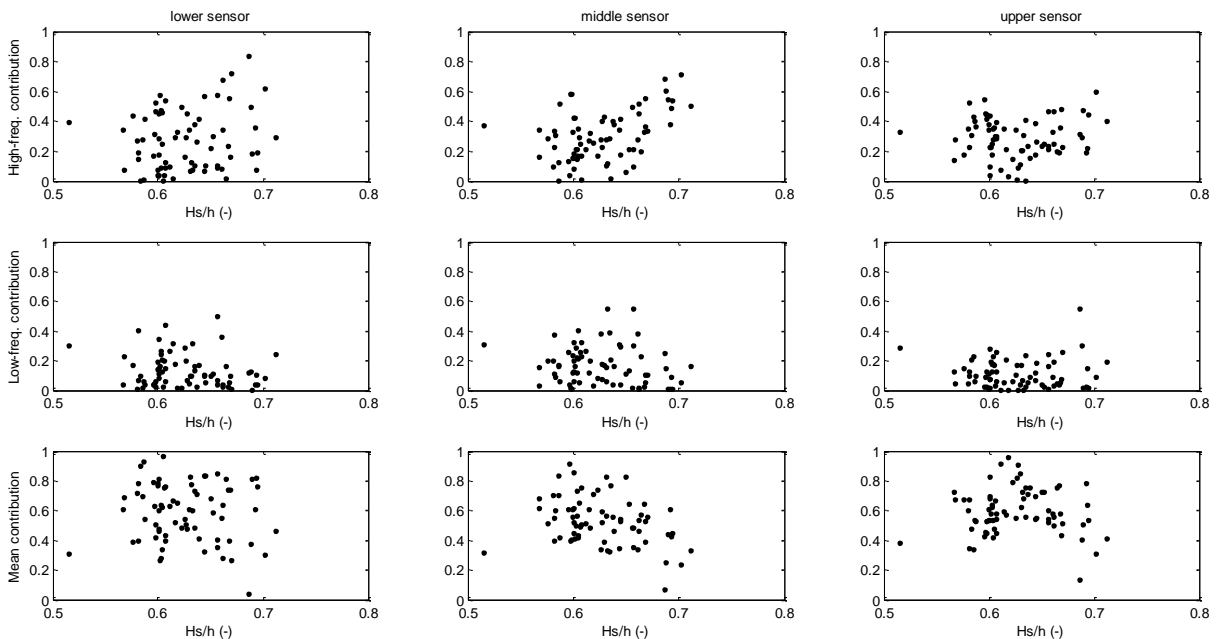
Figure 4.28: Relative contribution of high freq., low freq. and mean sediment fluxes to net flux during HWC2 at position P2.

The main cross-shore suspended sediment transport mechanisms during low and high wave conditions are summarized below. Although the observed Hs/h dependence of the fluxes is uncertain, it can be concluded that surf zone conditions prevailed at all tripod positions during low and high wave conditions. The breaking waves had generated undertow and therefore offshore directed transport at tripod positions P1 and P2 at all sensor heights during both periods of low wave conditions and at tripod P2 during HWC1 and at tripods P2

and P3 during HWC2. Onshore directed transport occurred at tripod P3 during LWC1 due to cell circulation and at tripod P3 and P4 during HWC1 due to overwash processes. The difference between both low wave conditions is that the net suspended sediment transport during LWC2 is several factors higher than during LWC1. The cross-shore suspended sediment transport mechanism during LWC2 result in erosion of the seaward side of the intertidal beach plain (Figure 4.6 and Figure 4.7). During LWC1 water levels overtopped the crest of the swash bar at tripod P3 causing it to inundate and water to flow out via the runnel towards the main channel of The Slufter creating a pattern of cell circulation. In both low wave conditions the transport mechanisms resulted in an onshore migration of a swash bar at the upper part of the intertidal beach plain (see sections 4.2.1 and 4.2.4). The difference between both high wave conditions is that the beach plain during HWC1 was inundated due to higher set-up levels compared to HWC2 (Figure 4.14). The beach crest inundation resulted in overwash processes and onshore directed net suspended sediment transport at tripod positions P3 and P4. Overwash processes reworked the entire cross-shore profile (Figure 4.4), eroding sediment on the seaward side of the beach plain and depositing sediment on the landward side of the beach plain. During HWC2 waves reached high enough to rework the seaward part of the beach plain (Figure 4.5). Little morphological change was observed at tripod position P2 even though values of net sediment transport were several factors higher compared to P2 during HWC1. Overall the mean flux contribution to the net flux is generally largest. The low-frequency flux contribution to the net flux during high wave conditions were generally larger compared to the little to no low-frequency flux contribution at low wave conditions.

5 Discussion

The fundamental nature of the sediment transport processes discussed in this study is that sediment is being stirred by turbulence generated near the sea floor. In an article by (Scott, Hsu, & Cox, 2009) it is suggested that this picture is somewhat more complex. Underneath breaking waves, turbulence generated by the breaking waves (also known as bore-generated turbulence) can also reach the sea floor and as a result stirs up sediment. The breaking wave turbulence often has no constant relation with the wave motion. This can lead to intermittent high suspended sediment concentrations under wave crest at one moment in time and under a wave trough in another moment in time. This has major consequences for the interpretation of suspended sediment transport. First of all, high-frequency suspended sediment transport under wave crest meant onshore directed transport, and if high-frequency transport was directed offshore it was thought this was caused due to vortex development on a steep rippled bed (Van Rijn, 1993). But if the high suspended sediment concentration is located underneath a wave trough it is transported offshore. When high suspended sediment concentration events occur at irregular intervals there is no constant relation between high-frequency suspended sediment and direction of transport. Furthermore, this would indicate that the high-frequency transport in one moment in time will amplify the current related suspended sediment transport (both fluxes in same direction) and in another moment in time will reduce the current related cross-shore transport (fluxes in opposing direction). Because these insights are relatively new they have not been implemented in this research, but in future research it is advised to take them into account.

Suspended sediment measurements require data calibration to convert field data measured in millivolt to a physical meaningful parameter, namely g/L or kg/m^3. A linear line was fitted through the data to obtain calibration curves for the conversion. Normally a second order polynomial is fitted through the data. This however gave poor results because the second order polynomial curves bended back downward (became negatively parabolic), which resulted in two possible outcomes in concentration in mV. This would mean that there are also two possible answers in concentration g/L, which is an unwanted situation. Therefore, it was chosen to use a linear fit on the data. The best linear fit (R^2 = 0.99) was achieved when fitted to concentration data up to 10 g/L ($\approx$ 300 mV).

All findings of the cross-shore suspended sediment transport need to be considered with care due to several unavoidable problems in the field and due to the used measuring methods. The first problem is that the tripods slowly sink into the sediment due to the swash of the rising tide that creates scour along the lead weights of the tripod. The scour becomes minimal when the weights are burrowed. As a consequence the exact heights of the sensors above the bed were unknown. The sensor height above the bed was measured once daily at low tide and was interpolated between these moments in time. Therefore, the observed general *Hs/h* dependence of the fluxes can only be regarded as tentative. Another problem is that the relative contributions of the oscillatory and current related flows are not

necessarily representative for the depth-averaged fluxes. In addition, flux profile estimates based on single current measurement can differ from flux profiles from paired instruments by as much as an order of magnitude and even the predicted direction can be incorrect (Ogston & Sternberg, 1995). To minimize this inaccuracy a simple engineering rule from (Van Rijn, 1991) is used to calculate the mean velocity at the location of the lower, middle and upper OBS sensor heights instead of using the actual measured EMCM velocity.

Suspended sediment transport processes are different between low- and high wave conditions due to a different hydrodynamic and morphodynamic setting (beach backed by dunes vs. beach backed by an inundated dune valley). Mean cross-shore currents during low wave conditions are often offshore directed at tripod positions P1 and P2 due to the presence of undertow. However, when waves stop breaking the undertow diminishes (LWC2 on the 29th of October). During LWC1 water levels were high enough to inundate tripod P3 measuring an onshore directed mean current due to the presence of horizontal cell circulation. There is a clear difference between the two high wave events with respect to the directional pattern of the mean cross-shore currents. During HWC1 mean cross-shore currents fluctuate in on- and offshore direction at positions P2 and P3. During this storm event the beach plain crest became inundated measuring a flow velocity of 1 m/s in onshore direction, which is 10 times larger than during low wave conditions. However, during HWC2 mean cross-shore currents were directed offshore with similar values for P2 and P3 as measured during HWC1.

The net transport which was determined by the relative importance of the oscillatory and mean components of the incident wave motions reveals offshore directed transport at tripod positions P1 and P2 at all sensor heights during both periods of low wave conditions and at tripod P2 during HWC1 and at tripods P2 and P3 during HWC2. Onshore directed transport occurred at tripod P3 during LWC1 due to cell circulation and at tripod P3 and P4 during HWC1 due to overwash processes. Overall the mean flux contribution to the net flux is generally largest. The low-frequency flux contribution to the net flux during high wave conditions were generally larger compared to the little to no low-frequency flux contribution at low wave conditions.

The cross-shore suspended sediment transport mechanisms during both low wave conditions resulted in an onshore migration of a swash bar at the upper part of the intertidal beach plain. The cross-shore suspended sediment transport mechanisms during the first high wave condition resulted in large scale onshore sediment transport. This was caused by overwash processes that were generated when the beach plain crest became inundated, e.g. sediment was eroded on the seaward side of the beach plain crest and deposited on the landward side. Furthermore, the swash bar and runnel disappeared flattening the entire beach plain profile. The cross-shore suspended sediment transport mechanisms during the second high wave event resulted in erosion of the high water areas on the seaward side of the beach plain crest.

The Slufter with its lower lying dune valley is a unique system compared to a beach backed by dunes. The hydrodynamic processes during low wave conditions strongly

resemble the processes that occur on a beach backed by dunes, i.e. undertow. However, during storm events, where high wave conditions and large storm surge levels coincide, the beach plain becomes entirely inundated resulting in overwash processes. Overwash processes dominate the suspended sediment transport on the higher parts of the beach plain at tripod positions P3 and P4 and generally cause a flattening of the beach plain morphology. While swash bars are generated and migrating onshore during low wave conditions at the intertidal part of the beach plain, which is a common phenomenon at barred beaches (Osborne & Greenwood, 1992a).

6 Conclusions

- *How does the magnitude and direction of mean currents, oscillatory flows and infragravity motion vary as a function of cross-shore position and as a function of offshore forcing?*

  The lower part of the intertidal zone is dominated by offshore mean currents (undertow) during both low- and high wave conditions. During low wave conditions the upper part of the intertidal zone is subject to onshore transport due to horizontal cell circulation. When high wave conditions cause beach crest inundation, onshore transport is dominated at the upper part of the intertidal zone and at the beach plain crest due to overwash processes with mean current velocities 10 times larger than during low-wave conditions.

- *What is the relative contribution of these flow mechanisms to the net suspended sediment transport and how does the relative contribution depend on cross-shore position and offshore forcing?*

  The mean flux contribution (= current related/undertow) to the net flux is generally largest followed closely by the high-frequency flux contribution. The low-frequency flux contribution (= infragravity wave related) to the net flux is significantly smaller, but is slightly larger during high wave conditions compared to low wave conditions.

- *What are the qualitative and quantitative differences between normal beach conditions and overwash processes during a flooding event?*

  Sediment that is eroded on the beach can be transported to the backbarrier during a flooding event which is not the case during normal beach conditions.

- *How does the morphology of the beach plain change during low- and high- energy conditions?*

  Swash bars are generated and migrating onshore during low wave conditions and the entire morphology of the beach plain flattens during high wave conditions.

Main research question:

- *Which hydrodynamic processes dominate the cross-shore suspended sediment transport leading to the observed morphological change of the beach plain of The Slufter during storm conditions?*

  Overwash processes dominate the cross-shore suspended sediment transport leading to the observed morphological change of the beach plain of The Slufter during storm conditions.

The hypothesis that infragravity waves are the dominant cross-shore sediment transport mechanism that results in the observed morphological change during high wave conditions is therefore rejected.

Recommendations

The data analyses of this study are concentrated on two extreme weather conditions, namely two time frames of low- and high wave conditions. Hereby neglecting intermediate wave conditions which prevailed during the fieldwork period. To complete the insights into the hydro- and morphodynamics of The Slufter system it is advised to continue data analysis via a desk study. Thanks to a successfully completed fieldwork period there is a lot of data to work with.

References

Aagaard, T. & B. Greenwood. (1995), Suspended sediment transport and morphological response on a dissipative beach. Continental Shelf Research 15(9), pp.1061-1086.

Beach, R.A. & R.W. Sternberg. (1991), Infragravity driven suspended sediment transport in the swash, inner and outer surf zone. Proc. Coastal Sediments '91. ASCE, pp.144-128.

Beach, R.A. & R.W. Sternberg. (1988), Suspended sediment transport in the surf zone: Response to cross-shore infragravity motion. Marine Geology 80(1-2), pp.61-79.

Cayocca, F. (2001), Long-term morphological modeling of a tidal inlet: The arcachon basin, france. Coastal Engineering 42(2), pp.115-142.

Conley, D.C. & R.A. Beach. (2003), Cross-shore sediment transport partitioning in the nearshore during a storm event. Journal of Geophysical Research C: Oceans 108(3), pp.10-1.

Donnelly, C., N. Kraus & M. Larson. (2006), State of knowledge on measurement and modeling of coastal overwash. Journal of Coastal Research 22(4), pp.965-991.

Downing, J.P., R.W. Sternberg & C.R.B. Lister. (1981), New instrumentation for the investigation of sediment suspension processes in the shallow marine environment. Marine Geology 42(1-4), pp.19-34.

Durieux, M. (2003), De stabiliteit van de slufter op texel. MSc Thesis Civil Engineering, Delft University, pp.91.

Foote, Y., P. Russell, D. Huntley et al. (1998), Energetics prediction of frequency-dependent suspended sand transport rates on a macrotidal beach. Earth Surface Processes and Landforms 23(10), pp.927-941.

Greenwood, B. & P.B. Hale. (1980), Depth of activity, sediment flux, and morphological change in a barred nearshore environment. in The Coastline of Canada, S.B. McCann, editor; Geological Survey of Canada Paper 80-10, pp.89-109.

Hanes, D.M. & D.A. Huntley. (1986), Continuous measurements of suspended sand concentration in a wave dominated nearshore environment. Continental Shelf Research 6(4), pp.585-596.

Huntley, D.A. & D.M. Hanes. (1987). Direct measurement of suspended sediment transport. Paper presented at the , 1 pp.723-737. Retrieved 8 July 2009.

Masselink, G. & M.G. Hughes, eds. (2003), An introduction to coastal processes and geomorphology. London: Hodder Arnold.

Masselink, G. & C. Pattiaratchi. (2000), Tidal asymmetry in sediment resuspension on a macrotidal beach in northwestern australia. Marine Geology 163(1-4), pp.257-274.

Nielsen, P. (1979), Some basic concepts of wave sediment transport. Technical University of Denmark, Lyngby, Institute of Hydrodynamics and Hydraulic Engineering Series Paper 20

Ogston, A.S. & R.W. Sternberg. (1995), On the importance of nearbed sediment flux measurements for estimating sediment transport in the surf zone. Continental Shelf Research 15(13), pp.1515-1524.

Osborne, P.D. & B. Greenwood. (1992a), Frequency dependent cross-shore suspended sediment transport. 1. A non-barred shoreface. Marine Geology 106(1-2), pp.1-24.

Osborne, P.D. & B. Greenwood. (1992b), Frequency dependent cross-shore suspended sediment transport. 2. A barred shoreface. Marine Geology 106(1-2), pp.25-51.

Price, T.D. & B.G. Ruessink. (2008), Morphodynamic zone variability on a microtidal barred beach. Marine Geology 251(1-2), pp.98-109.

Puijvelde, S.v. (2009), Morphodynamics of de slufter - morphodynamical processes in a small tidal inlet in the netherlands. MSc. Thesis Physical Geography, Utrecht University, pp.pp. 92.

Raubenheimer, B., R.T. Guza & S. Elgar. (1996), Wave transformation across the inner surf zone. Journal of Geophysical Research C: Oceans 101(C11), pp.25589-25597.

Ruessink, B.G., K.T. Houwman & P. Hoekstra. (1998), The systemic contribution of transporting mechanisms to the cross-shore sediment transport in water depths of 3 to 9 m. Marine Geology 152(4), pp.295-324.

Russell, P.E. (1993), Mechanisms for beach erosion during storms. Continental Shelf Research 13(11), pp.1243-1265.

Scott, N.V., T.-. Hsu & D. Cox. (2009), Steep wave, turbulence, and sediment concentration statistics beneath a breaking wave field and their implications for sediment transport. Continental Shelf Research 29(20), pp.2303-2317.

Van Rijn, L.C. (1991), Database sand concentrations and sand transport in current and/or waves. report H1148-04/05, delft hydraulics, netherlands.

Van Rijn, L. C. (1993). Principles of sediment transport in rivers, estuaries and coastal seas. Amsterdam: Aqua Publications.

Appendices

A.   Cross-shore suspended sediment fluxes

A.1   Cross-shore suspended sediment fluxes during LWC1 at position P2

a: lower OBS sensor   **b:** upper OBS sensor
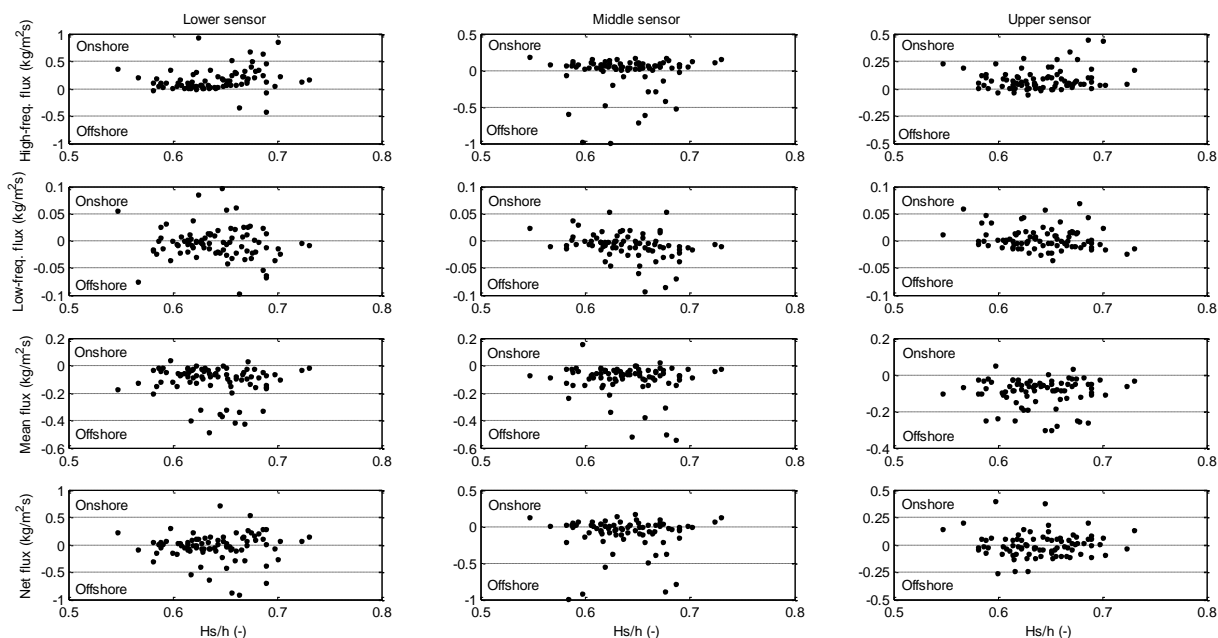
A.2   Cross-shore suspended sediment fluxes during LWC1 at position P3

a: lower OBS sensor   **b:** upper OBS sensor
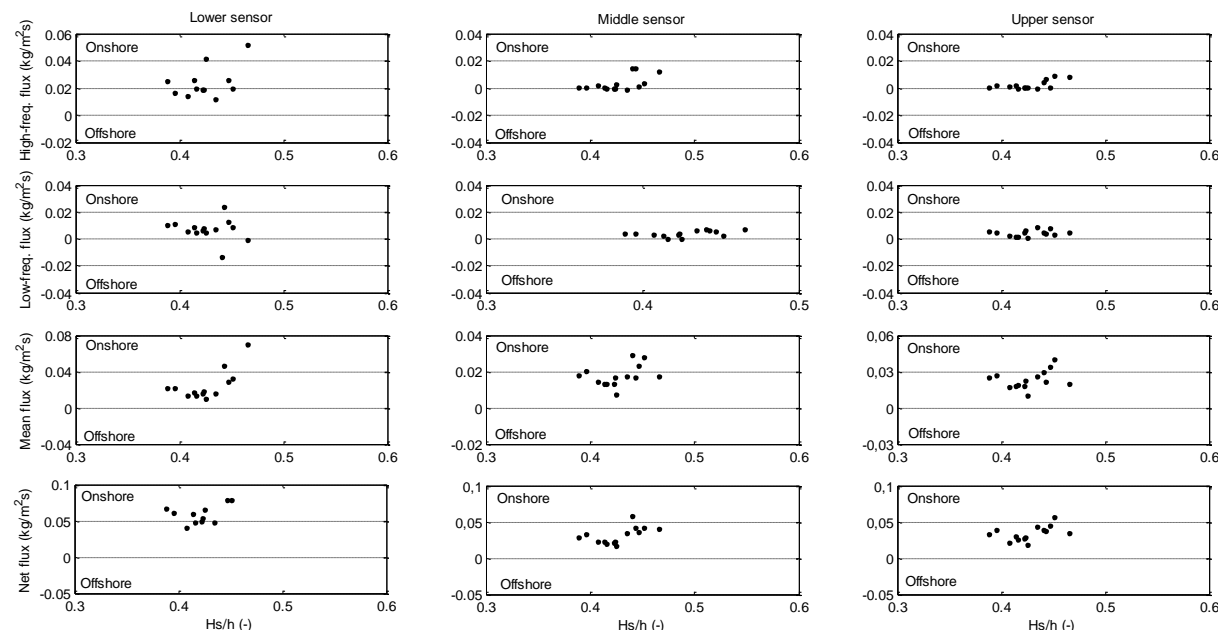
A.3   Cross-shore suspended sediment fluxes during LWC2 at position P2

a: lower OBS sensor   **b:** upper OBS sensor
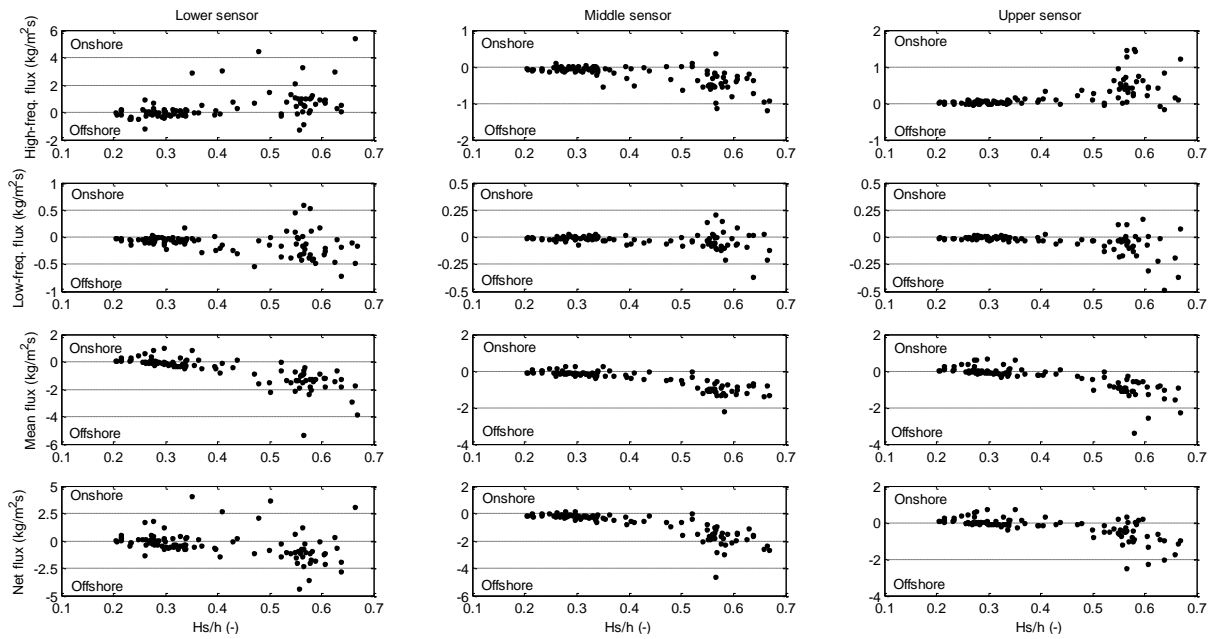
A.4   Cross-shore suspended sediment fluxes during HWC1 at position P3

a: lower OBS sensor   **b:** upper OBS sensor
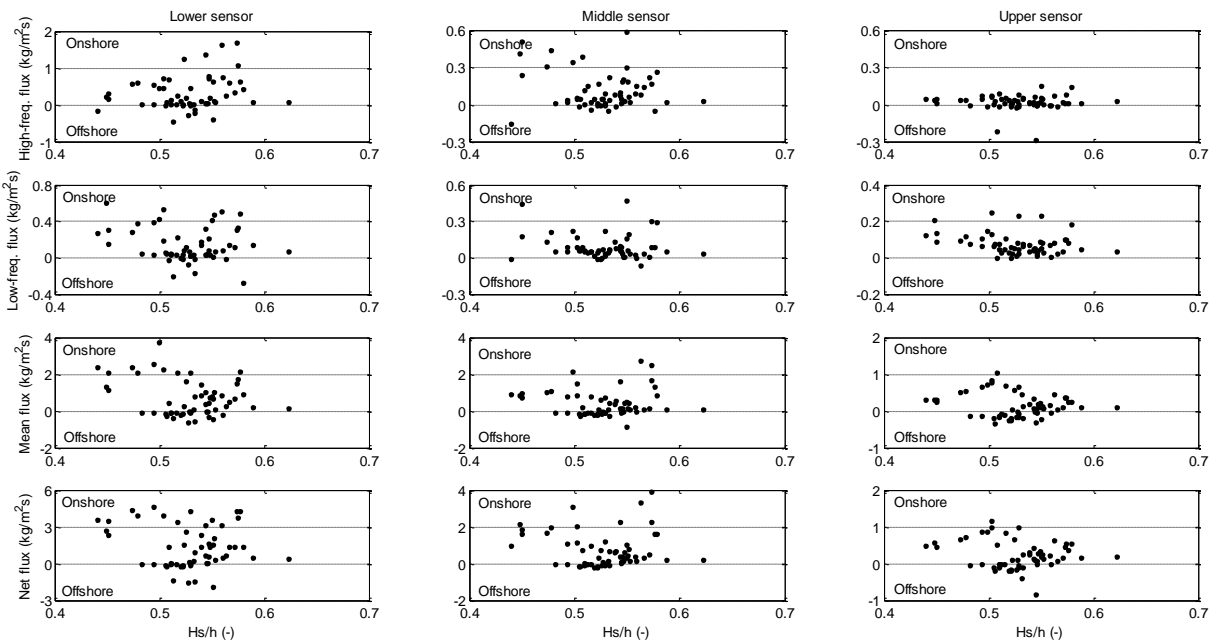
A.5   Cross-shore suspended sediment fluxes during HWC1 at position P4

     a: lower OBS sensor   **b:** upper OBS sensor
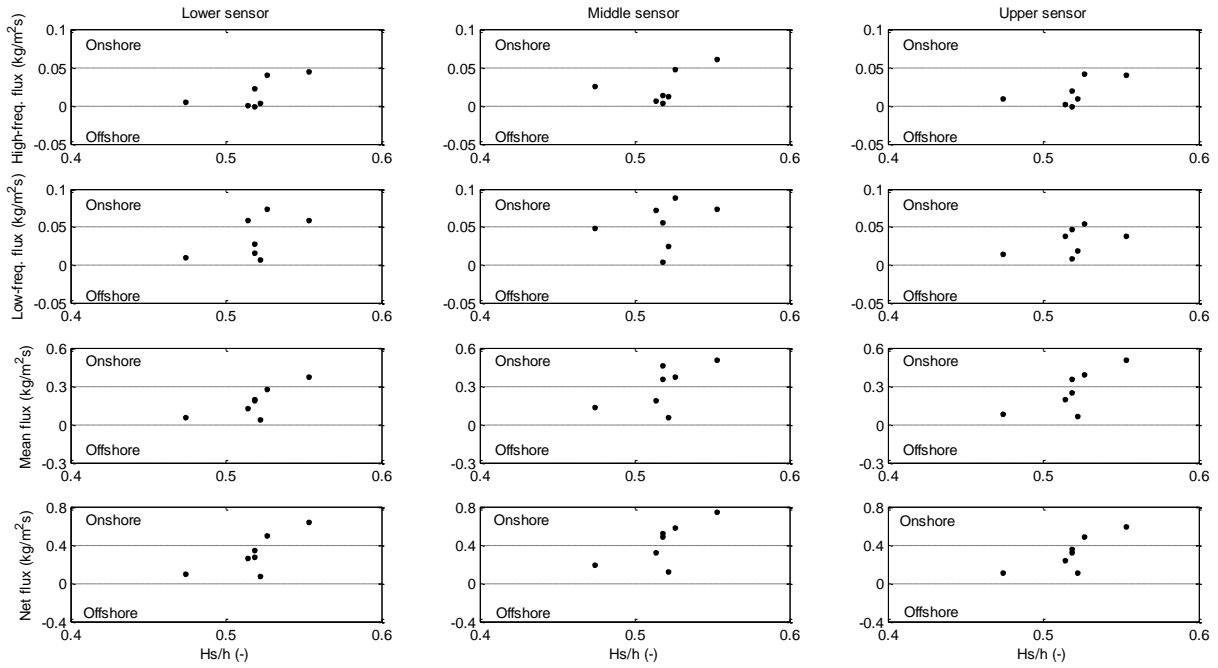
A.6   Cross-shore suspended sediment fluxes during HWC2 at position P3

     a: lower OBS sensor   **b:** upper OBS sensor
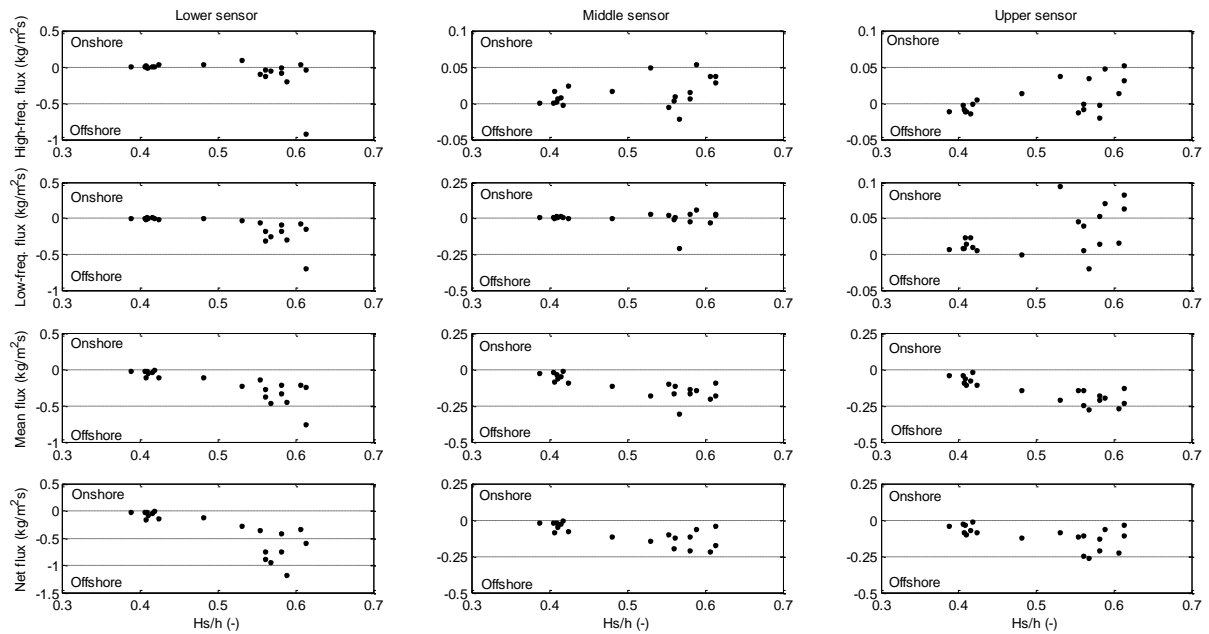
B. Relative contribution of high freq., low freq. and mean sediment fluxes to net flux

B.1 Relative contribution of high freq., low freq. and mean sediment fluxes to net flux during LWC1 at position P2

a: lower OBS sensor **b:** upper OBS sensor
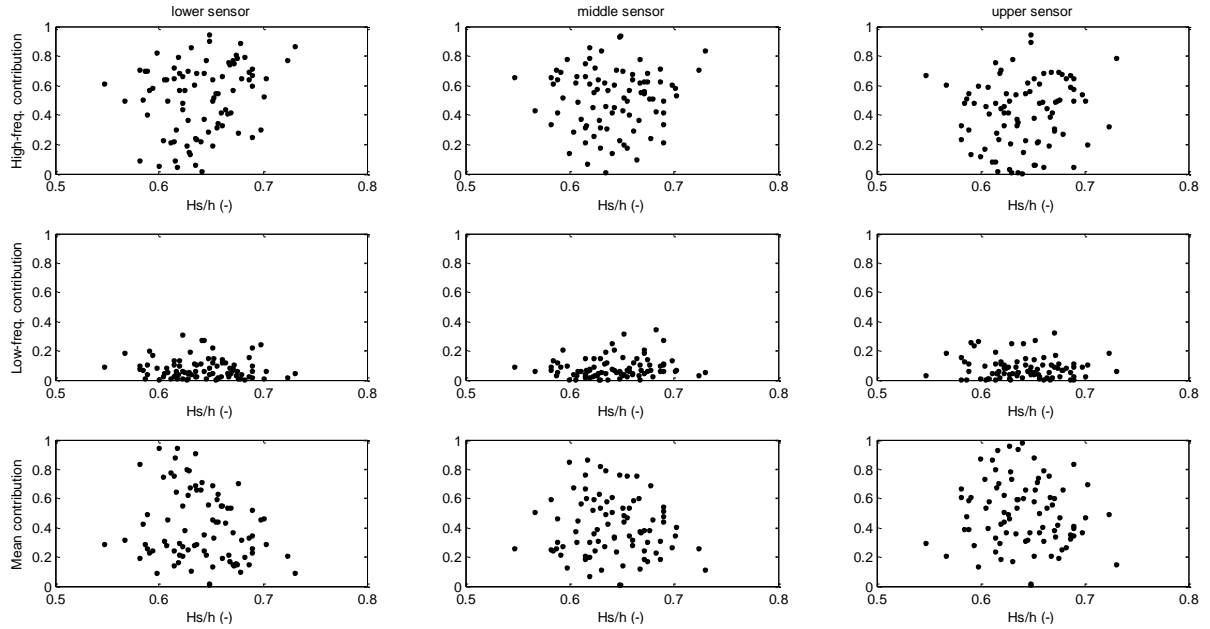
B.2 Relative contribution of high freq., low freq. and mean sediment fluxes to net flux during LWC1 at position P3

a: lower OBS sensor   **b:** upper OBS sensor
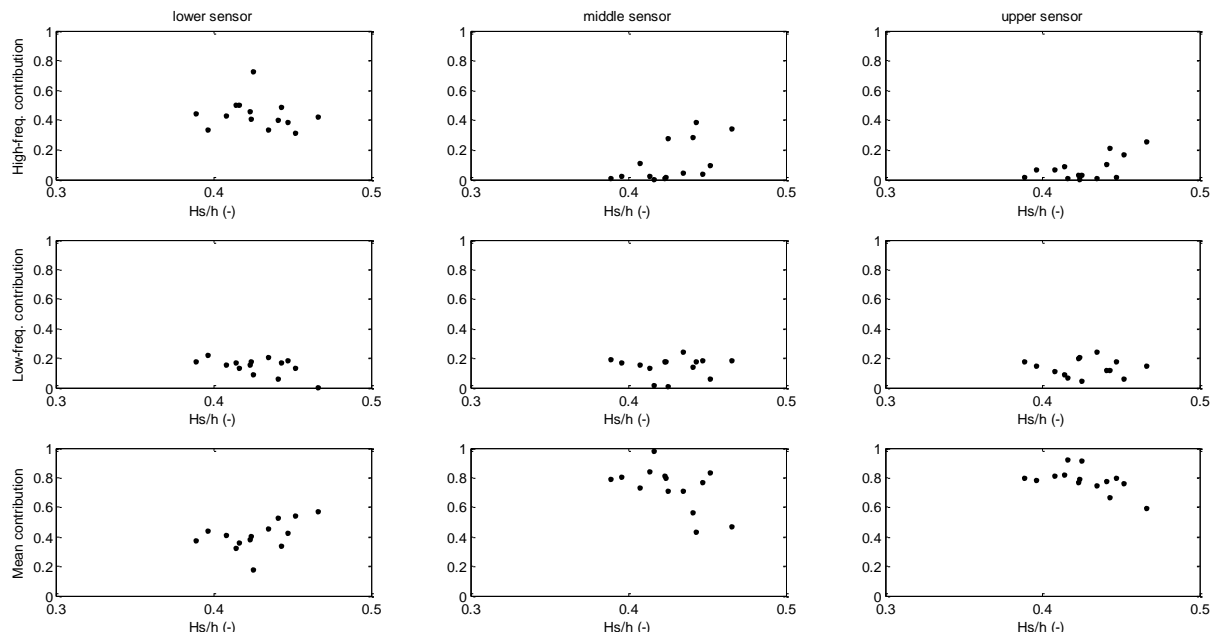
B.3 Relative contribution of high freq., low freq. and mean sediment fluxes to net flux during LWC2 at position P2

a: lower OBS sensor   **b:** upper OBS sensor
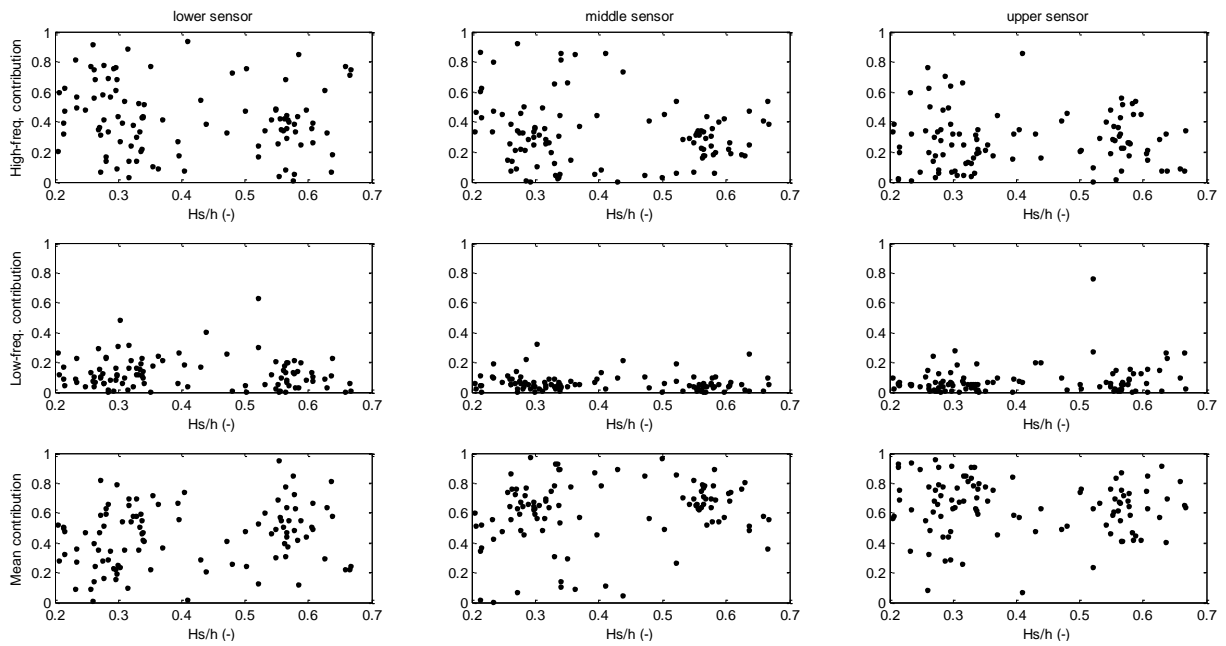
B.4   Relative contribution of high freq., low freq. and mean sediment fluxes to net flux during HWC1 at position P3

a: lower OBS sensor   **b:** upper OBS sensor
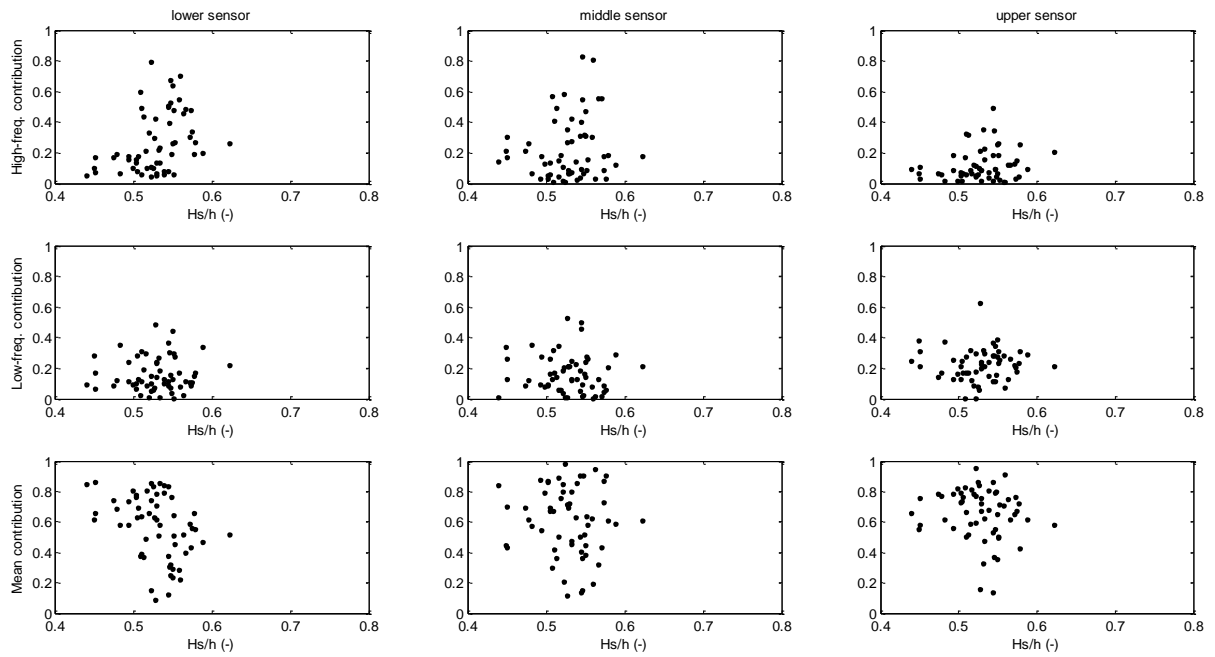
B.5 Relative contribution of high freq., low freq. and mean sediment fluxes to net flux during HWC1 at position P4

a: lower OBS sensor **b:** upper OBS sensor
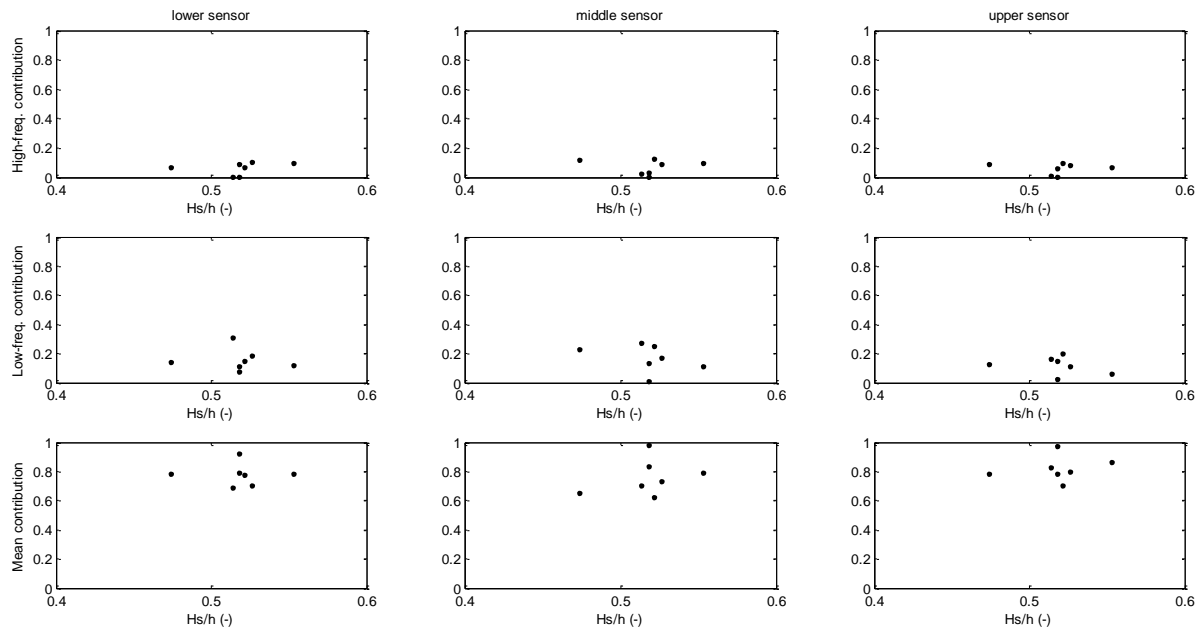
B.6   Relative contribution of high freq., low freq. and mean sediment fluxes to net flux during HWC2 at position P3

a: lower OBS sensor   **b:** upper OBS sensor
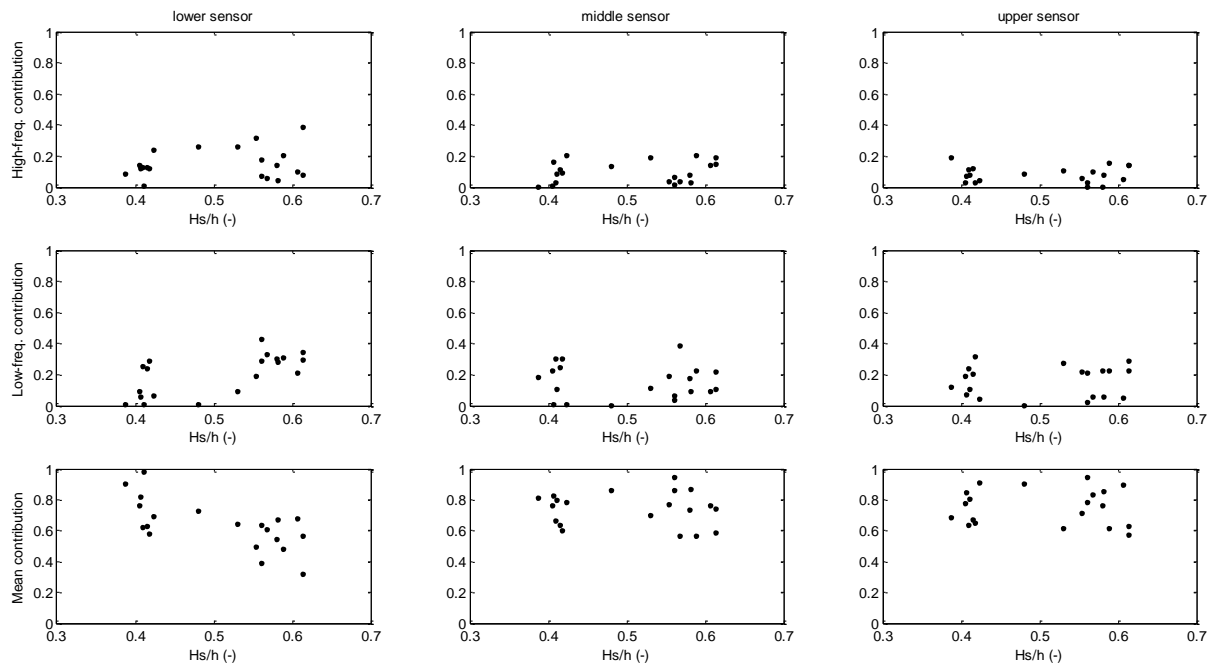
C.1. Hourly Variance Density Spectrum and Co-spectral density during LWC1 at P1

C.1.1   26 Sept 22:00 – 23:00
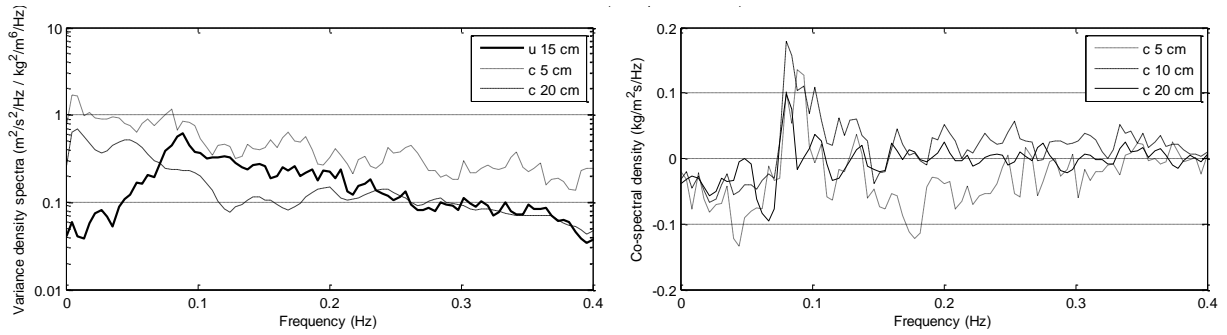
C.1.2   26 Sept 23:00 – 24:00
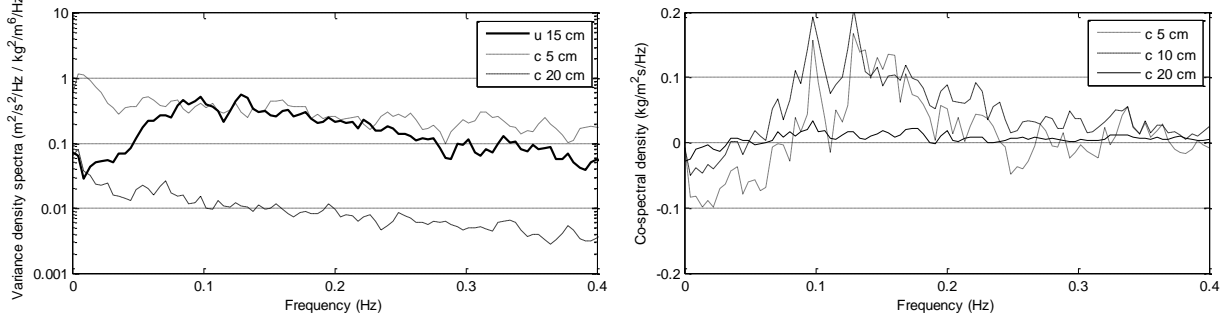
C.1.3   27 Sept 00:00 – 01:00
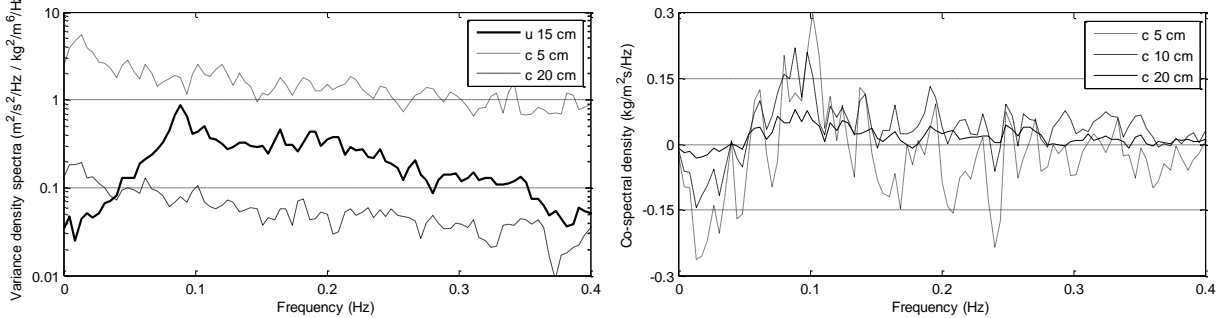
C.1.4   27 Sept 01:00 – 02:00
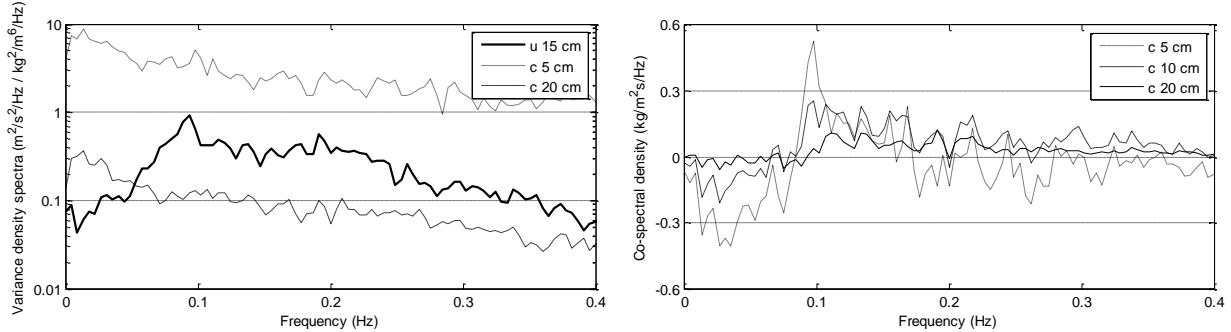
C.1.5   **27 Sept 02:00 – 03:00**
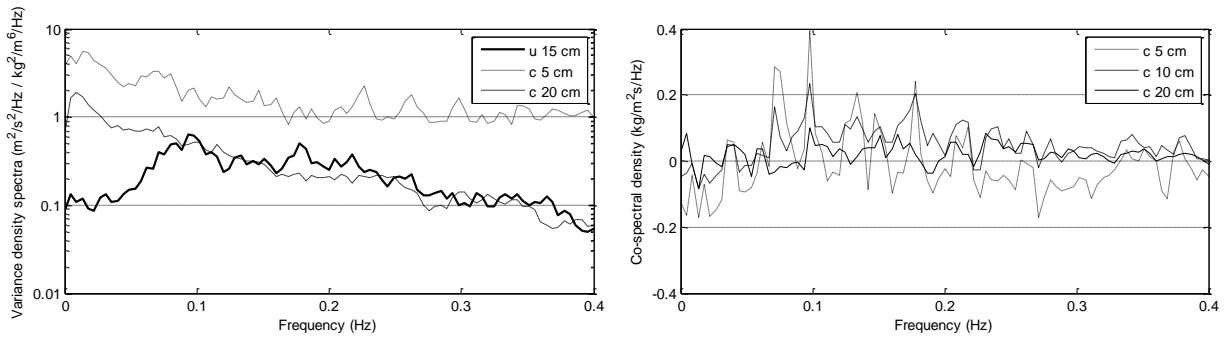
C.1.6   **27 Sept 03:00 – 04:00**
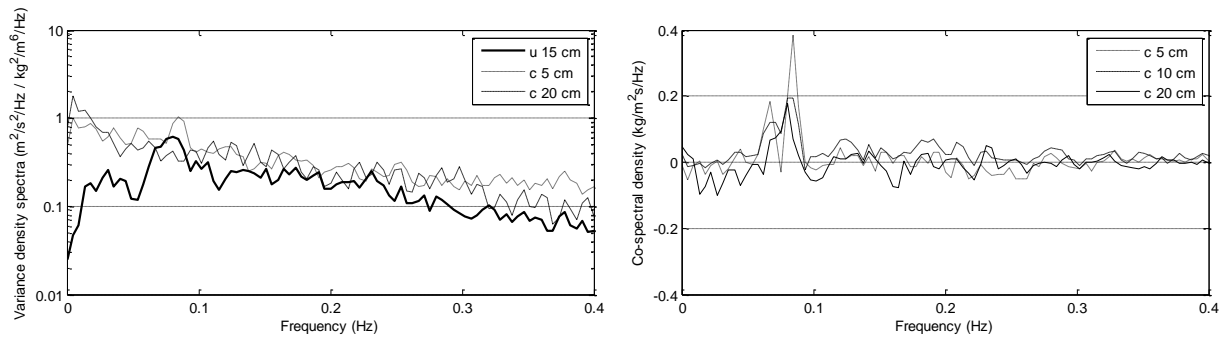
C.1.7   **27 Sept 10:00 – 11:00**
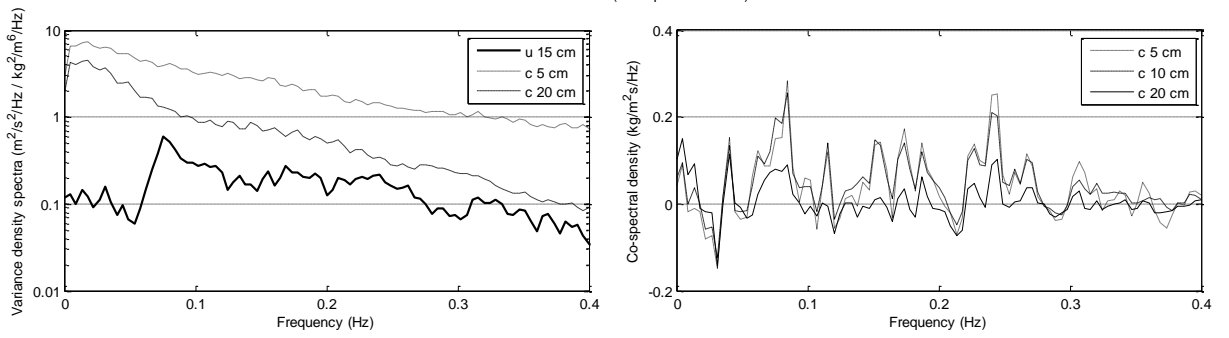
C.1.8   **27 Sept 11:00 – 12:00**
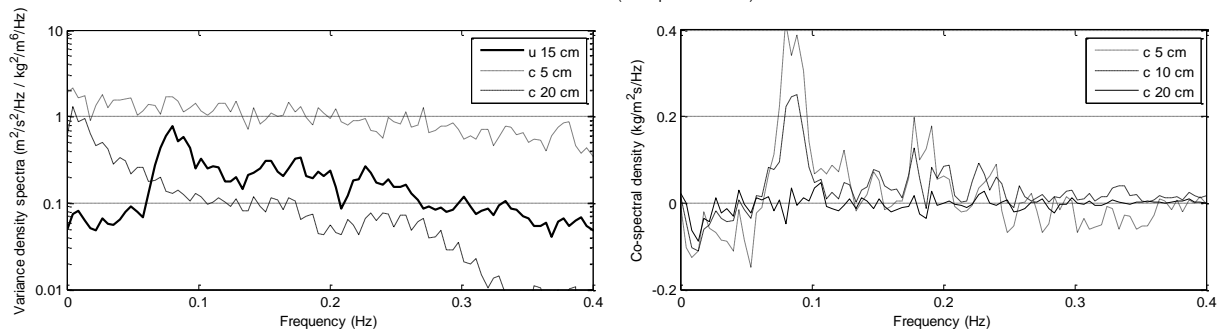
C.1.9   **27 Sept 12:00 – 13:00**
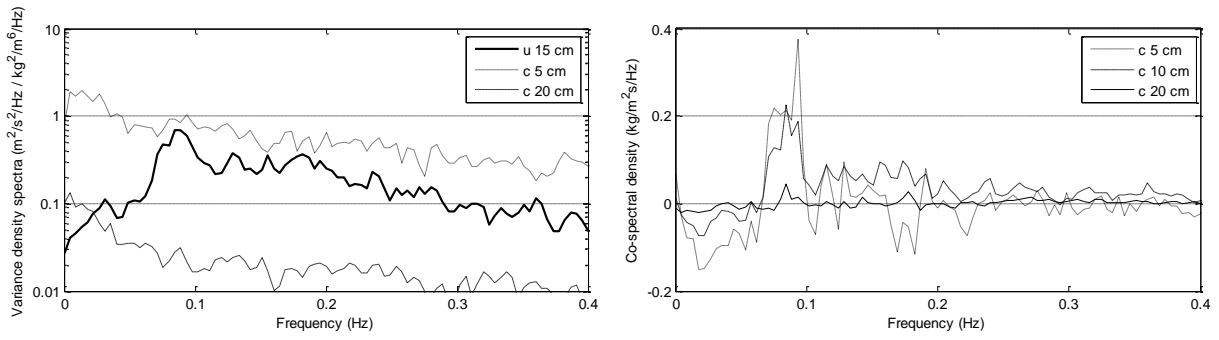
C.1.10   **27 Sept 13:00 – 14:00**
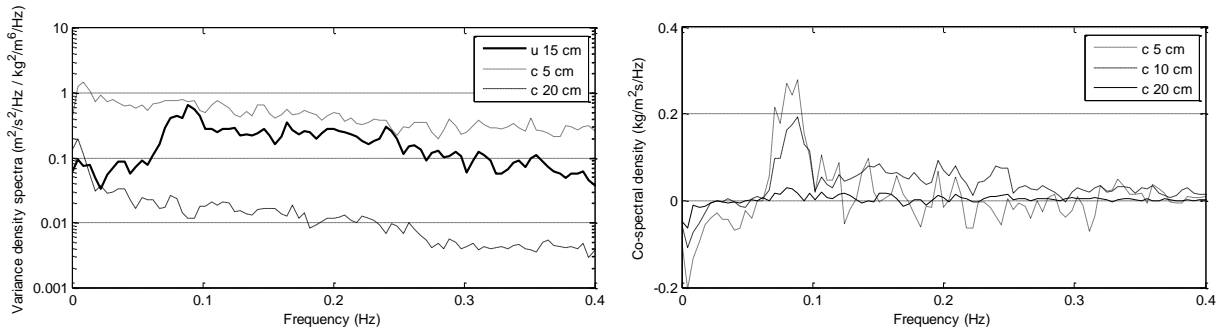
C.1.11   **27 Sept 14:00 – 15:00**
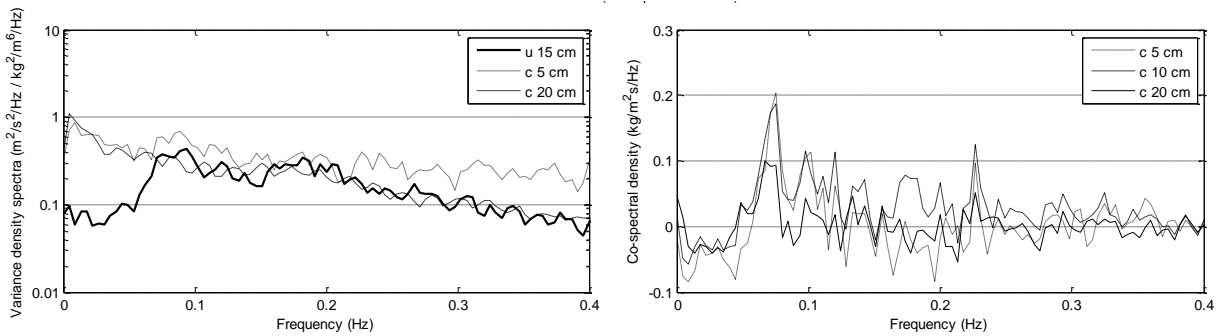
C.1.12   **27 Sept 15:00 – 16:00**
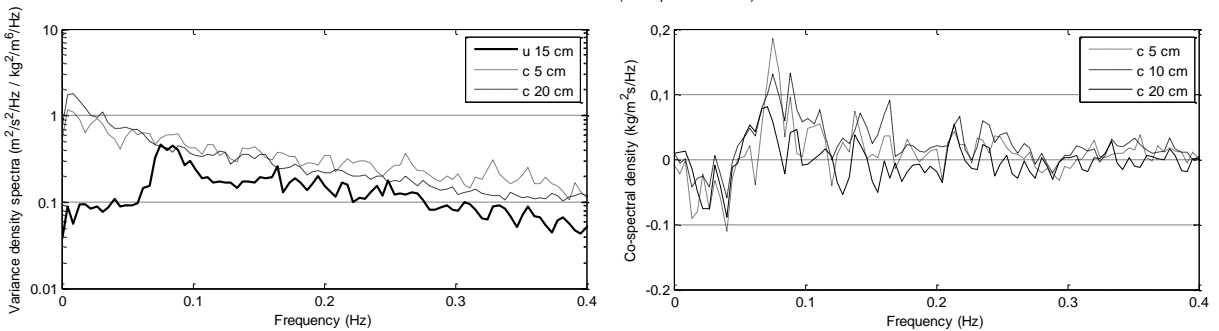
C.2 Hourly Variance Density Spectrum and Co-spectral density during LWC1 at P2

C.2.1   26 Sept 22:00 – 23:00
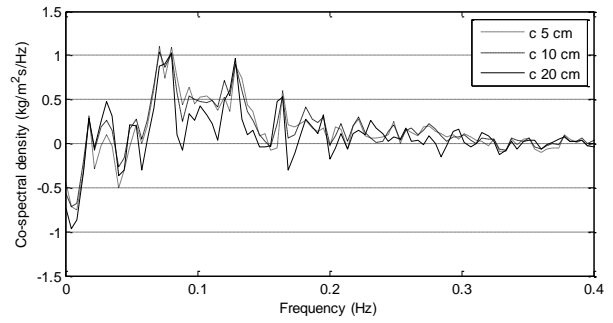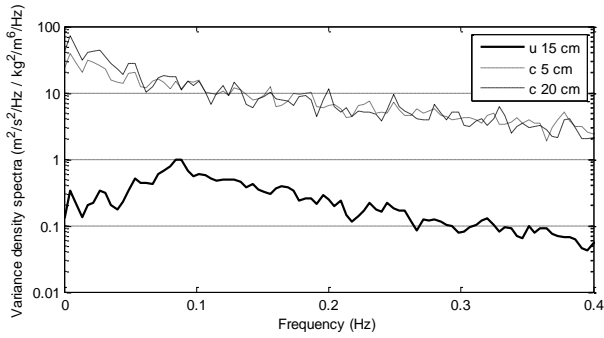

C.2.2   26 Sept 23:00 – 24:00
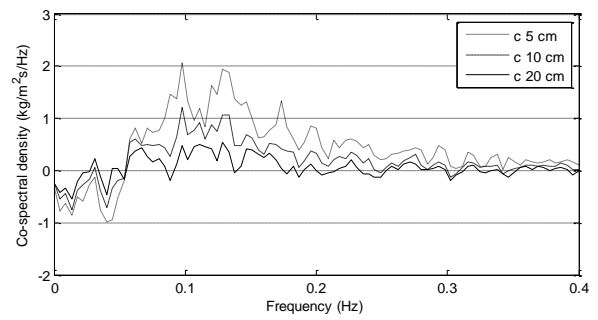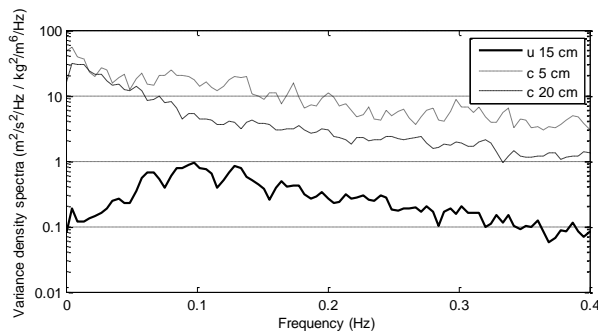
C.2.3   27 Sept 00:00 – 01:00
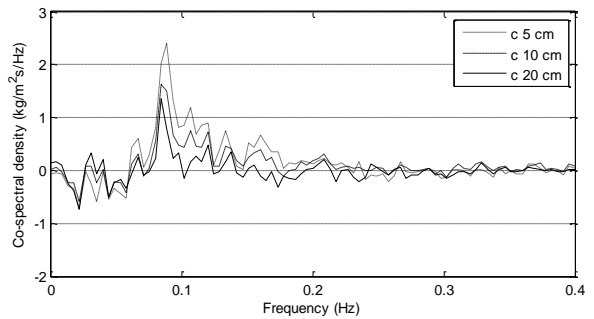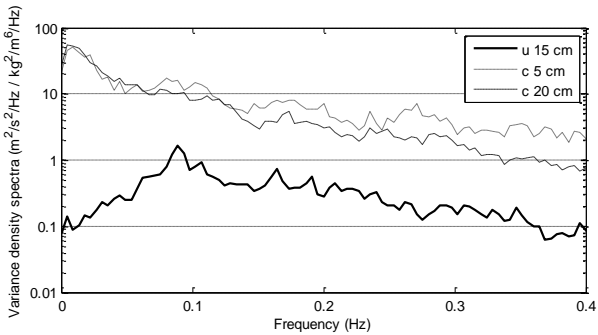
C.2.4   27 Sept 01:00 – 02:00
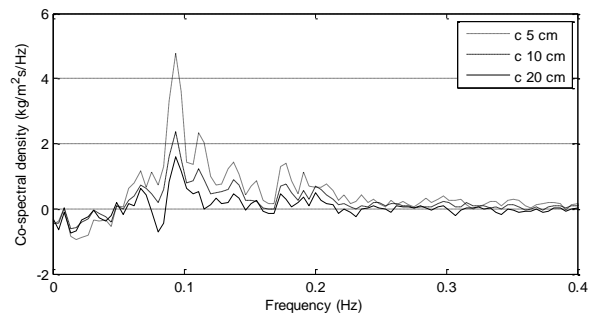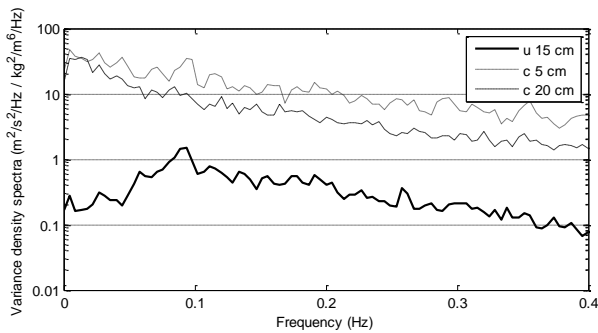
C.2.5 **27 Sept 02:00 – 03:00**
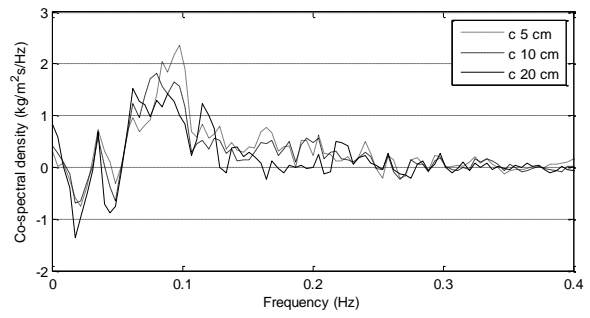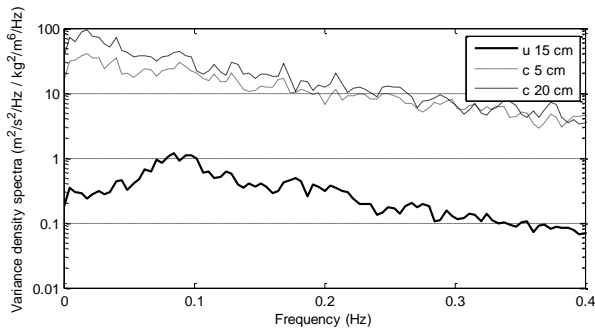
C.3 **Hourly Variance Density Spectrum and Co-spectral density during LWC1 at P3**

Note: Different timeframe compared to P1 and P2 during LWC1, due to the fact that there was not enough data recorded on the 26/27th day half-cylce

C.3.1 **25 Sept 23:00 – 24:00**
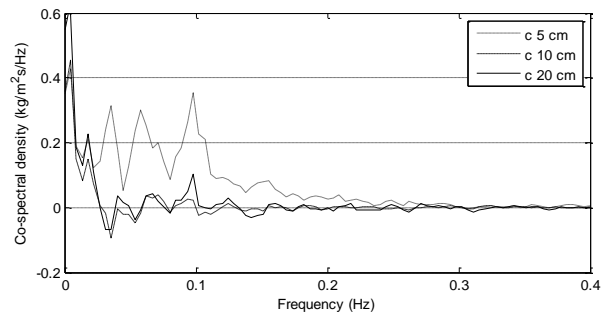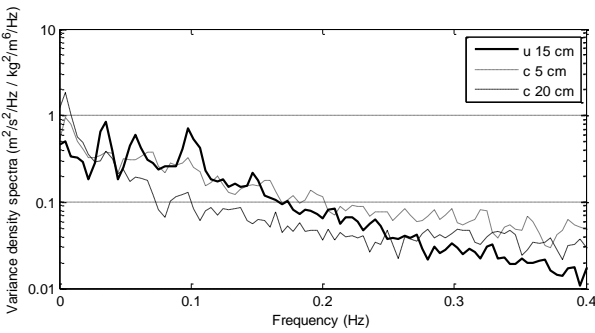
**C.3.2** **26 Sept 00:00 – 01:00**
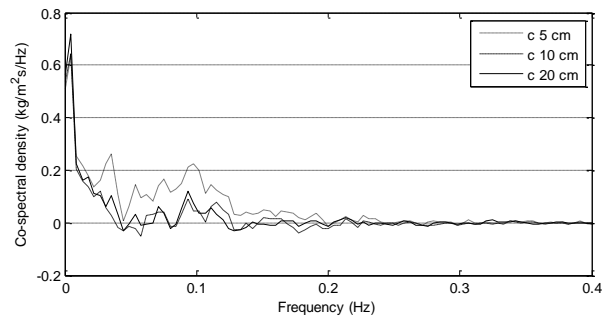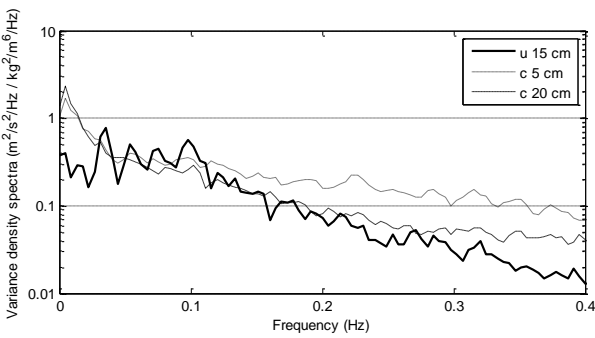
C.4. Hourly Variance Density Spectrum and Co-spectral density during HWC1 at P2

C.4.1   4 Oct 04:00 – 05:00
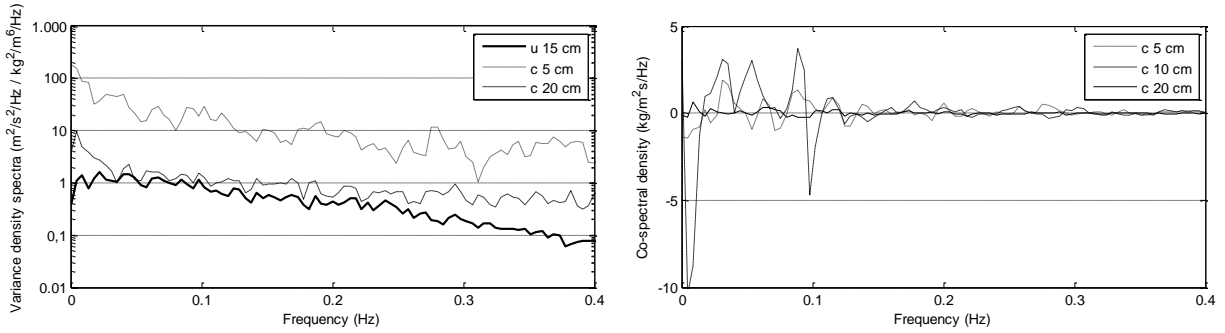
C.4.2   4 Oct 05:00 – 06:00
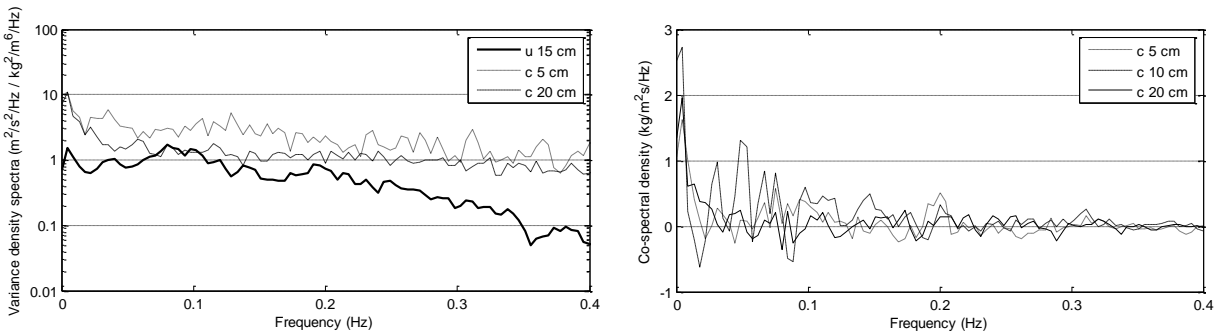
C.4.3   4 Oct 06:00 – 07:00
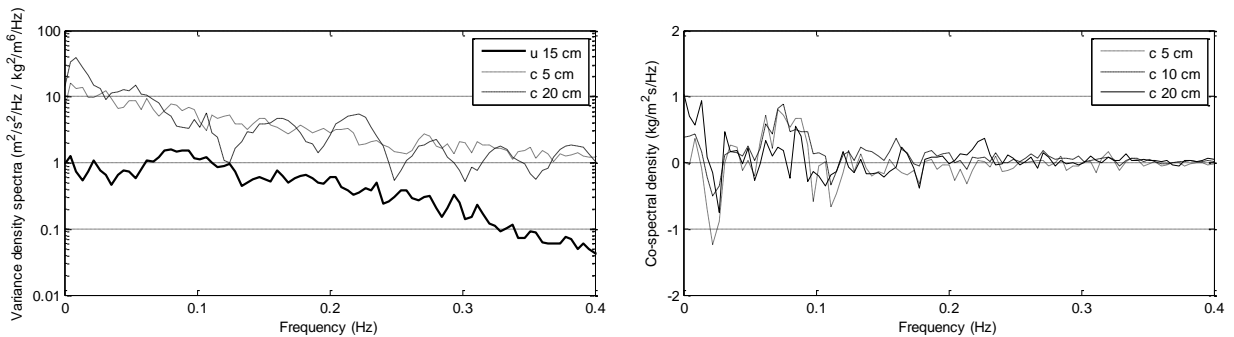
C.4.4   4 Oct 07:00 – 08:00
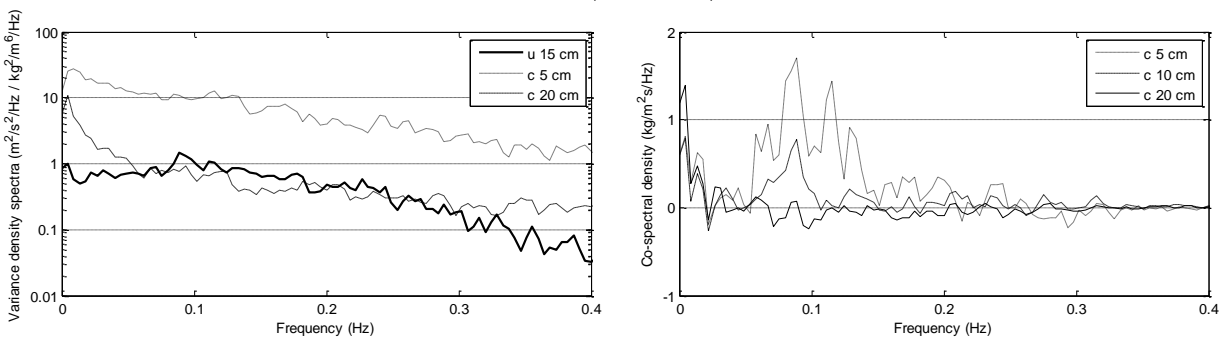
C.4.5   **4 Oct 08:00 – 09:00**
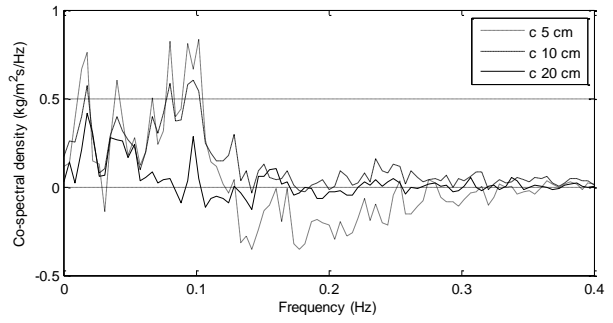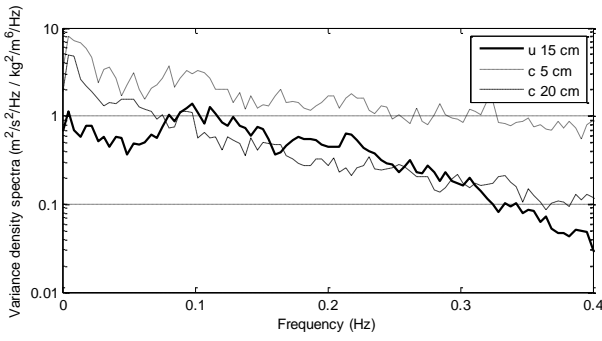
C.4.6   **4 Oct 09:00 – 10:00**
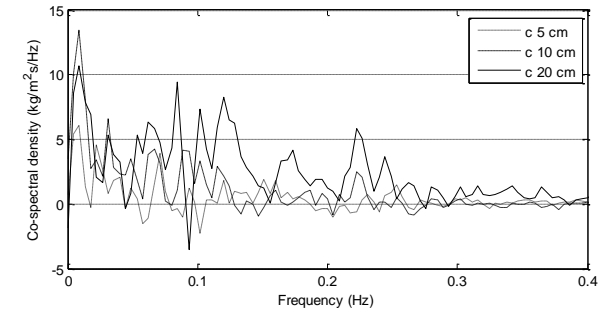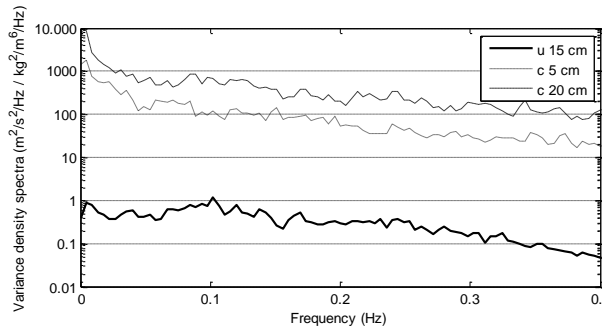
C.4.7   **4 Oct 10:00 – 11:00**
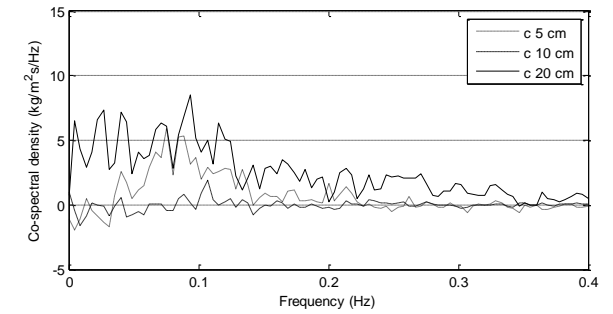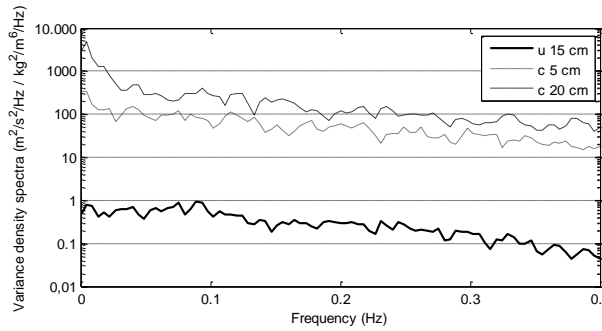
C.4.8   **4 Oct 11:00 – 12:00**
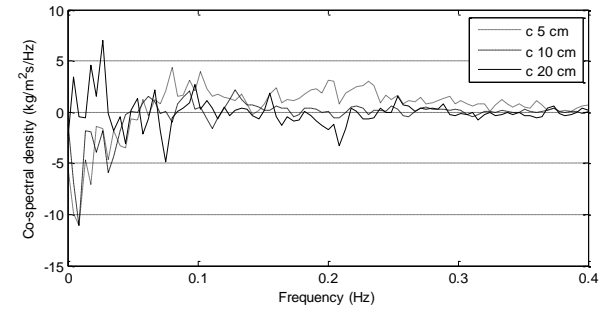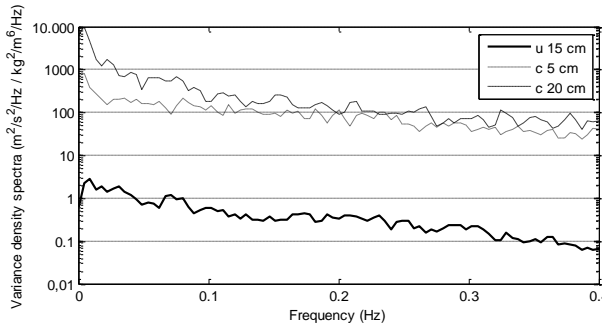
C.4.9   **4 Oct 12:00 – 13:00**
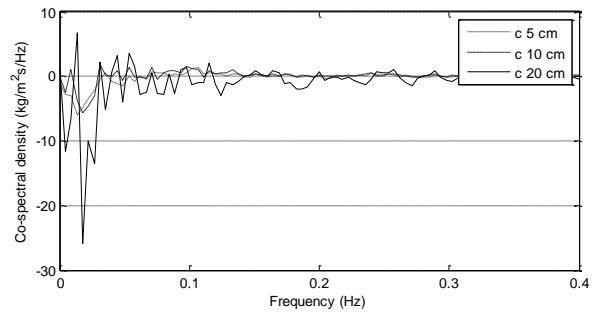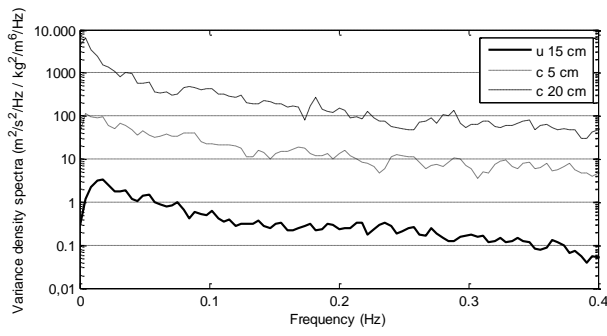
C.4.10   **4 Oct 17:00 – 18:00**
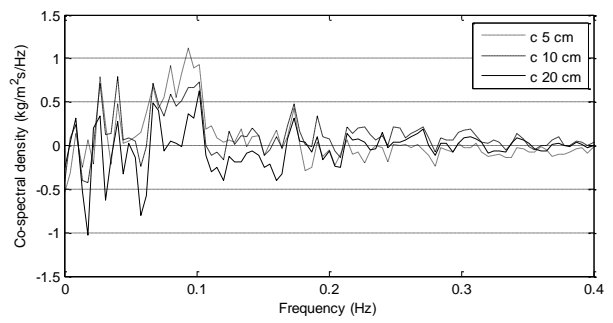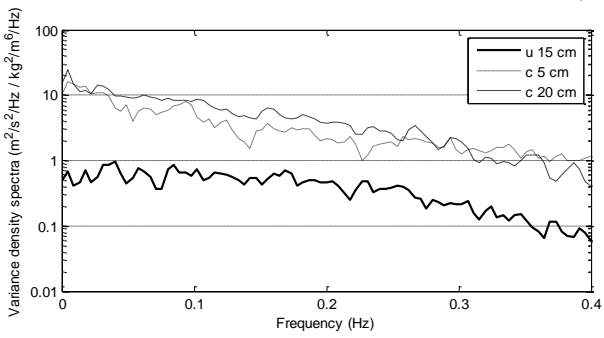
C.4.11   **4 Oct 18:00 – 19:00**
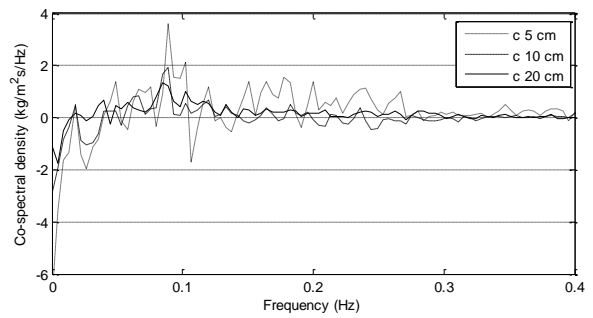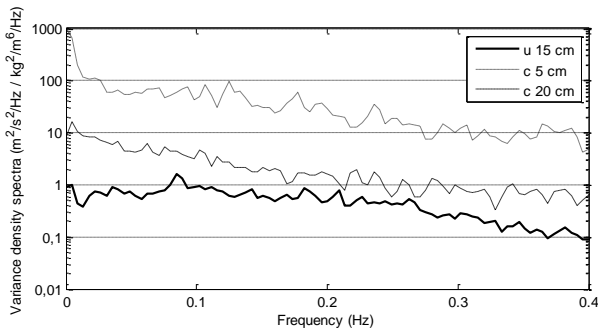
C.4.12   **4 Oct 19:00 – 20:00**
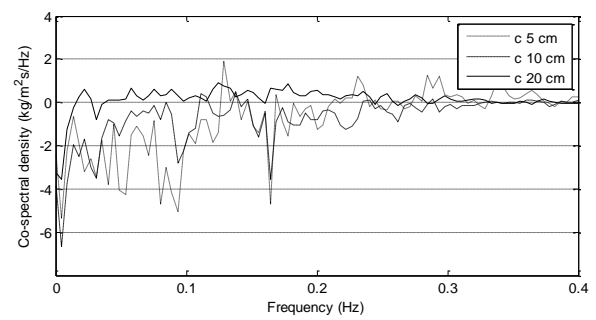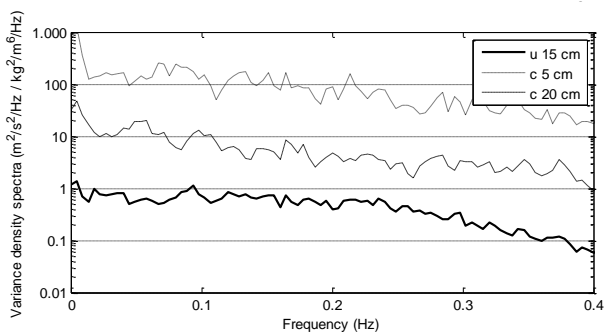
C.4.13   **4 Oct 20:00 – 21:00**
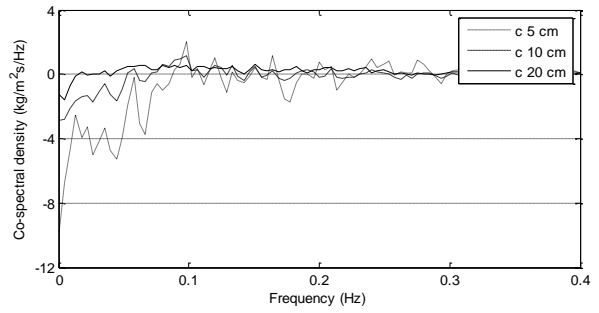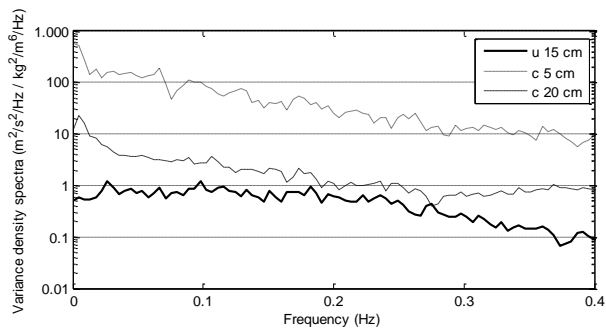
C.4.14   **4 Oct 21:00 – 22:00**
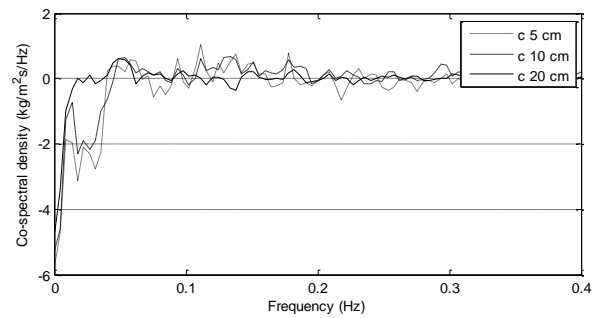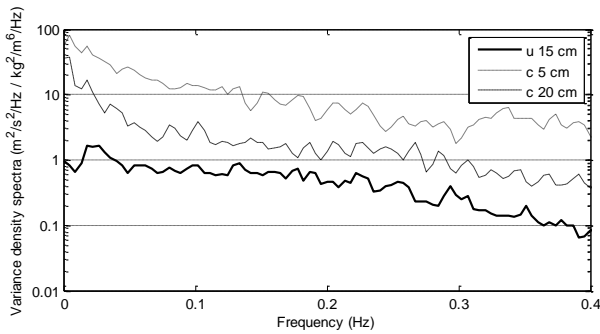
C.4.15   **4 Oct 22:00 – 23:00**
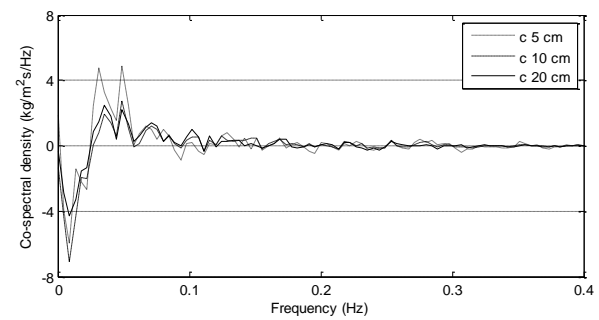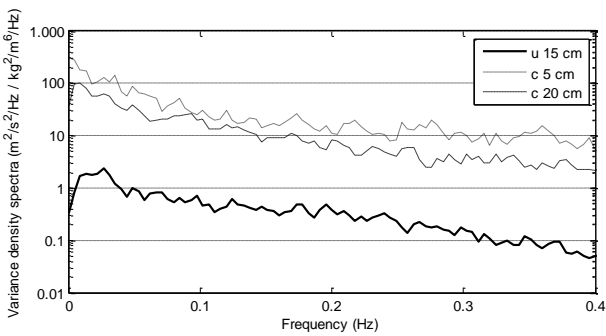
C.5.   Hourly Variance Density Spectrum and Co-spectral density during HWC1 at P3

C.5.1   **4 Oct 04:00 – 05:00**
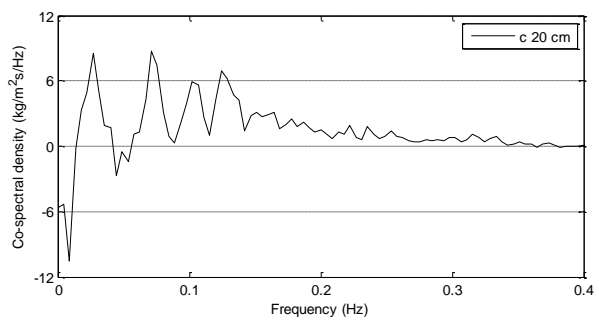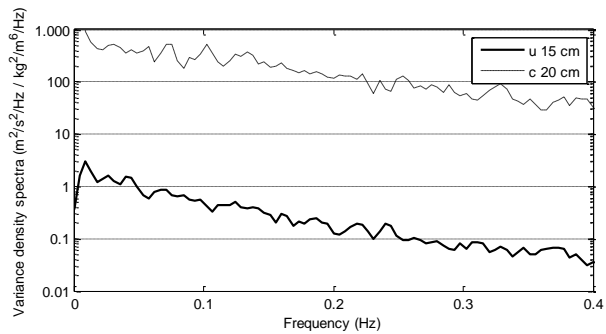
Note: that often at tripod position P3 the bottom two OBS-sensors were intermittently buried in the sand, therefore it is chosen to only plot the spectral results of the upper sensor C3.

C.5.2   **4 Oct 05:00 – 06:00**
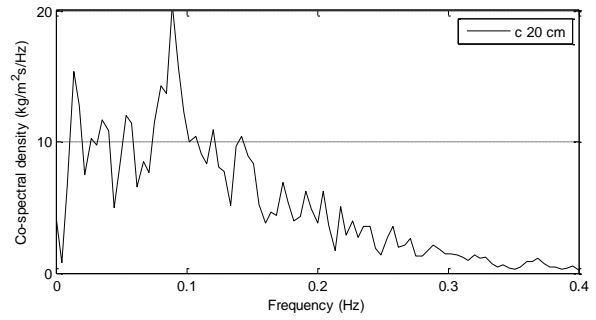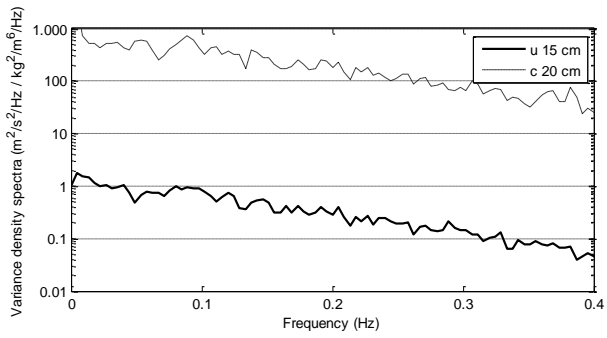
C.5.3   **4 Oct 06:00 – 07:00**
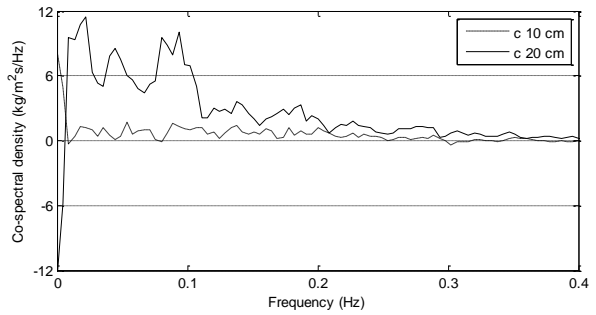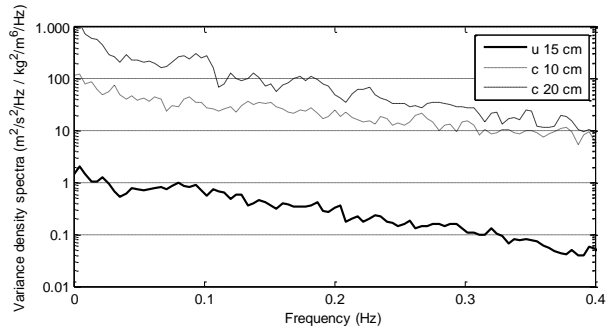
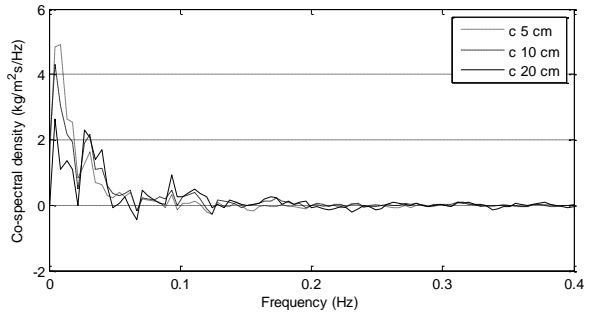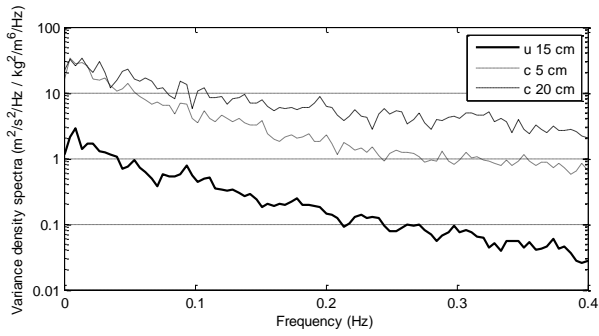**C.5.4**   **4 Oct 07:00 – 08:00**
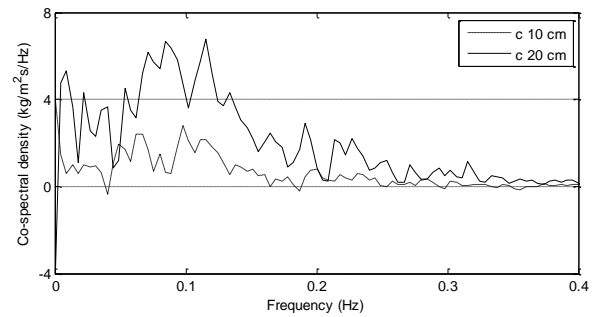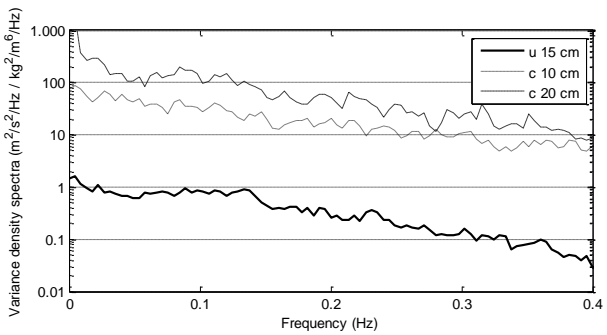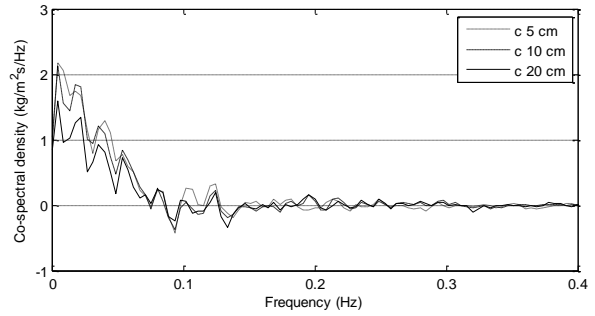

C.5.5   **4 Oct 08:00 – 09:00**
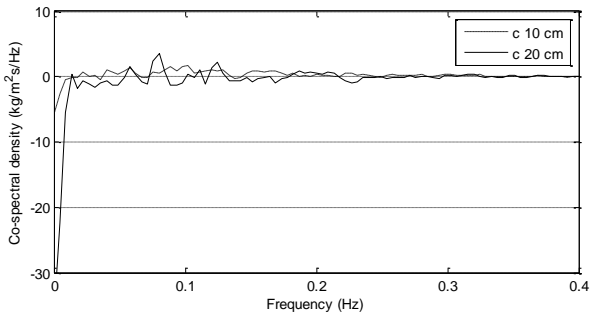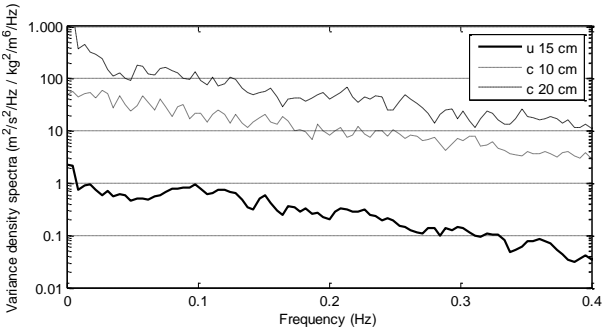
C.5.6   **4 Oct 18:00 – 19:00**
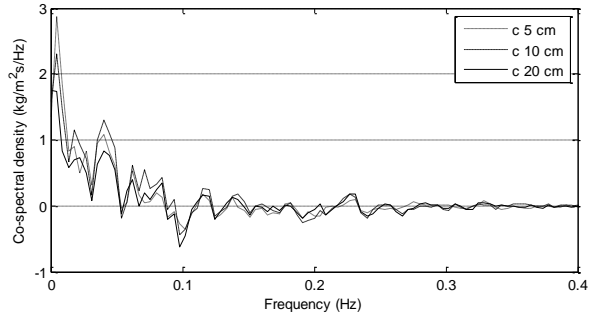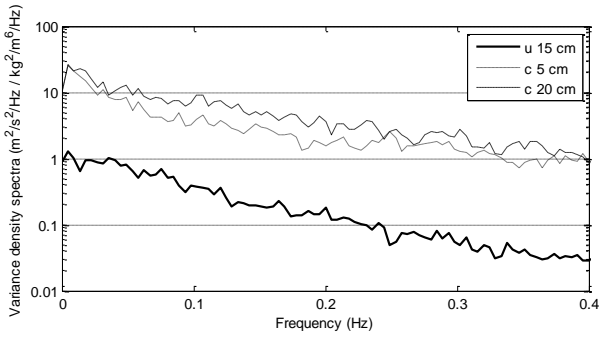
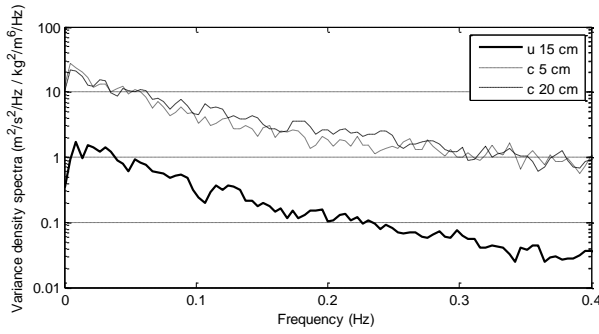**C.5.7**   **4 Oct 19:00 – 20:00**

C.5.8   **4 Oct 20:00 – 21:00**

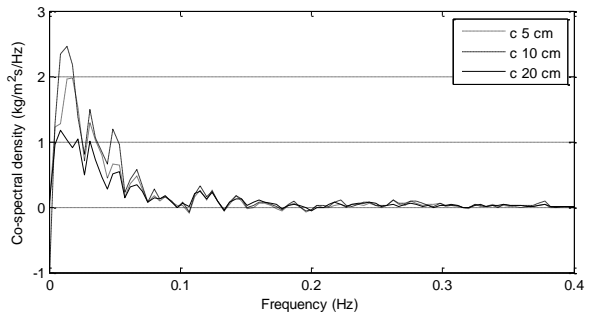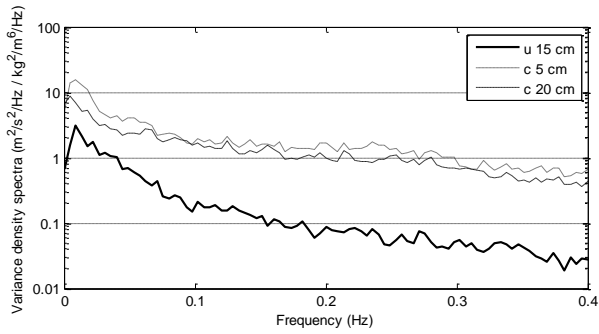**C.6.**   **Hourly Variance Density Spectrum and Co-spectral density during HWC1 at P4**

C.6.1   **4 Oct 07:00 – 08:00**

C.6.2   **4 Oct 08:00 – 09:00**